BIMETALLIC EFFECT OF SINGLE NANOCATALYSTS VISUALIZED BY SUPER-RESOLUTION CATALYSIS IMAGING

A Dissertation
Presented to the Faculty of the Graduate School
of Cornell University
In Partial Fulfillment of the Requirements for the Degree of
Doctor of Philosophy

by
Guanqun Chen
December 2017

BIMETALLIC EFFECT OF SINGLE NANOCATALYSTS VISUALIZED BY SUPER-RESOLUTION CATALYSIS IMAGING

Guanqun Chen

Cornell University 2017

Compared with their monometallic counterparts, bimetallic nanoparticles often show enhanced catalytic activity associated with the bimetallic interface. Direct quantitation of catalytic activity at the bimetallic interface is important for understanding the enhancement mechanism, but challenging experimentally. Using single-molecule super-resolution catalysis imaging in correlation with electron microscopy, we report the first quantitative visualization of enhanced bimetallic activity within single bimetallic nanoparticles. We focus on heteronuclear bimetallic PdAu nanoparticles that present a well-defined Pd-Au bimetallic interface in catalyzing a photo-driven fluorogenic disproportionation reaction. Our approach also enables a direct comparison between the bimetallic and monometallic regions within the same nanoparticle. Theoretical calculations further provide insights into the electronic nature of N–O bond activation of the reactant (resazurin) adsorbed on bimetallic sites. Sub-particle activity correlation between bimetallic enhancement and monometallic activity suggests that the favorable locations to construct bimetallic sites are those monometallic sites with higher activity, leading to a strategy for making effective bimetallic nanocatalysts. The results highlight the power of super-resolution catalysis imaging in gaining insights that could help improve nanocatalysts.

BIOGRAPHICAL SKETCH

Guanqun Chen obtained his B.S. in Polymer Materials and Engineering from Zhejiang University, China, in 2011. During his undergraduate studies, he did training research of using metal nanoparticles in ordered mesoporous silica as a substrate for surface-enhanced Raman spectroscopy (SERS). After undergraduate studies, Guanqun attended graduate school for the PhD program in the Department of Chemistry and Chemical Biology at Cornell University, and was supervised by Prof. Peng Chen. His PhD research was about using single-molecule super-resolution fluorescence microscopy to study metal nanoparticle catalysis.

Dedicated to Lansheng Wang, Hongye Zhang and Zhongtian Chen

ACKNOWLEDGMENTS

I would first express my deepest gratitude to my advisor, Prof. Peng Chen, for his inspiring guidance, as nothing of my research is possible without his instruction and help. His passion, rigorousness, and perfectionism for research would always stimulate me to achieve high-quality work in future career. I also thank my committee member Prof. David A. Muller for his valuable insights as well as the helpful classes; Prof. Poul B. Petersen for his scientific feedback. I also want to thank Prof. Roald Hoffmann for his help and feedback in theoretical calculations.

I am grateful to the former and present Chen group members because of their help, contributions and discussions: Xiaochun Zhou, for training me and sharing his valuable experiences in single-particle catalysis; Tai-yen Chen, for his help in optics and Matlab codes; Justin Sambur, for his instructions in electrochemistry and discussions; Eric Choudhary for TEM characterizations; Hao Shen, Chunming Liu, Feng Yang, Won Jung, Xiangcheng Sun, Xianwen Mao, Mahdi Hesari for their valuable discussions; and Ningmu Zou, for his contributions in my research as well as the friendship.

Many thanks to Dr. Bo Chen in Prof. Roald Hoffmann's group for teaching me the fundamentals and programming of theoretical calculations as well as his contributions in my research. I also want to thank Prof. Nanfeng Zheng for his development and help of the nanoparticle synthesis.

Finally, I would like to thank my family members: my 91-year-old grandmother, Lansheng Wang, my mother, Hongye Zhang, and my father, Zhongtian Chen for their supports and encouragements in my life. The special thanks go to my beloved wife, Yimu Zhao, for her appearances in both my bachelor's thesis and doctoral dissertation.

TABLE OF CONTENTS

LIST OF FIGURES

LIST OF TABLES

CHAPTER ONE

PAST STUDIES OF SINGLE-MOLECULE SUPER-RESOLUTION FLUORESCENCE MICROSCOPY OF HETEROGENOUS CATALYSIS

1.1 Introduction

Catalysis is very important in modern societies, as it enables many crucial processes such as petroleum refinery, clean energy generation, chemical production, pharmaceutical development and pollutant removal[1,2]. Catalysis are generally divided into two categories: homogeneous catalysis, in which the reactant and catalysts are in one phase (solution), and heterogeneous catalysis, in which the catalytic reaction occurs at or near the interface between two phases, typically gas-solid or liquid-solid[3]. One advantage of heterogeneous catalysis (over homogenous catalysis) is the facile separation between the product mixture and catalysts after reaction and therefore it is generally more favorable in chemical industry[2]. Nanoparticles have become an important class of heterogeneous catalysts because they offer 1) large surface-to-volume ratio, desirable for surface reaction (catalysis) and 2) distinct properties (i.e. high activity, high selectivity) due to the nanoscale structures[1,2,4-7]. The very central question for nanoparticle catalysis research is to understand is the fundamental structure-function correlation, which essentially connects the structural and electronic properties of nanoscale materials to the mechanism of catalytic reaction.

The enormous efforts in studying nanoparticle catalysis have made significant achievements[1,2,4-10]. However, the nanoparticle heterogeneity seems to be a challenge to the traditional catalytic characterizations, in which the ensemble-averaged results are from many nanoparticles and thus the individualities of single particles are masked[11]. Nanoparticle heterogeneity is a general term, which means particle-to-particle differences in size, geometry, composition, crystal facets, defect densities, etc. Recently, the development of advanced characterization methods enables single-particle studies, in which people could interrogate the properties of a single nanoparticle without interference from others. Such techniques include electrochemical scanning probe microscopy (SECM)[12,13], single-molecule fluorescence microscopy[14-16], surface plasmon resonance spectroscopy[17,18] and many others[19-22].

This chapter gives a brief review of single-molecule super-resolution (SMSR) fluorescence microscopy in studying heterogeneous catalysis. The following sections cover the fundamentals and selected examples of SMSR fluorescence microscopy studies of nanoparticle catalysis.

1.2 Fundamentals of single-molecule super-resolution fluorescence microscopy

The resolution limit of a conventional optical microscope is called Abbe's diffraction limit (formulated by Ernst Abbe in 1873 and Lord Rayleigh in 1896), which is about half of the wavelength of the light used in the microscope (typically ~200-300 nm for visible light). The Nobel Prize in Chemistry 2014 was awarded to Eric Betzig, Stefan W. Hell and William E. Moerner for their contributions to the development of "super-resolved fluorescence microcopy", in which the spatial resolution could reach far beyond Abbe's diffraction limit. There are mainly two approaches of super-resolved fluorescence microscopy: 1) stimulated emission depletion (STED) microscopy[23], in which, at one time, only the fluorophores in a very small region, less than the diffraction-limited size, can be excited to achieve super-resolution imaging, and 2) single-molecule super-resolution (SMSR) fluorescence microscopy[24], in which, at one time, only a single fluorophore within a diffraction-limited area is excited and its position can be localized with a precision of several to tens of nm.

The single-molecule super-resolution (SMSR) fluorescence microscopy is widely applied to biologic sciences due to multiple desirable features. First, it enables both in vitro and in vivo studies because the imaging condition (ambient environment) is very friendly to biological systems. Second, the high spatial resolution (~tens of nm) matches the dimension of the objects in cells[25]. Third, the high temporal resolution (down to several ms) offers capability of tracking the biochemical reactions at single-turnover level as well as the motions of proteins or DNA in cells[26,27]. Fourth, the implementation of SMSR fluorescence microscope is relatively easy compared to the sophisticated imaging techniques (i.e., electron microscopes).

Derived from single-molecule enzymology studies in which the single-enzyme activity was measured[26,28], the single-nanoparticle catalysis studies, using similar approach and analysis, emerged rapidly[14-16]. The shared facts between enzymes (biological homogenous catalysts) and nanoparticles (non-biological heterogeneous catalysts) inspired people to use SMSR fluorescence microscopy to study nanoparticle catalysis. Similarly as discussed above, there are several advantages of SMSR fluorescence microscopy in single-particle catalysis study: 1) The ambient experiment condition enables in-situ catalysis measurement in aqueous solution at room temperature. 2) The high spatial resolution (~tens of nm) allows for the catalytic characterization at single-particle or even sub-particle level[29]. 3) The high temporal resolution, at single-turnover level (~tens of ms), is powerful in studying the kinetics of catalysis on single nanoparticles[30].

The typical experimental setups of wide-field SMSR fluorescence microscope are shown in Figure 1.1. Depending on the way of laser excitation, there are mainly two types: total-internal-reflection fluorescence (TIRF) microscope (Figure 1.1A) and epifluorescence microscope (Figure 1.1B)[31]. In both setups, the catalysts are in a fluidic cell containing reactant solution. The fluorescence signals of catalytic products formed on the nanocatalysts are collected by an electron-multiplying CCD (EMCCD) camera, which is very sensitive in photon detection. The TIRF microscope has better signal-to-noise ratio because it only excites (by the evanescent field) a small volume (~200-300 nm in depth) of solution close to the quartz slide surface (where the particles are deposited on). Therefore this method works for small nanoparticles (less than 200 nm in size). The epifluorescence microscope is suitable for thicker particles (hundreds of nm to microns in thickness) because the excitation laser directly goes through the entire flow cell and thus could excite the whole catalyst particle.

The temporal information of fluorescence image is straightforward; each image is time-coded and the temporal resolution is determined by the operating frame rate of the camera. The spatial information is generated by the following data analysis. Each fluorescent spot in the image is a point spread function (PSF) and its position can be determined by fitting its intensity profile with a 2-D Gaussian equation[32]. Generally the localization precision is about tens of nm, depending mainly on the number of photons collected from its emission[32].

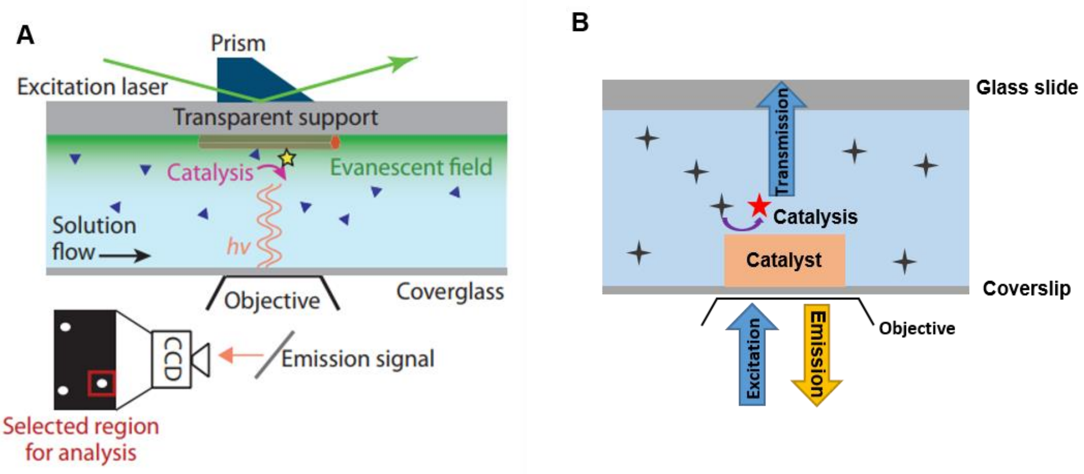

Figure 1.1 Experimental setups of single-molecule super-resolution fluorescence microscopy. (A) Prism-type total-internal-reflection fluorescence (TIRF) microscope and (B) Epifluorescence microscope. Figure A adapted from Sambur et al.[11] Copyright 2014 Annual Reviews.

There are tremendous efforts in developing the SMSR approach for nanoparticle catalysis, which include applications in thermal catalysis[29,30,33-36], photocatalysis[37,38], electrocatalysis[39] and photoelectrocatalysis[40]. The selected examples are reviewed in the next subsection.

1.3 Single-molecule super-resolution fluorescence microscopy in studying catalysis

1.3.1 Thermal catalysis

SMSR fluorescence microscopy was first applied to the thermal catalysis separately by Hofkens[33] and Chen[30] with their coworkers, which established the foundation of single-particle catalysis study by single-molecule fluorescence microscopy.

Roeffaers et al.[33] mapped a catalytic fluorogenic reaction on layered double hydroxide (LDH) catalysts with single-turnover temporal resolution. The LDH catalyzes a transesterification or hydrolysis reaction of non-fluorescent fluorescein ester to fluorescent fluorescein in alcohol solvent or aqueous solution. It is found that the transesterification and hydrolysis reactions of 5-carboxyfluorescein diacetate (C-FDA) have different spatial activity patterns (Figure 1.2, A, B for transesterification, E, F for hydrolysis): the transesterification occurs across the entire basal {0001} plane (Figure 1.2C) while the hydrolysis preferentially proceeds on the lateral $\{10\bar{1}0\}$ facets (Figure 1.2G). This spatially resolved activity measurement shows that the single-molecule fluorescence microscopy could provide insights into heterogeneous catalysis and could generate useful information toward rational design of effective industrial catalysts.

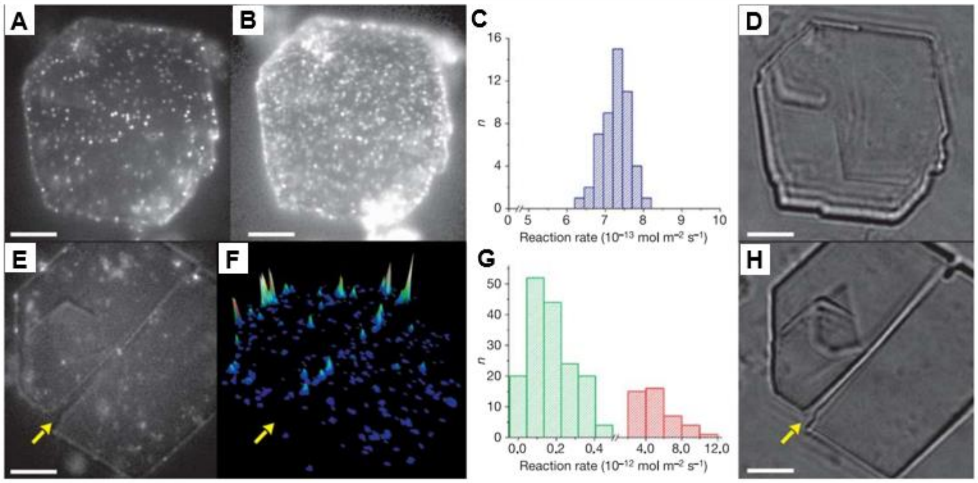

Figure 1.2 Spatially-resolved catalysis on single crystals. (A) Fluorescence wide-field image of a transesterification reaction in 1-butanol on a layered double hydroxide (LDH) crystal at 40 nM ester concentration. (B) Same as A but at 700 nM ester concentration on the same LDH crystal. (C) Distribution of the reaction rate of 1 μm^2 area on the crystal surface. (D) Optical transmission image of the crystal in A. (E) Same as A but for a hydrolysis reaction on a different crystal in aqueous solution at 600 nM ester concentration. (F) Accumulated fluorescence image (over 256 images) of the crystal in E. (G) same as C, but for the crystal in E. There are two distinct populations: the fast population is on $\{10\bar{1}0\}$ facets (red) and the slow one is on $\{0001\}$ facets. (green). (H) Optical transmission image of the crystal in E. Scale bars, 5 μm. Figures adapted from Roeffaers et al.[33] Copyright 2006 Nature Publishing Group.

Xu et al.[30] first applied the single-molecule fluorescence microscopy to study single-nanoparticle catalysis kinetics. Au nanoparticles can catalyze a fluorogenic deoxygenation (reduction) reaction of non-fluorescent resazurin to highly fluorescent resorufin with reductant hydroxylamine. The fluorescence intensity trajectory from a Au nanoparticle was shown in Figure 1.3A, in which each fluorescence burst is a single turnover of resazurin to resorufin. The single off- and on- times, τ_{off} and τ_{on}, are stochastic but their inverse average values, $\langle\tau_{\mathrm{off}}\rangle^{-1}$ and $\langle\tau_{\mathrm{on}}\rangle^{-1}$ are resazurin concentration dependent (Figure 1.3B, C), indicating the formation of resorufin on Au nanoparticles follows a Langmuir–Hinshelwood mechanism[41] and the product dissociation could have two pathways, direct dissociation and substrate-assisted dissociation. By quantitative analysis of $\langle\tau_{\mathrm{off}}\rangle^{-1}$ and $\langle\tau_{\mathrm{on}}\rangle^{-1}$, three types of $\langle\tau_{\mathrm{on}}\rangle^{-1}$ behaviors were identified: depending on the relative rate of direct dissociation and substrate-assisted dissociation, $\langle\tau_{\mathrm{on}}\rangle^{-1}$ of individual Au particle could increase, decrease or stay unchanged with the increase of resazurin concentration. Also, the catalytic activity dynamics, reflected by the activity fluctuation of single Au nanoparticles, was examined and attributed to the dynamic surface reconstruction. All of the information generated in this study shows the power of single-molecule fluorescence microscopy in studying the reaction kinetics of single-particle catalysis, which is a remarkable advantage of this approach compared with ensemble-averaged catalytic measurements.

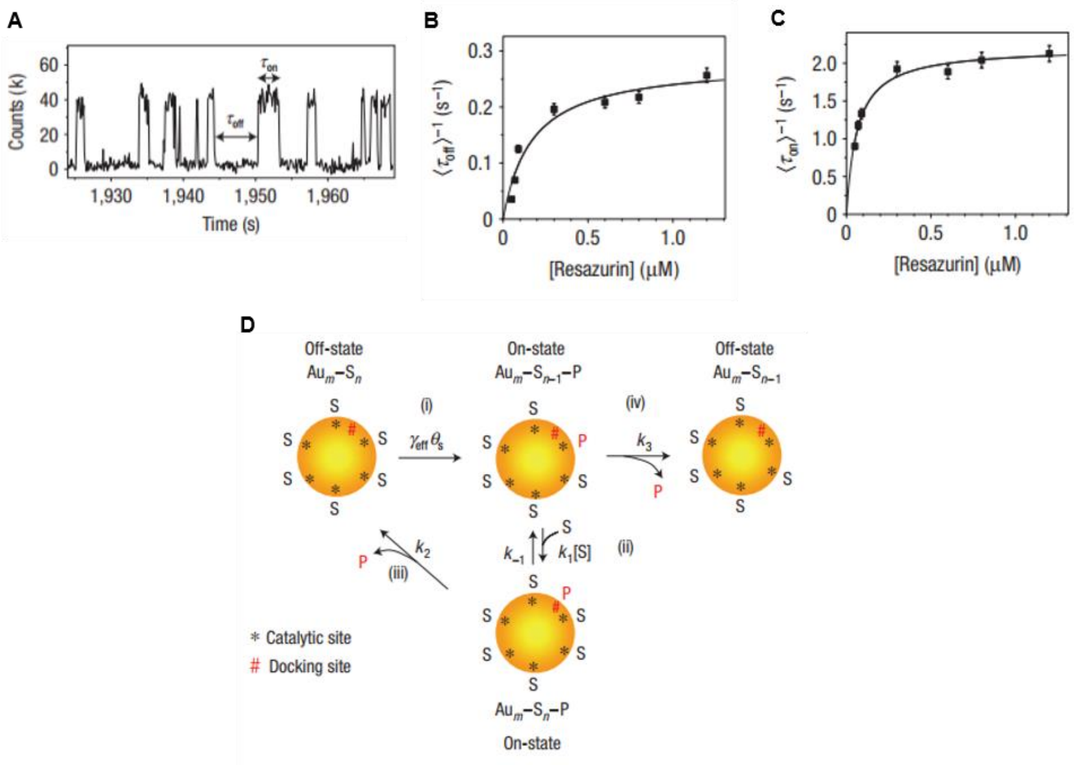

Figure 1.3 Single Au nanoparticle catalysis kinetics. (A) A segment of the fluorescence intensity trajectory from a Au nanoparticle catalyzing a deoxygenation reaction of non-fluorescent resazurin to form fluorescent resorufin. (B) Resazurin concentration dependence of $\langle\tau_{off}\rangle^{-1}$. τ_{off} is the waiting time before resorufin formation. (C) Same as B, but for $\langle\tau_{on}\rangle^{-1}$. τ_{on} is the waiting time before resorufin dissociation after its formation on the particle. (D) Kinetic mechanism of single Au nanoparticle catalysis. S: resazurin; P: resorufin. Au_m–S_n represents a Au nanoparticle having *n* adsorbed resazurin molecules. Figures adapted from Xu et al.[30] Copyright 2008 Nature Publishing Group.

Using SMSR fluorescent microscopy, Zhou et al.[29] mapped the activity of single mesoporous silica coated Au (Au@mSiO_2) nanorods in catalyzing an oxidative deacetylation reaction of non-fluorescent Amplex Red to fluorescent resorufin (Figure

1.4A). Interestingly, the catalytic activity along the side of Au nanorod, which should be of the same crystal facet, is not homogenous. An activity gradient from the center (highest) toward both ends is discovered (Figure 1.4B). It is also found that this gradient is negatively related to the nanorod length (Figure 1.4C), supporting that the observed activity gradient might be related to the defect density gradient which was introduced during the seeded growth of these nanorods. Also using SMSR fluorescent microscopy, Andoy et al.[34] observed a similar phenomenon on two-dimensional mesoporous silica coated Au nanoplates in catalyzing a reduction reaction of resazurin to resorufin: there is an activity gradient from the center toward the periphery of the Au nanoplate (Figure 1.4D, E) and the activity gradient is also negatively related to the size of the nanoplate (Figure 1.4F). These two studies are solid evidences that the SMSR fluorescence microscopy could help unveil the catalytic properties at sub-particle level thus render new knowledge of nanoparticle catalysis.

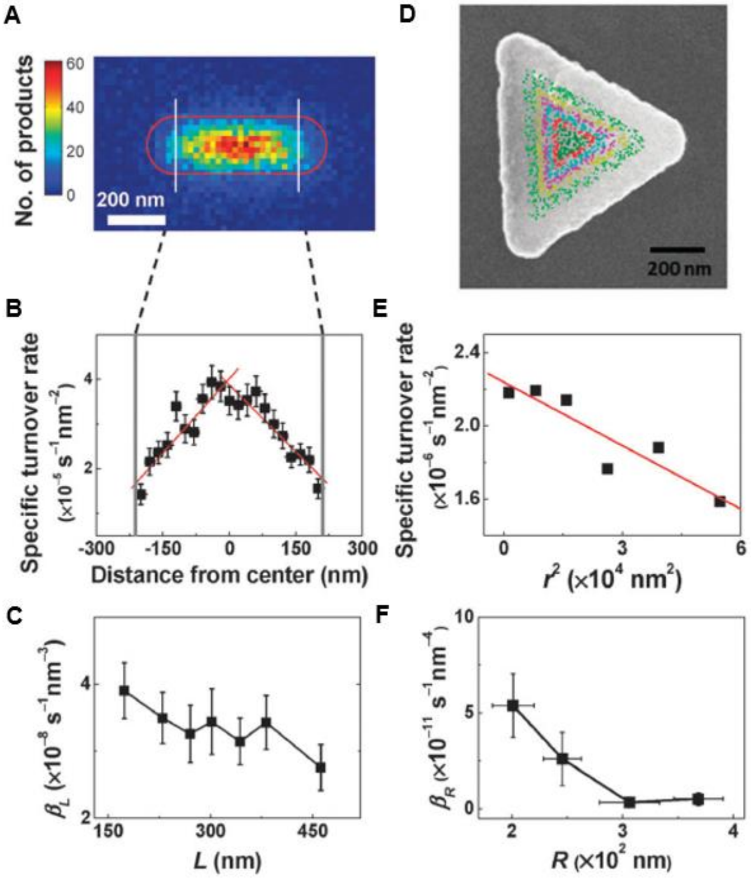

Figure 1.4 Catalytic activity gradient within single nanocatalysts. (A) 2-D histogram of catalytic product (resorufin) positions on a single Au@mSiO_2 nanorod, in which a bi-directional catalytic activity decay from the center toward both ends was observed. The red line is the structural contour of this particle determined by SEM. The catalytic events on the particle between two white lines were analyzed to show the gradient. (B) Line-profile of the specific turnover rate along the side of the particle in A. (C) The linear activity gradient β_L vs. nanorod length L. (D) Catalytic product (resorufin) positions on a single Au@mSiO_2 nanoplate. Their positions are color-coded based on the distance from the center of nanoplate. (E) The specific turnover rate vs. r^2, r is the distance from the center of nanoplate. (F) The radial activity gradient β_R vs. nanoplate radius R. Figure

adapted from Chen et al.[15] Copyright 2013 Royal Society of Chemistry. Original data of A, B, C are adapted from Zhou et al.[29] Copyright 2012 Nature Publishing Group. Original data of D, E, F are adapted from Andoy et al.[34] Copyright 2013 American Chemical Society.

1.3.2 Photocatalysis

Majima and coworkers developed a fluorescent boron-dipyrromethene (BODIPY)-based dye (3,4-dinitrophenyl-BODIPY, DN-BODIPY) as the probe of photocatalysis [42]. Upon 365 nm UV-excitation of TiO_2 nanoparticles, non-fluorescent DN-BODIPY can undergo a photocatalytic reduction to form fluorescent 4-hydroxyamino-3-nitrophenyl-BODIPY (HN-BODIPY) by accepting the photo-generated electrons from TiO_2. Using this dye, Tachikawa et al. applied SMSR fluorescence microscopy to study photocatalysis of anatase TiO_2 single crystals (Figure 1.5A)[37]. There is a strong facet-dependence of the photocatalytic reduction activity: the reaction preferentially occurred on the lateral {101} facets (Figure 1.5B, C), indicating the photogenerated electrons tend to be trapped on {101} surfaces rather than basal {001} facets. Interestingly, when {001} surface was illuminated by UV light, the reaction still occurred on the {101} facets with a considerable activity (Figure 1.5D). On the contrary, when {101} surface was illuminated, the activity was much lower on {001} compared to that on {101} (Figure 1.5E). These observations indicate an anisotropic electron flow within the single TiO_2 crystals, which might be informative for people to understand the photocatalysis on anisotropic nanocrystals.

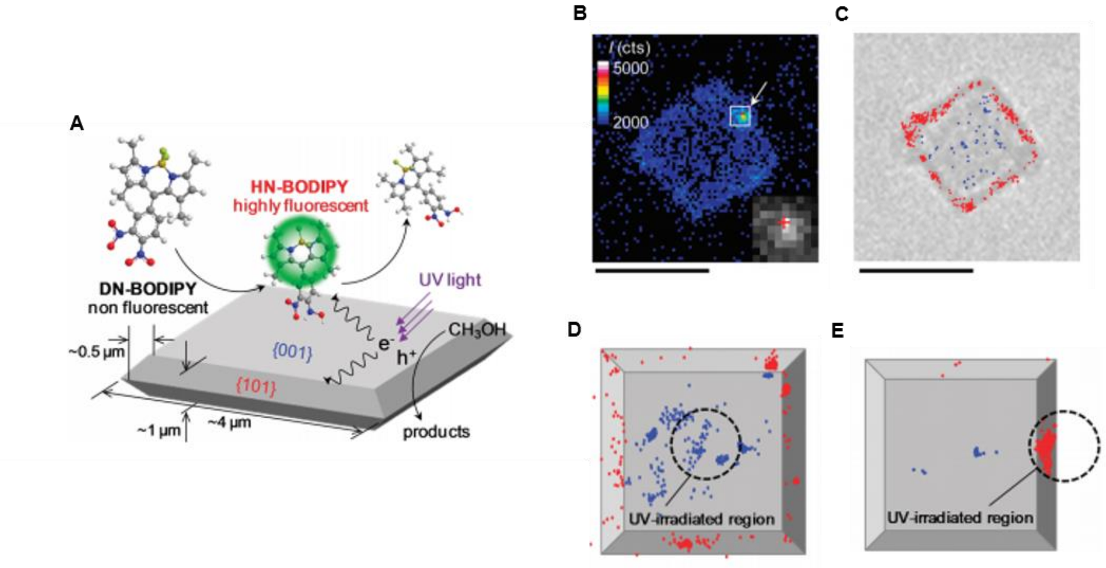

Figure 1.5 Photocatalysis of single TiO_2 crystals. (A) Photocatalysis on a single TiO_2 crystal. (B) Fluorescence image of a single TiO_2 crystal in catalyzing a fluorogenic photoreaction. The inset is the raw image in the square box indicated by the white arrow. (C) Transmission image of the single TiO_2 crystal in B. The blue and red dots are products on {001} and {101} crystal facets, respectively. (D) The product locations on {001} (blue) and {101} (red) facets upon UV irradiation of the center region ({001} surface). The beam size was 2 μm in diameter, indicated by the dashed circle. (E) Same as D but the UV irradiation was focused at the lateral {101} facet. Scale bars, 4 μm. Figures adapted from Tachikawa et al[37]. Copyright 2011 American Chemical Society.

1.3.3 Electrocatalysis

Xu et al. first applied SMSR fluorescence microscopy to study the electrocatalysis of single-walled carbon nanotubes (SWNTs)[39]. The redox chemistry of the reactant resazurin is shown in Figure 1.6A. Resazurin (S) can undergo a two-electron reduction to resorufin (P), which is highly fluorescent and can be detected at single-turnover level by SMSR fluoresce microscopy. Resorufin (P) can be further reduced to dihydroresorufin (PH_2) and this conversion is reversible. To apply potentials for electrocatalysis, the SWNTs were deposited on an ITO-coated quartz slide, which served as the working electrode. Upon the negative potentials and constant supply of resazurin aqueous solution, the single-molecule fluorescent signals from the electrocatalysis product resorufin were detected on single catalytic sites of SWNTs. The sudden decrease of fluorescence intensity after product resorufin formed on the nanotube was attributed to the further reduction of resorufin (P) to dihydroresorufin (PH_2). Thus the waiting time before a fluorescent signal occurs, τ_{off}, reflects the electrocatalytic activity of resazurin (S) to resorufin (P), and the waiting time before a fluorescent signal disappears, τ_{on}, reflects the electrocatalytic activity of resorufin (P) to dihydroresorufin (PH_2). And their inverse averages, $\langle\tau_{\text{off}}\rangle^{-1}$ and $\langle\tau_{\text{on}}\rangle^{-1}$, are the reaction rates of S to P and P to PH_2 of a single catalytic site, respectively, which are indeed heterogeneous among reactive sites of SWNTs. The resazurin concentration dependence of ensemble-averaged $\langle\tau_{\text{off}}\rangle^{-1}$ and $\langle\tau_{\text{on}}\rangle^{-1}$ at different potentials are shown in Figure 1.6B, C. By quantitative analysis of the waiting times, the kinetic mechanism of electrocatalysis by SWNTs was proposed (Figure 1.6D). This single-particle electrocatalysis study, reflects the heterogeneity among SWNT reactive sites, which also broadens the applications of SMSR fluorescence microscopy in heterogeneous catalysis.

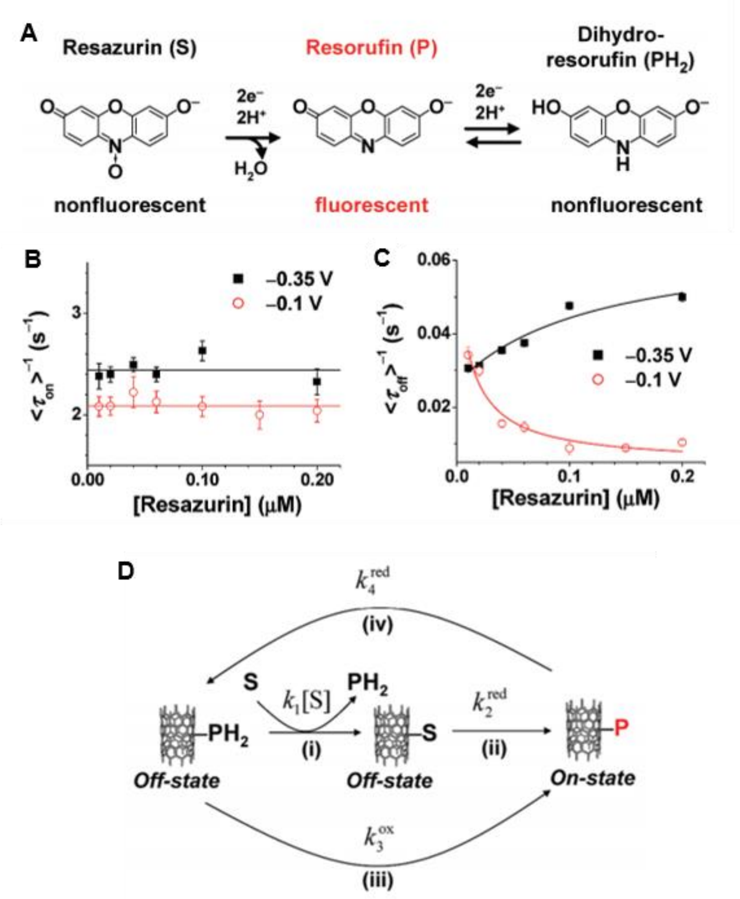

Figure 1.6 Electrocatalysis of single-walled carbon nanotubes (SWNTs). (A) Redox conversions of resazurin in aqueous solution. (B) $\langle\tau_{\text{on}}\rangle^{-1}$ at two different potentials, −0.35 V (black) and −0.1V (red), τ_{on} is the waiting time before the dissociation of resorufin from the particle. (C) Same as B but for $\langle\tau_{\text{off}}\rangle^{-1}$, τ_{off} is the waiting time before the generation of resorufin on the carbon nanotube. (D) Kinetic mechanism of the electrocatalysis on single-walled carbon nanotubes (SWNTs). S: resazurin; P: resorufin; PH_2: dihydroresorufin. Figures adapted from Xu et al.[39] Copyright 2009 American Chemical Society.

1.3.4 Photoelectrocatalysis

Chen and coworkers studied the photoelectrocatalysis of single crystalline TiO_2 nanorods, and the activity mapping was used as the guild for the optimized oxygen-evolution-catalyst (OEC) deposition on TiO_2 nanorods (Figure 1.7A)[40]. Two redox probes, Amplex Red and resazurin, were used to map the photo-generated hole (h^+) and electron (e^-) activities of single TiO_2 nanorods upon UV excitation, respectively (Figure 1.7, B, D, F for hole-induced reaction, C, E, G for electron-induced reaction). At potential $E \geq -0.3$V, Amplex Red can undergo a hole-induced oxidation reaction to form fluorescent product resorufin (Figure 1.7L), and when $E \leq -0.4$V, resazurin can react with the photo-generated electrons to form resorufin (Figure 1.7M). Upon 365 nm laser excitation and at $E \geq -0.3$V, there is an anodic photocurrent from the water oxidation, which is qualitatively similar to the hole-induced reaction activity measured from the catalysis imaging (Figure 1.7N). Interestingly, there are some catalytically hot spots on TiO_2 nanorods and a positive correlation between the hole and electron activities is observed (Figure 1.7K), which means those hot spots are active for both hole and electron reactions, and presumably should be the ideal locations to deposit OEC for water oxidation. After photochemically depositing the cobalt-based OEC on these hot spots (Figure 1.7H, I, J), the enhanced absorbed-photon-to-current efficiency (η) and negatively shifted onset potential ($E_{\mathrm{on,GB}}$) are observed as expected (Figure 1.7O). Strikingly, there is a negative correlation between the relative improvement of η, which is $\Delta\eta/\ \eta$, and the initial η (Figure 1.7P), indicating that upon OEC deposition, the originally more active sites got less relative improvement of the activity. The similar negative correlation is observed between the relative change of onset potential $E_{\text{on,GB}}$, which is $\Delta E_{\text{on,GB}}/ E_{\text{on,GB}}$, and the initial $E_{\text{on,GB}}$ (Figure 1.7Q), indicating the nanorods with originally more negative onset potentials gained less negative shift (of the onset potentials) after OEC deposition. These results are particularly useful for designing effective water-splitting photocatalysts and the authors indeed proposed a block-deposit-remove strategy to make the OEC catalysts optimally deposited on semiconductor materials. The experimental techniques and discoveries in this photoelectrocatalysis study[40] represent the frontier of using SMSR fluorescence microscopy to study heterogeneous catalysis.

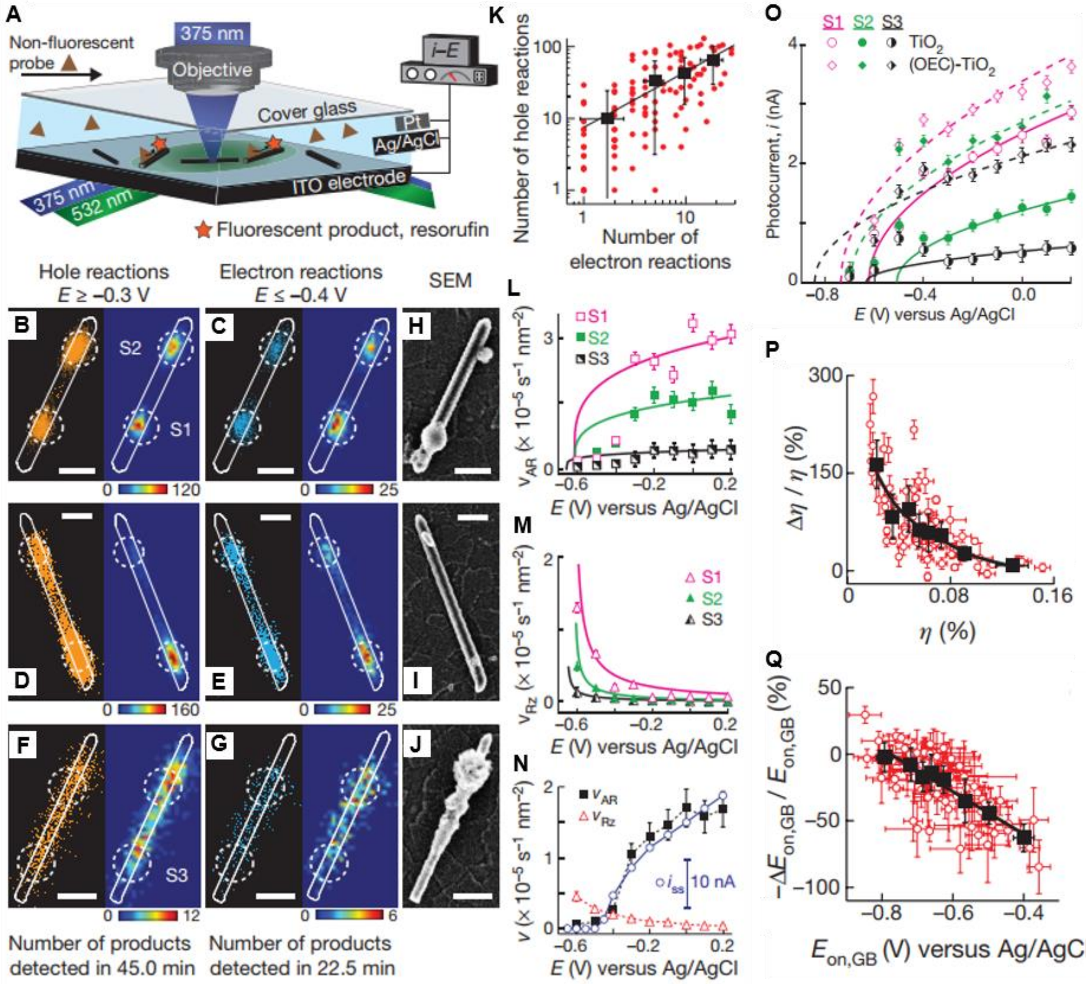

Figure 1.7 Activity mapping of single TiO_2 nanorod photoelectrocatalysis as the guild for optimal oxygen-evolution-catalyst (OEC) deposition. (A) Experimental setup of the SMSR fluorescence imaging of photoelectrocatalysis. (B) Scatter plot (left) and 2-D histogram (right) of the product (resorufin) positions, from a photo-generated hole-induced reaction, on a single TiO_2 nanorod. (C) Same as B but the product molecules (resorufin) are from a photo-generated electron-induced reaction. (D-E) and (F-G) are the same as B and C but for two different nanorods. (H-J) SEM images of the nanorods shown in B-G, after OEC deposition on the activity hot spots. All scale bars, 400 nm. (K) Correlation between the activities of hole reaction and electron reaction for the

pixels on the nanorod in B and C. (L-M) Potential dependences of the turnover rates (v_{AR} for hole reaction, v_{Rz} for electron reaction) of the spots (S1, S2, S3) indicated by dashed circles in B-C (S1, S2) and F-G (S3). (N) Comparison between the nanorod-averaged turnover rates of two reactions (v_{AR}, v_{Rz}) and the ensemble-averaged anodic photocurrent i_{ss} of water oxidation catalyzed by TiO_2 nanorods. (O) i-E curves measured from spots S1, S2 and S3 before (solid line) and after (dashed line) OEC deposition. (P) Relative improvement of the absorbed-photon-to-current efficiency versus the initial efficiency. Open circles are individual spots on TiO_2 nanorods and black squares are averaged results. (Q) Same as (P) but for relative change of the onset potential vs. the initial value. Figures adapted from Sambur et al.[40] Copyright 2016 Nature Publishing Group.

1.4 Scope of this thesis

This dissertation focuses on using SMSR fluorescence microscopy to study heterogeneous catalysis. The high temporal resolution and high spatial resolution enable the catalytic characterizations at single-turnover sub-particle level, which are fully utilized to establish the structure-activity relationship of nanocatalysts.

Chapter 2 is a comprehensive study of PdAu bimetallic nanoparticle catalysis by super-resolution catalysis imaging, which benefits from the high spatial resolution of this technique. Compared with their monometallic counterparts, bimetallic nanoparticles often show enhanced catalytic activity associated with the bimetallic interface. Direct quantitation of catalytic activity at the bimetallic interface is important for understanding the enhancement mechanism, but challenging experimentally. Using single-molecule super-resolution catalysis imaging in correlation with electron microscopy, we report the first quantitative visualization of enhanced bimetallic activity within single bimetallic nanoparticles. We focus on heteronuclear bimetallic PdAu nanoparticles that present a well-defined Pd-Au bimetallic interface in catalyzing a photo-driven fluorogenic disproportionation reaction. Our approach also enables a direct comparison between the bimetallic and monometallic regions within the same nanoparticle. Theoretical calculations further provide insights into the electronic nature of N–O bond activation of the reactant (resazurin) adsorbed on bimetallic sites. Sub-particle activity correlation between bimetallic enhancement and monometallic activity suggests that the favorable locations to construct bimetallic sites are those monometallic sites with higher activity, leading to a strategy for making effective bimetallic nanocatalysts. The results highlight the power of super-resolution catalysis imaging in gaining insights that could help improve nanocatalysts.

Chapter 3 contains supplementary information to the bimetallic catalysis study presented in Chapter 2, which are: detailed sample preparations, complementary ensemble activity measurements, super-resolution imaging experiment setup and data analysis, finite-difference time-domain (FDTD) simulations, and density functional theory (DFT) calculations. The additional experiment results and analyses are also included in Chapter 3.

1.5 References

(1) Bell, A. T. The impact of nanoscience on heterogeneous catalysis. *Science* **2003**, *299*, 1688-1691.

(2) Zaera, F. Nanostructured materials for applications in heterogeneous catalysis. *Chem Soc Rev* **2013**, *42*, 2746-2762.

(3) IUPAC Compendium of Chemical Terminology - the Gold Book. http://goldbook.iupac.org/html/C/C00876.html.

(4) Valden, M.; Lai, X.; Goodman, D. W. Onset of catalytic activity of gold clusters on titania with the appearance of nonmetallic properties. *Science* **1998**, *281*, 1647-1650.

(5) Lee, I.; Delbecq, F.; Morales, R.; Albiter, M. A.; Zaera, F. Tuning selectivity in catalysis by controlling particle shape. *Nat Mater* **2009**, *8*, 132-138.

(6) Lim, B.; Jiang, M. J.; Camargo, P. H. C.; Cho, E. C.; Tao, J.; Lu, X. M.; Zhu, Y. M.; Xia, Y. N. Pd-Pt Bimetallic Nanodendrites with High Activity for Oxygen Reduction. *Science* **2009**, *324*, 1302-1305.

(7) Lei, Y.; Mehmood, F.; Lee, S.; Greeley, J.; Lee, B.; Seifert, S.; Winans, R. E.; Elam, J. W.; Meyer, R. J.; Redfern, P. C.; Teschner, D.; Schlogl, R.; Pellin, M. J.; Curtiss, L. A.; Vajda, S. Increased Silver Activity for Direct Propylene Epoxidation via Subnanometer Size Effects. *Science* **2010**, *328*, 224-228.

(8) Somorjai, G. A.; Contreras, A. M.; Montano, M.; Rioux, R. M. Clusters, surfaces, and catalysis. *P Natl Acad Sci USA* **2006**, *103*, 10577-10583.

(9) Xie, X. W.; Li, Y.; Liu, Z. Q.; Haruta, M.; Shen, W. J. Low-temperature oxidation of CO catalysed by Co3O4 nanorods. *Nature* **2009**, *458*, 746-749.

(10) Yang, X. F.; Wang, A. Q.; Qiao, B. T.; Li, J.; Liu, J. Y.; Zhang, T. Single-Atom Catalysts: A New Frontier in Heterogeneous Catalysis. *Accounts Chem Res* **2013**, *46*, 1740-1748.

(11) Sambur, J. B.; Chen, P. Approaches to Single-Nanoparticle Catalysis. *Annu Rev Phys Chem* **2014**, *65*, 395-422.

(12) Meier, J.; Friedrich, K. A.; Stimming, U. Novel method for the investigation of single nanoparticle reactivity. *Faraday Discuss* **2002**, *121*, 365-372.

(13) Chen, S. L.; Kucernak, A. Electrocatalysis under conditions of high mass transport rate: Oxygen reduction on single submicrometer-sized Pt particles supported on carbon. *J Phys Chem B* **2004**, *108*, 3262-3276.

(14) Janssen, K. P. F.; De Cremer, G.; Neely, R. K.; Kubarev, A. V.; Van Loon, J.; Martens, J. A.; De Vos, D. E.; Roeffaers, M. B. J.; Hofkens, J. Single molecule methods for the study of catalysis: from enzymes to heterogeneous catalysts. *Chem Soc Rev* **2014**, *43*, 990-1006.

(15) Chen, P.; Zhou, X. C.; Andoy, N. M.; Han, K. S.; Choudhary, E.; Zou, N. M.; Chen, G. Q.; Shen, H. Spatiotemporal catalytic dynamics within single nanocatalysts revealed by single-molecule microscopy. *Chem Soc Rev* **2014**, *43*, 1107-1117.

(16) Chen, T.; Dong, B.; Chen, K.; Zhao, F.; Cheng, X.; Ma, C.; Lee, S.; Zhang, P.; Kang, S. H.; Ha, J. W.; Xu, W.; Fang, N. Optical Super-Resolution Imaging of Surface Reactions. *Chemical reviews* **2017**, 7510-7537.

(17) Novo, C.; Funston, A. M.; Mulvaney, P. Direct observation of chemical reactions on single gold nanocrystals using surface plasmon spectroscopy. *Nat Nanotechnol* **2008**, *3*, 598-602.

(18) Eo, M.; Baek, J.; Song, H. D.; Lee, S.; Yi, J. Quantification of electron transfer rates of different facets on single gold nanoparticles during catalytic reactions. *Chem Commun* **2013**, *49*, 5204-5206.

(19) Heck, K. N.; Janesko, B. G.; Scuseria, G. E.; Halas, N. J.; Wong, M. S. Observing Metal-Catalyzed Chemical Reactions in Situ Using Surface-Enhanced Raman Spectroscopy on Pd-Au Nanoshells. *J Am Chem Soc* **2008**, *130*, 16592-16600.

(20) de Smit, E.; Swart, I.; Creemer, J. F.; Hoveling, G. H.; Gilles, M. K.; Tyliszczak, T.; Kooyman, P. J.; Zandbergen, H. W.; Morin, C.; Weckhuysen, B. M.; de Groot, F. M. F. Nanoscale chemical imaging of a working catalyst by scanning transmission X-ray microscopy. *Nature* **2008**, *456*, 222-225.

(21) Liu, N.; Tang, M. L.; Hentschel, M.; Giessen, H.; Alivisatos, A. P. Nanoantenna-enhanced gas sensing in a single tailored nanofocus. *Nat Mater* **2011**, *10*, 631-636.

(22) van Schrojenstein Lantman, E. M.; Deckert-Gaudig, T.; Mank, A. J. G.; Deckert, V.; Weckhuysen, B. M. Catalytic processes monitored at the nanoscale with tip-enhanced Raman spectroscopy. *Nat Nanotechnol* **2012**, *7*, 583-586.

(23) Klar, T. A.; Jakobs, S.; Dyba, M.; Egner, A.; Hell, S. W. Fluorescence microscopy with diffraction resolution barrier broken by stimulated emission. *P Natl Acad Sci USA* **2000**, *97*, 8206-8210.

(24) Dickson, R. M.; Cubitt, A. B.; Tsien, R. Y.; Moerner, W. E. On/off blinking and switching behaviour of single molecules of green fluorescent protein. *Nature* **1997**, *388*, 355-358.

(25) Rust, M. J.; Bates, M.; Zhuang, X. W. Sub-diffraction-limit imaging by stochastic optical reconstruction microscopy (STORM). *Nat Methods* **2006**, *3*, 793-795.

(26) Lu, H. P.; Xun, L. Y.; Xie, X. S. Single-molecule enzymatic dynamics. *Science* **1998**, *282*, 1877-1882.

(27) Chen, T. Y.; Santiago, A. G.; Jung, W.; Krzeminski, L.; Yang, F.; Martell, D. J.; Helmann, J. D.; Chen, P. Concentration- and chromosome-organization-dependent regulator unbinding from DNA for transcription regulation in living cells. *Nat Commun* **2015**, *6*, 7445.

(28) English, B. P.; Min, W.; van Oijen, A. M.; Lee, K. T.; Luo, G. B.; Sun, H. Y.; Cherayil, B. J.; Kou, S. C.; Xie, X. S. Ever-fluctuating single enzyme molecules: Michaelis-Menten equation revisited. *Nat Chem Biol* **2006**, *2*, 87-94.

(29) Zhou, X. C.; Andoy, N. M.; Liu, G. K.; Choudhary, E.; Han, K. S.; Shen, H.; Chen, P. Quantitative super-resolution imaging uncovers reactivity patterns on single nanocatalysts. *Nat Nanotechnol* **2012**, *7*, 237-241.

(30) Xu, W. L.; Kong, J. S.; Yeh, Y. T. E.; Chen, P. Single-molecule nanocatalysis reveals heterogeneous reaction pathways and catalytic dynamics. *Nat Mater* **2008**, *7*, 992-996.

(31) Moerner, W. E.; Fromm, D. P. Methods of single-molecule fluorescence spectroscopy and microscopy. *Rev Sci Instrum* **2003**, *74*, 3597-3619.

(32) Thompson, R. E.; Larson, D. R.; Webb, W. W. Precise nanometer localization analysis for individual fluorescent probes. *Biophys J* **2002**, *82*, 2775-2783.

(33) Roeffaers, M. B. J.; Sels, B. F.; Uji-i, H.; De Schryver, F. C.; Jacobs, P. A.; De Vos, D. E.; Hofkens, J. Spatially resolved observation of crystal-face-dependent catalysis by single turnover counting. *Nature* **2006**, *439*, 572-575.

(34) Andoy, N. M.; Zhou, X. C.; Choudhary, E.; Shen, H.; Liu, G. K.; Chen, P. Single-Molecule Catalysis Mapping Quantifies Site-Specific Activity and Uncovers Radial Activity Gradient on Single 2D Nanocrystals. *J Am Chem Soc* **2013**, *135*, 1845-1852.

(35) Decan, M. R.; Impellizzeri, S.; Marin, M. L.; Scaiano, J. C. Copper nanoparticle heterogeneous catalytic 'click' cycloaddition confirmed by single-molecule spectroscopy. *Nat Commun* **2014**, *5*, 4612.

(36) Ristanovic, Z.; Kerssens, M. M.; Kubarev, A. V.; Hendriks, F. C.; Dedecker, P.; Hofkens, J.; Roeffaers, M. B. J.; Weckhuysen, B. M. High-Resolution Single-Molecule Fluorescence Imaging of Zeolite Aggregates within Real-Life Fluid Catalytic Cracking Particles. *Angew Chem Int Edit* **2015**, *54*, 1836-1840.

(37) Tachikawa, T.; Yamashita, S.; Majima, T. Evidence for Crystal-Face-Dependent TiO2 Photocatalysis from Single-Molecule Imaging and Kinetic Analysis. *J Am Chem Soc* **2011**, *133*, 7197-7204.

(38) Zhang, Y. W.; Lucas, J. M.; Song, P.; Beberwyck, B.; Fu, Q.; Xu, W. L.; Alivisatos, A. P. Superresolution fluorescence mapping of single-nanoparticle catalysts reveals spatiotemporal variations in surface reactivity. *P Natl Acad Sci USA* **2015**, *112*, 8959-8964.

(39) Xu, W. L.; Shen, H.; Kim, Y. J.; Zhou, X. C.; Liu, G. K.; Park, J.; Chen, P. Single-Molecule Electrocatalysis by Single-Walled Carbon Nanotubes. *Nano Lett* **2009**, *9*, 3968-3973.

(40) Sambur, J. B.; Chen, T. Y.; Choudhary, E.; Chen, G. Q.; Nissen, E. J.; Thomas, E. M.; Zou, N. M.; Chen, P. Sub-particle reaction and photocurrent mapping to optimize catalyst-modified photoanodes. *Nature* **2016**, *530*, 77-80.

(41) Satterfield, C. N.: *Heterogeneous catalysis in practice*; McGraw-Hill: New York, 1980.

(42) Tachikawa, T.; Wang, N.; Yamashita, S.; Cui, S. C.; Majima, T. Design of a Highly Sensitive Fluorescent Probe for Interfacial Electron Transfer on a TiO2 Surface. *Angew Chem Int Edit* **2010**, *49*, 8593-8597.

CHAPTER TWO

BIMETALLIC EFFECT OF SINGLE NANOCATALYSTS VISUALIZED BY SUPER-RESOLUTION CATALYSIS IMAGING

2.1 Introduction

Bimetallic nanoparticles are an important class of nanoscale catalysts in heterogeneous catalysis; they are widely used in industry due to the enhanced catalytic properties (i.e. activity, selectively, stability) compared with their monometallic counterparts[1,2]. Many experimental and theoretical efforts have been spent in understanding the catalytic enhancements from the bimetallic effects[2-4]. Two general mechanisms are often found to operate: (1) electronic (a.k.a. ligand) effect, in which the electronic properties of the catalytically active metal could be tuned by the other metal, leading to enhancement in activity[5]; (2) geometric (a.k.a. ensemble) effect, where two metals together could form highly active surface sites made by an ensemble of atoms in some specific atomic arrangement[6,7]. It is often challenging to deconvolute completely these two effects. Nevertheless the catalytic enhancement, in both cases, is a result of direct metal-metal interactions at the atomic scale, i.e., involving interfacing two types of metal components directly.

A majority of the scientific insights into bimetallic effects of nanoparticle catalysts came from studies at the ensemble level, where a large number of nanoparticles are measured simultaneously[2-13]. By varying the composition of the bimetallic nanoparticles (typically alloy), the location, or the geometry of bimetallic sites, one could optimize the bimetallic catalysts for the largest activity enhancement. For such ensemble-averaged measurements, bimetallic nanocatalysts present particular challenges, however. First, these nanocatalysts are highly heterogeneous; their differences in catalytic activity are masked by the ensemble averaging. Second, even on a single bimetallic nanoparticle, there are both bimetallic and monometallic surface sites; the letter could contribute significant to the measured activity. Spatially resolved activity measurements within a single catalyst particle are thus desirable. A recent tip-enhanced Raman spectroscopy (TERS) imaging study showed that on a bimetallic PdAu surface, the Pd edge atoms better activate the reactant than the Pd terrace atoms on a Au(111) surface[14]. Although with high spatial resolution (~several nm), no quantitation of catalytic activity was available in such TERS imaging.

Single-molecule super-resolution fluorescence microscopy has emerged recently as an effective and complementary approach to study catalysis on nanoscale particles[15-26], including thermal catalysis[18-21], photocatalysis[22,23], electrocatalysis[24], and photoelectrocatalysis[25]. Individual nanocatalysts can be interrogated at nanometer spatial resolution and single-turnover temporal resolution in real time under operando conditions, where the activity differences among different nanoparticles or even among different surface sites on the same nanoparticle can be directly quantified.

Here we report the first single-molecule super-resolution imaging of the bimetallic effects within single nanoparticle catalysts, in particular single heteronuclear PdAu nanoparticles in catalyzing a photo-driven fluorogenic disproportionation reaction. The heteronuclear architecture allows for a clear definition of an interfacial region between the two metal components and a concurrent comparison with monometallic regions on the same particle. We directly visualize the enhanced activity at the bimetallic regions within individual PdAu nanoparticles. DFT calculations further provide insights into the mechanism of the enhanced activation of the reactant molecule at bimetallic vs. monometallic surface sites. The correlation between the catalytic activity of bimetallic and monometallic regions within the same particle reveals the desirable locations to form bimetallic sites, which could potentially guide the design of effective bimetallic nanocatalysts.

2.2 Results and discussions

2.2.1 PdAu nanoparticles can catalyze the photo-driven fluorogenic disproportionation reaction of resazurin.

We chose a heteronuclear PdAu bimetallic nanoparticle as a model bimetallic catalyst. Each PdAu nanoparticle consists of a penta-twinned crystalline Pd nanorod (~500-4000 nm in length and 25.5 ± 2.8 nm in diameter) with a pseudospherical Au nanoparticle (~60-140 nm in diameter) grown on one or both of its tips (Figure 2.1A and Figure 3.1)[27]. The heteronuclear architecture and the geometries of the two respective components enable ready identification of the interface between the two metals in each PdAu nanoparticle in later scanning electron microscopy (SEM) characterizations. Elemental line-profiling via energy dispersive spectroscopy confirms the heteronuclear nature with a clearly defined bimetallic junction between the Pd nanorod and the Au particle (Figure 2.1B).

We further coated the PdAu nanoparticles with a mesoporous silica shell of 114 ± 11 nm in thickness (Figure 2.1C), which allowed us to use UV-ozone to remove the organic ligands (e.g., polyvinylpyrrolidone (PVP)) on PdAu nanoparticles while maintaining their morphologies (especially the Pd-Au interface) and the accessibility of the metal surface to the reactant molecules via the mesopores[28,29]. $NaBH_4$ was then used to reduce the oxide layer on the metal to activate the surface for catalysis after UV-ozone treatment. In the subsequent imaging experiment, the mesoporous silica shell also facilitates the fluorescence detection of the catalytic product molecules, which adsorb temporarily on the walls of the mesopores, thus circumventing the possible fluorescence quenching associated with direct detection on metal surfaces (see Section 2.2.2 below). (Note: for simplicity, we use “PdAu nanoparticles” to refer to these mesoporous silica coated nanoparticles in the writing below unless specified otherwise.)

Past studies have shown that the non-fluorescent molecule resazurin (**Rz**$^{-}$), upon illumination with 532 nm light, can disproportionate to an one-electron reduced (**Rz**$^{2-\bullet}$) and an one-electron oxidized (**Rz**$^{\bullet}$) radial species[30], and the former one (**Rz**$^{2-\bullet}$) can further disproportionate to generate the highly fluorescent molecule resorufin (**Rf**$^{-}$) (two-electron reduced from **Rz**$^{-}$) and resazurin (**Rz**$^{-}$)[31]. Figure 2.1D gives the expected overall reaction equation. We have independently confirmed this photo-driven disproportionation reaction, and further determined its 3:1 reaction stoichiometry for **Rz**:**Rf** (Section 3.4.1 and 3.4.2). We found that the PdAu nanoparticles, as well as their monometallic components, can catalyze this photo-driven fluorogenic reaction (Figure

2.1E, and black line in inset, Section 3.4.1 and 3.4.2). Control experiments show that without the PdAu nanoparticle catalyst or light, the reaction is insignificant (Figure 2.1E inset, blue and green lines). Moreover, 488 nm light, which **Rz**$^-$ does not absorb but can excite the conduction band electrons of the metal (Figure 3.4E), cannot drive this reaction (Figure 2.1E inset, red line), indicating that the photoexcitation of the reactant **Rz**$^-$, rather than that of the metal, is a key step in the disproportionation reaction.

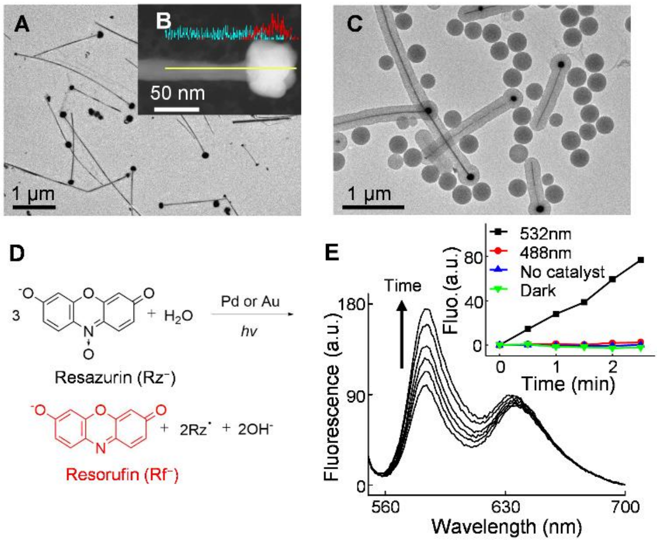

Figure 2.1 PdAu heteronuclear nanoparticles can catalyze photo-driven disproportionation reaction of resazurin to generate resorufin. (A) TEM image of heteronuclear bimetallic PdAu nanoparticles; structural measurements in Figure 3.1. (B) Elemental line profile on a PdAu nanoparticle. Cyan: Pd; red: Au. Yellow line: the position of line scanning. (C) TEM image of mesoporous silica coated PdAu nanoparticles. (D) Proposed chemical equation of photo-driven disproportionation reaction of resazurin (**Rz**$^-$) to resorufin (**Rf**$^-$) and a one-electron-oxidized radical species (**Rz**$^\bullet$) catalyzed by Pd or Au catalysts. (E) Fluorescence spectra of reaction solution containing 30.7 μM **Rz**$^-$ in 0.2 M pH 7.2 phosphate buffer in the presence of mesoporous

silica coated PdAu nanoparticles under 50 mW 532 nm laser illumination; the increase of fluorescence at 583 nm indicates the formation of **Rf**$^-$. Inset: the fluorescence intensity at 583 nm vs. time profile of the reaction solution with catalysts under 50 mW 532 nm illumination (black), under 50 mW 488 nm illumination (red), without catalyst under at 50 mW 532 nm excitation (blue), or with catalyst but no light illumination (green).

2.2.2 Single-molecule super-resolution catalysis imaging of single PdAu nanoparticles.

The fluorogenic nature of the photo-driven resazurin disproportionation allowed us to use single-molecule super-resolution fluorescence microscopy to image this reaction on individual PdAu nanoparticles, an approach we developed previously[28,29]. In this approach, the particles were dispersed on a quartz slide within a microfluidic reactor. A continuous flow of a reactant solution and a constant 532 nm laser illumination led to a steady-state catalytic kinetics. Using wide-field total internal reflection fluorescence (TIRF) microscopy, we imaged the fluorescence of the product resorufin at the single-molecule level and localized their positions individually with ~30-40 nm precision. The product molecules reside on the nanoparticle (i.e., adsorbed within the mesoporous silica shell) for ~20 ms on average (i.e., ~1 image frame) (Figure 3.7E) and do not show significant lateral diffusion (Section 3.5.2.1) before desorbing and disappearing into the surrounding solution. We further confirmed the identity of the product resorufin by measuring the fluorescence spectrum on single PdAu nanoparticles (Figure 3.6B).

Figure 2.2A shows an exemplary map of thousands of product molecules imaged and localized on a single PdAu nanoparticle; its rod shape is apparent. Subsequent imaging through SEM independently confirmed the heteronuclear bimetallic morphology of each particle (Figure 2.2B), in which the Au particle is clearly visible at the tip of the Pd nanorod.

We titrated the reactant concentration [$\mathbf{Rz}^{-}$] and the incident 532 nm laser power density *I*, and examined how the catalytic activity of individual PdAu nanoparticles depend on them. Over the course of these titrations, the catalytic activity of the particles showed no significant deactivation for ~6 hours (Figure 3.12A). We further accounted for potential changes in fluorescence detection efficiency due to changes in background noises during these titrations (Section 3.5.2.2).

With increasing [$\mathbf{Rz}^{-}$], the turnover rates of PdAu nanoparticles follow the classic Langmuir saturation kinetics for heterogeneous catalysis, both at the single-particle level and after ensemble averaging (Figure 2.2F), further supporting that the catalysis here is mediated on metal surfaces. With increasing *I*, the turnover rates of individual particles increase linearly (Figure 2.2F), in contrast to the quadratic power dependence of the un-catalyzed photo-driven disproportionation reaction (Figure 3.4F). This linear power dependence suggests that the rate-limiting step of the catalytic reaction merely involves one photo-excited reactant molecule resazurin ($\mathbf{Rz}^{-}\mathbf{*}$).

Taking together all above results, we formulated a working kinetic mechanism of the catalytic disproportionation (Figure 2.2E; details in Section 3.5.4). The reduction part of disproportionation is imaged directly in our experiments, in which a surface-adsorbed photo-excited resazurin (M^{n}–$\mathbf{Rz}^{-}\mathbf{*}$, n is the number of electrons on the metal catalyst particle) obtained two electrons from the catalyst to generate resorufin (**Rf**$^-$). For the oxidation part, which is not directly measured, we proposed it is a surface-adsorbed excited-state resazurin that donates one electron to the metal catalyst generating a neutral radical (Rz$^\bullet$), giving the overall reaction as that in Figure 2.1D. This mechanism gives the catalytic turnover rate v as (derivation in Section 3.5.4):

$$v = I\frac{kK[\mathrm{Rz}^-]}{1+K[\mathrm{Rz}^-]} \tag{2.1}$$

Here k is a catalytic rate constant and K is a reactant adsorption equilibrium constant on the metal surface. This equation predicts the saturating kinetics on [**Rz**$^-$] and the linear dependence on I, as observed experimentally (Figure 2.2F). By globally fitting both [**Rz**$^-$] and I dependences of v, we extracted k and K of PdAu nanoparticles at both the single-particle and the ensemble-averaged level.

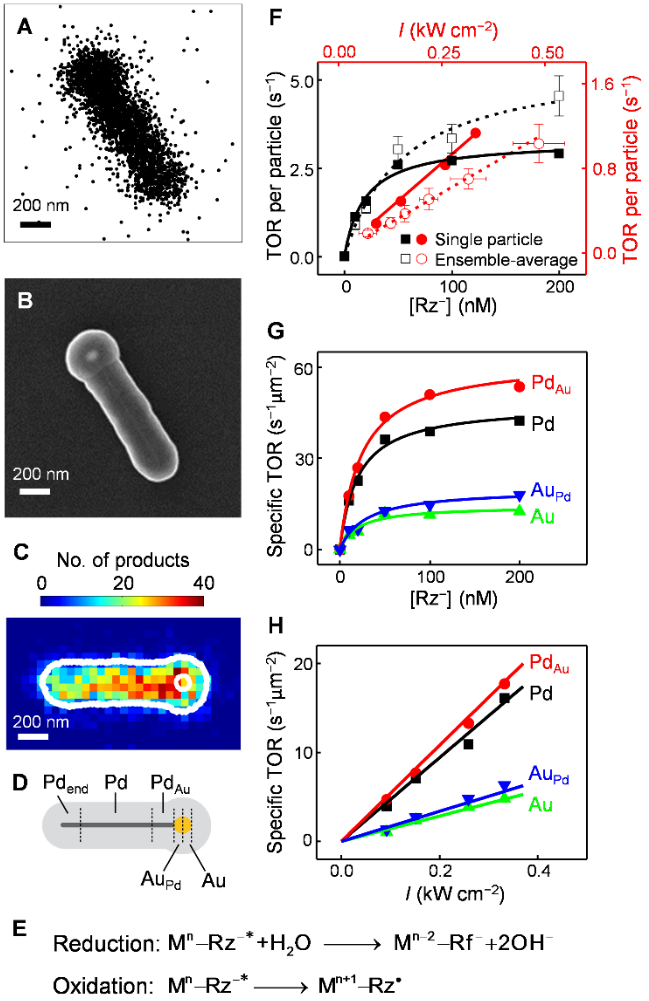

Figure 2.2 Super-resolution catalysis imaging and single-to-sub particle level analysis of reaction kinetics of PdAu nanoparticles. (A) Positions of ~2900 products detected on a single mesoporous silica coated PdAu nanoparticle. (B) SEM image of the nanoparticle in A. (C) Two-dimensional histogram of product positions on the nanoparticle in A-B in 50 × 50 nm^2 bins. The nanoparticle has been reoriented to align horizontally. Outer white line: structural contour; white circle: the contour of the Au particle; both determined from the SEM image in B. (D) Segmentation of a typical PdAu nanoparticle: regions of monometallic Pd (Pd), Au-doped Pd next to the Pd-Au interface (Pd$_{Au}$), monometallic Au (Au), and Pd-doped Au next to the Pd-Au interface (Au$_{Pd}$).

The end segment (Pd_{end}) is described in Section 2.2.6. (E) Proposed kinetic mechanism of the catalytic disproportionation. M^n–$\mathbf{Rz}^{-*}$: a metal-surface-adsorbed excited-state resazurin; n is the number of electrons on the metal; the changes in electron counts on the metal particle are denoted. (F) Reactant concentration [$\mathbf{Rz}^-$] (black) and 532 nm laser power density *I* (red) dependences of the turnover rate (TOR) per PdAu nanoparticle. Solid symbols: the single particle in A-C; open symbols: results averaged over 53 nanoparticles. Error bars: s.e.m. for *y* and s.d. for *x*. Solid and dashed lines: global fits of Equation (2.1). (G-H) [$\mathbf{Rz}^-$] and *I* dependences of specific turnover rates of the segments (Pd, Pd_{Au}, Au, Au_{Pd}) for the nanoparticle in A-C.

2.2.3 Sub-particle analysis reveals enhanced catalytic activity around the Pd-Au interface.

The unique patterns of nanoparticles allowed us to overlay their super-resolution catalysis images onto their respective SEM images with ~40 nm precision (Figure 2.2C; and Figure 3.10), on which the Pd-Au interface of the heteronuclear particle can be readily located in reference to the Au particle position. A higher catalytic activity (i.e., more reaction products) is apparent around the interfacial region (Figure 2.2C), suggesting a direct, and first-of-its-kind, visualization of bimetallic effect of catalytic enhancement.

We then dissected each heteronuclear PdAu nanoparticle into four different regions (Figure 2.2D): (1) a 100-nm long segment of the Pd nanorod adjacent to the interface, i.e., Pd_{Au} region, corresponding to a bimetallic component that is dominantly

Pd with minor Au doping on the surface from the attached Au particle (Figure 2.1B); (2) the rest of Pd nanorod away from the interface (excluding the other end of the Pd nanorod), representing the monometallic Pd component; (3) the Au hemisphere adjacent to the interface, i.e., Au_{Pd} region, corresponding to the other bimetallic component that is dominantly Au with minor Pd doping (Figure 2.1B); and (4) the other hemisphere of Au, representing the monometallic Au component. The dimensions of all four regions are significantly larger than our spatial resolution (30-40 nm) to make these sub-particle dissections physically meaningful. The specific catalytic rates of all four regions show saturation kinetics with increasing reactant concentration [$\mathbf{Rz}^-$] and a linear dependence on the light power density I (Figure 2.2G, H), as observed for the whole particle (Figure 2.2F). Fitting these results with Equation (2.1) gave the catalytic rate constant k and the reactant adsorption equilibrium constant K of each region for each PdAu nanoparticle.

Pooling results from 53 PdAu nanoparticles, the catalytic rate constant k of the bimetallic Pd_{Au} and Au_{Pd} regions are ~50% more active on average than their monometallic Pd and Au counterparts (Figure 2.3A and Figure 3.12B), directly reporting bimetallic catalytic enhancement. On the other hand, the reactant adsorption equilibrium constant K shows an opposite trend: the K of bimetallic regions are ~30% smaller on average than their monometallic counter parts (Figure 2.3B). Furthermore, for each type of regions, the k and K of individual PdAu nanoparticles are anti-correlated (Figure 2.3C, D). Therefore, the enhanced catalytic activity at bimetallic regions is associated with weakened reactant adsorption, rationalizable by transition state theory, in which a less stable reactant is closer in energy to the transition state resulting in a lower activation barrier.

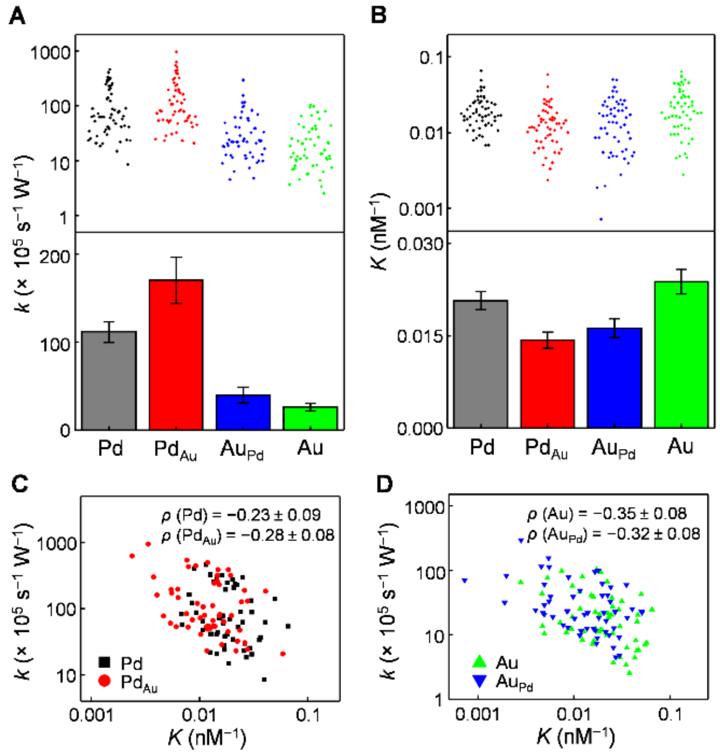

Figure 2.3 Sub-particle catalytic properties of bimetallic vs. monometallic regions. (A, B) The catalytic rate constant *k* (A) and reactant adsorption equilibrium constant *K* (B) of the bimetallic regions (Pd_{Au}, Au_{Pd}) vs. monometallic regions (Pd, Au). Upper: results of individual nanoparticles; each dot is one PdAu nanoparticle. Lower: ensemble averages; error bars are s.e.m. (C, D) Scatter plots of *k* vs. *K* for each type of regions of individual PdAu nanoparticles; each dot is one region from one PdAu nanoparticle. ρ is the Pearson's cross correlation coefficient.

Control measurements and analyses show that: (1) The mesoporous silica shell of the bimetallic and monometallic regions present equal accessibility to the reactant molecules (Figure 3.12E). (2) The fluorescence intensities and dwell times of the reaction products at the bimetallic regions are indistinguishable from those at the monometallic regions, and therefore the products are equally detected at different regions on the same nanoparticle (Figure 3.12D, F). And (3) the plasmonic enhancement effect is insignificant at the bimetallic regions (Section 3.6). Altogether, these results support that the observed higher product detection rates at interfacial regions are indeed due to the bimetallic catalytic enhancement there.

2.2.4 Breaking the metal-metal junction abolishes the enhanced catalytic activity at bimetallic regions.

To further support that the enhanced catalytic activity is indeed related to the Pd-Au interface in the heteronuclear PdAu nanoparticle, we broke the Pd-Au junction by heating the PdAu nanoparticles at 450 ℃ for 1 hour. A nanoscale gap appears between the Pd nanorod and the Au nanoparticle within the mesoporous silica shell (Figure 2.4A; more examples in Figure 3.3).

We then imaged these PdAu nanoparticles with nanoscale gaps (i.e., gap-PdAu nanoparticles) in catalyzing the same reaction (Figure 2.4C; and Figure 3.14A), and with SEM, in which the gaps are visible (Figure 2.4D; and Figure 3.14B). Strikingly, the enhanced catalytic activity originally around the Pd-Au interface vanished, supporting that the enhanced catalytic activity is specific to the heteronuclear bimetallic structure with direct Pd-Au contact.

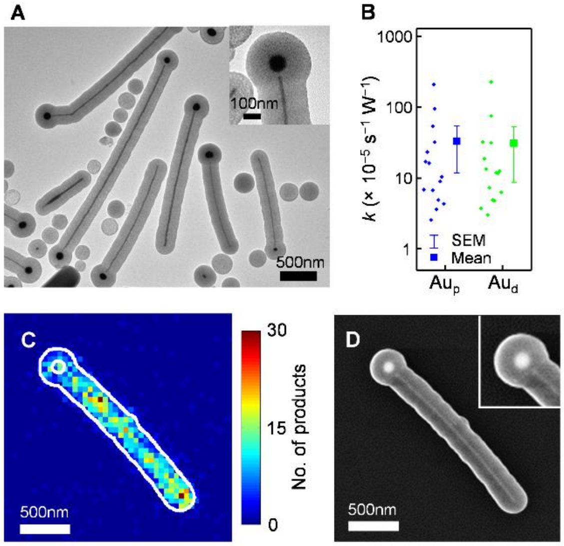

Figure 2.4 Super-resolution catalysis imaging of PdAu nanoparticles with nanoscale gaps (gap-PdAu nanoparticles). (A) TEM image of gap-PdAu nanoparticles coated with mesoporous silica. Inset: a zoom-in. (B) Box plot of the catalytic rate constant *k* of the proximal (Au_p) and distant (Au_d) Au hemispheres with regard to the Pd nanorods in the gap-PdAu nanoparticles. (C) Two-dimensional histogram of ~2500 product locations on a gap-PdAu nanoparticle. White line: structural contours of the outer shell and the spherical Au particle. (D) SEM image of the gap-PdAu nanoparticle in C. Inset: zoom-in of the nano-gap.

Since the spherical Au particles are easily identifiable in the SEM images of these gap-PdAu nanoparticles, onto which the super-resolution catalysis images were mapped (Figure 2.4C-D), we compared the catalytic kinetics of the Au hemisphere proximal to the Pd nanorod (i.e., Au_p) with the other hemisphere distant from the nanorod (i.e., Au_d). (We could not reliably dissect out a Pd nanorod segment proximal to the Au particle because the nanorod end at the gap cannot be clearly located in the SEM image). No significant differences in the catalytic rate constants were observed between the two hemispheres (Figure 2.4B) (nor in the reactant adsorption equilibrium constant *K*; Figure 3.14C), further supporting that the enhanced catalytic activity originally around the interface region is specific to the intact heteronuclear PdAu bimetallic structure.

It is worth noting that heat-breaking the Pd-Au junction should have left some Pd atoms on the Au particle, and therefore the proximal Au hemisphere should still behave like a Au_{Pd} region. However, the heating could have homogenized the structural and compositional differences between the two hemispheres. In any case, the abolishment of observable catalytic enhancement after breaking the junction supports that the enhancement is associated with the particular geometry with direct Pd-Au contact.

2.2.5 Electronic structure elucidation of reactant activation on monometallic and bimetallic surfaces.

Resazurin interaction with Pd and PdAu surfaces. We performed DFT calculations using the VASP package[32] to gain more insights into the activation on Pd, Au, or bimetallic surface sites of resazurin's N–O bond, which is cleaved to become resorufin (Figure 2.1D; calculation details in Sections 3.7.1-3.7.3). Although the photo-driven disproportionation of resazurin involves its excited state (Figure 2.2E), these ground-state DFT calculations could still inform on how resazurin's N–O bond gets activated upon interaction with metal surfaces. We first examined resazurin interaction with a Pd(100) surface, the dominant facets on the sides of Pd nanorods[27]. The optimized adsorption geometry has resazurin lying flat on the surface (Figure 2.5A). The N–O fragment of resazurin is tilted away from the surface, in which the O atom sits approximately above the center of four Pd atoms and the N atom is above an edge bridging two Pd atoms. Importantly, compared with that in the free resazurin molecule, the N–O bond is elongated by 0.007 Å (Table 3.2), reflecting its weakening and thus activation for cleavage, consistent with Pd's being a catalyst for the observed reaction.

We performed crystal orbital Hamiltonian population (COHP) analysis[33] to examine the interactions between the N–O fragment of resazurin and the Pd surface. COHP analysis allows for an energy-resolved visualization of bonding and antibonding orbital interactions between specific atoms (Figure 2.5C). The interactions mainly come from two types of Pd–O bonding interactions (Figure 2.5C, red shades below the Fermi level). One type involves N–O bonding orbitals (Figure 2.5C, blue line), located energetically below the Pd *d* band (at about −14 to −11.5 eV); this type of interaction is referred to as forward-donation[34]. The other type involves N–O antibonding orbitals, located energetically within the Pd *d* band (at about –7.6 to –6.6 eV); this type is referred to as back-donation[34].

We further performed DFT calculations using the Gaussian package[35] to visualize the molecular orbitals of resazurin (Section 3.7.6). Two N–O fragment based orbitals are identified to be likely involved in the forward- and back-donations between the N–O fragment and the Pd surface (Section 3.7.6): one a doubly occupied π bonding orbital, denoted as $\pi_{N–O}$ (Figure 2.5E); the other an unoccupied π^* orbital, denoted as

$\pi^*_{N–O}$ (Figure 2.5F). Both $\pi_{N–O}$ and $\pi^*_{N–O}$ have orbital lobes on the O atom pointing toward the Pd surface for bonding interactions.

Combining the adsorption geometry, the COHP analysis, and the resazurin MOs, we schematically depicted the forward-donation and back-donation interactions between Pd and the O atom of resazurin, labeled as $\pi_{N–O} + d$ and $d + \pi^*_{N–O}$, respectively (Figure 2.5G, H). Both types of interactions weaken the N–O bond of resazurin, consistent with the elongated N–O bond of resazurin adsorbed on the Pd(100) surface. But these two interactions have opposite charge transfer directions: the forward-donation takes away charge density from a N–O π bonding orbital, whereas the back-donation injects charge density into a N–O π* antibonding orbital; the net charge transfer is from Pd to the N–O fragment (Table 3.2), indicating the back-donation is a more dominant bonding interaction here.

To computationally evaluate how bimetallic sites can possibly enhance the activation of resazurin's N–O bond for cleavage, we substituted by Au the eight surface Pd atoms (numbered in Figure 2.5A) that directly interact with the carbon atoms of resazurin. The substitution was done one atom at time to dissect the effect of each substitution in forming bimetallic Au@Pd(100) surface sites, on which resazurin adsorption was further geometry optimized. No significant change of the resazurin adsorption geometry is observed on these model bimetallic surfaces (Section 3.7.3.1). Among the eight structures on these Au@Pd(100) surfaces, one of the most stable structures is a Au substitution at the Pd atom no. 2 (Figure 2.5A), which is far from the N–O fragment of the resazurin. Here the O of N–O is closer to the metal surface and

N–O is further elongated compared to that on Pd(111) (Table 3.2), indicating a more weakened N–O bond and likely a bimetallic effect of enhancing the activation of the N–O bond for cleavage, even though the second metal (i.e., Au here) is not directly bonded to the N–O fragment. COHP analysis identified the same forward- and back-donation interactions between Pd and O atoms (Figure 3.22A). More important, both interactions increase in magnitude compared with those on monometallic Pd(100) (Table 3.4), consistent with the further weakening and thus enhanced activation of the N–O bond for cleavage on bimetallic Pd_{Au} surfaces.

Resazurin interactions with Au and Au_{Pd} surfaces. We performed similar calculations of resazurin adsorption on a Au(111) surface. Au(111) surface was chosen as a model because the capping ligands PVP and iodide, used in the synthesis, prefer Au(111) facet sites in growing Au nanoparticles[36,37]. The optimized adsorption geometry has resazurin lies flat on the surface with 4 of its carbons and the O atom of the N–O fragment sitting on top of Au atoms (Figure 2.5B). Moreover, the N–O fragment is tilted toward the Au surface, suggesting strong interactions between Au and the N–O fragment; this is in contrast to that of resazurin-Pd(100) interactions where the N–O fragment is not directly on top of any Pd atom and is titled away from the surface (Figure 2.5A). The N–O bond is also elongated (by 0.006 Å) on Au(111) compared with that in the free resazurin (Table 3.3), indicating a weakening of the N–O bond and thus activation toward cleavage.

Similarly, we did single Pd atom substitutions for the five Au atoms sitting directly below the resazurin atoms (Figure 2.5B) to evaluate the bimetallic effect. All five substitutions lead to shorter metal–O bonds (by ~0.1 Å) compared with that on the Au(111) surface (Table 3.3), indicating even stronger interactions between the bimetallic surface and the N–O fragment. All of them also have further elongated N–O bond, indicating its enhanced activation via bimetallic effect.

COHP analysis of resazurin on Au(111) identified forward- and back-donation interactions between Au and the O atom of the N–O fragment (Figure 2.5D), as in resazurin-Pd(100) interactions. The orbital overlap pattern here is different, as the O atom here sits directly on top of a Au atom (Figure 2.5I, J). The local net charge transfer is from Au to the N–O fragment, indicating the back-donation is also more important here (Table 3.3). For the bimetallic surface Pd@Au(111), the COHP analysis also shows that both forward- and back-donation interactions increase between the metal and the N–O fragment (Table 3.4), leading to further activation of N–O.

Altogether, DFT calculations show that both substituting Pd by Au on Pd(100) and substituting Au by Pd on Au(111) could give a more lengthened N–O bond, from increases in both forward- and back-donation interactions, leading to the enhanced activation of the N–O bond for cleavage on the bimetallic surfaces.

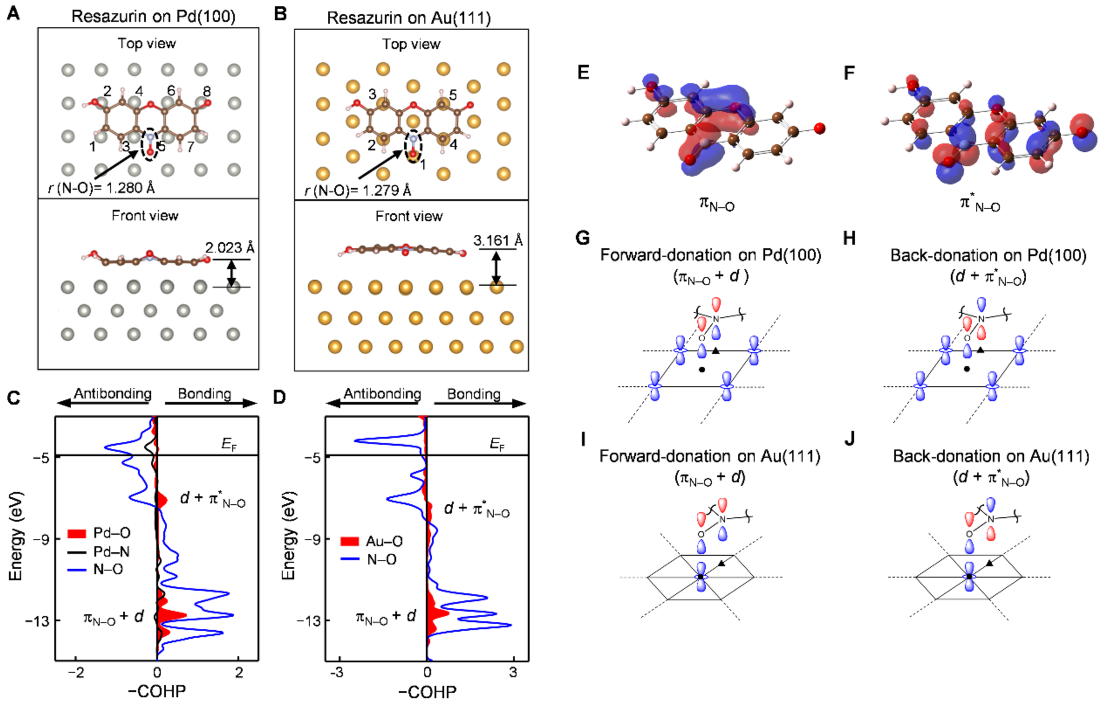

Figure 2.5 Electronic interactions of resazurin with Pd and Au surfaces. (A, B) Optimized adsorption geometries of resazurin on Pd(100) and Au(111). The Pd or Au atoms to be substituted for evaluating bimetallic effects are numbered. (C, D) COHP analyses for the interactions between the N–O fragment of resazurin and the closest metal atoms on Pd(100) and Au(111), respectively. The horizontal lines represent the Fermi-level (E_F), referenced to the vacuum (E = 0). (E, F) The molecular orbitals of resazurin that are dominantly π_{N-O} (doubly occupied) and π^*_{N-O} (unoccupied) in nature. (G, H) Schematics of the forward-donation and back-donation on Pd(100). (I, J) Schematics of the forward-donation and back-donation on Au(111). Only the N–O fragment of resazurin is drawn. We use d_{z^2} to represent d-orbitals of metal since they are pointed toward N–O. The solid circles and triangles mark the projected positions of O and N on the metal surface, respectively.

2.2.6 Activity correlation within single particle reveals optimal locations for bimetallic sites.

Our sub-particle level activity quantitation also allowed us to examine how the activity enhancements of the bimetallic regions are related to the activity of the corresponding monometallic regions within the same particle (Figure 2.6A, B, black and red points); the latter would represent the original "monometallic" activity of the bimetallic region before the second metal was introduced. Strikingly, positive correlations are clearly observed. For the particles whose monometallic Pd region has higher catalytic rate constant k, their bimetallic activity enhancement Δk_{BI} (defined as $k(\mathrm{Pd_{Au}}) - k(\mathrm{Pd})$) of the bimetallic $\mathrm{Pd_{Au}}$ region is also larger (Figure 2.6A). Same trend applies to the bimetallic $\mathrm{Au_{Pd}}$ region (Figure 2.6B). These trends indicate that when the particle, Pd or Au, is more active, the bimetallic enhancement is larger.

As a control, we also analyzed the corresponding sub-particle regions of pure single Pd nanorods and single Au particles, which are minor components in the sample and imaged together with PdAu bimetallic nanoparticles. For each Pd nanorod, we compared the activity of the end regions adjacent to the two tips (which are at the same location as the bimetallic $\mathrm{Pd_{Au}}$ region in a PdAu nanoparticle) to the side activity (excluding the ends), which corresponds to the monometallic Pd region in a PdAu nanoparticle. For each Au nanoparticle, we arbitrarily dissected it into two hemispheres vertically and compared the left vs. right hemisphere. Neither of the two controls shows any significant correlation (Figure 2.6A, B, pink points), indicating that possible intraparticle activity heterogeneity would not give the observed positive correlations between the bimetallic activity enhancement and the original monometallic activity.

These positive correlations suggest that to obtain larger bimetallic activity enhancement, one should deposit the second metal onto originally more active monometallic surface sites of Pd or Au, constituting a possible rationalized strategy in making more active bimetallic nanoparticle catalysts. Implementing this strategy would require one to (1) identify what types of surface sites are more active on the initial monometallic particle, and (2) selectively deposit the second metal onto the more active sites of the first metal.

Structurally anisotropic nanoparticles, such as 1-dimensional nanorods, offer opportunities to fulfil these two requirements. Regarding requirement (1), our previous study has identified that for Au nanorods, their two ends are generally more active than their side facets in catalyzing an oxidative deacetylation reaction, possibly due to the higher activity of low coordination surface sites abundant at the ends[28]. Here we found the same phenomenon on Pd nanorods: their free end segment Pd_{end} (Figure 2.2D) in the heteronuclear PdAu bimetallic particle is more active than their side facets (Figure 2.6C). Regarding requirement (2), one could utilize appropriate capping ligands that could selectively bind to the side facets of the first metal nanorods, leaving the two ends preferentially for the deposition of the second metal (Figure 2.6D). (Note for generating just bimetallic Pd_{Au} sites, the deposition of Au would certainly needs to be much less in quantity to not grow a big Au particle). Subsequent removal of the capping ligands would result in a bimetallic system where the second metal is at the desired higher activity sites of the first metal. Interestingly, this scheme is what underlies the synthesis of the heteronuclear bimetallic PdAu nanorod-nanoparticle in the current study, in which the Au particle grew selectively at the ends of Pd nanorods and the side-facets of Pd nanorods were preferentially blocked by the PVP and iodide ligands[27]. Similar strategies have been reported in synthesizing Pd-tipped Au nanorods[38] and Pd-edged Ag nanocubes[39] for detecting catalytic products via surface-enhanced Raman scattering, and Pt-tipped Au nanorods for surface-plasmon-enhanced catalysis[40]. With appropriate ligands, one could expect this synthesis strategy to be applicable to particles that are less structurally anisotropic (e.g., pseudospheres) for generating bimetallic sites at desired locations.

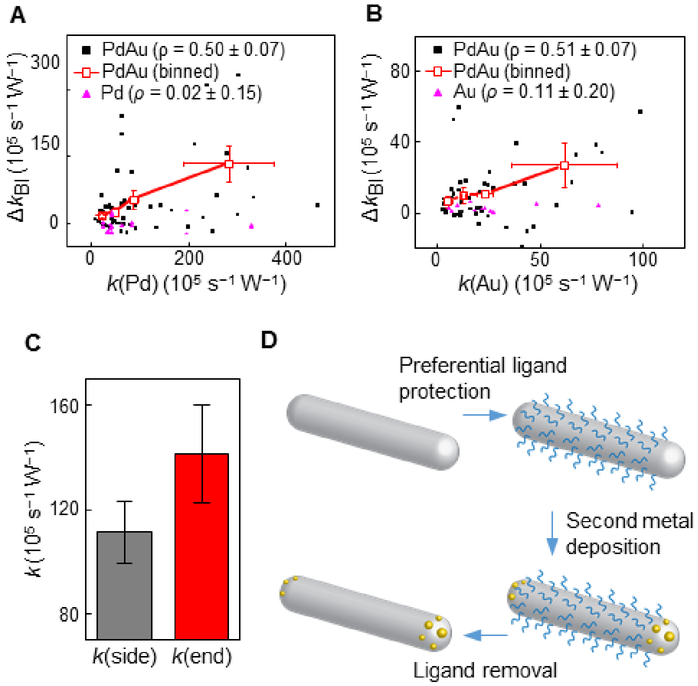

Figure 2.6 Rational strategy for generating more active bimetallic PdAu nanocatalysts. (A) Correlation between the catalytic activity enhancement of the bimetallic Pd_{Au} region and the monometallic Pd region on the same heteronuclear PdAu nanoparticle. Each black dot is a single PdAu nanoparticle. Hollow red squares are binned and averaged

results. The pure single Pd nanorods (pink) serve as the control. ρ is the Pearson's correlation coefficient for the individual particles. (B) Same as A, but for the bimetallic Au_{Pd} vs. the monometallic Au regions with pure Au nanoparticles (pink) as the control. (C) The catalytic rate constant k of the side and end regions of Pd nanorods (average from 46 nanoparticles). (D) Schematic of the proposed strategy to deposit the second metal onto the ends of nanorods of the first metal. Error bars are s.e.m. for all y-axes and s.d. for all x-axes.

2.3 Conclusions

In summary, using single-molecule super-resolution catalysis imaging in correlation with SEM, we have directly visualized and quantified the bimetallic activity enhancement on heteronuclear PdAu nanoparticles at the sub-particle level in catalyzing the photo-driven disproportionation of resazurin. DFT calculations provide insights into the electronic nature of the activation of the resazurin N–O bond on the metal surfaces via synergistic forward- and back-donation interactions. The results further suggest that higher activity monometallic sites are optimal location to form bimetallic sites for larger activity enhancement, demonstrating the effectiveness of the super-resolution catalysis imaging approach in deriving knowledge for guiding the development of better nanocatalysts.

2.4 References

(1) Bartholomew, C. H.; Farrauto, R. J.: *Fundamentals of industrial catalytic processes*; 2nd ed.; Wiley: Hoboken, N.J., 2006.

(2) Gilroy, K. D.; Ruditskiy, A.; Peng, H. C.; Qin, D.; Xia, Y. N. Bimetallic Nanocrystals: Syntheses, Properties, and Applications. *Chem Rev* **2016**, *116*, 10414-10472.

(3) Norskov, J. K.; Abild-Pedersen, F.; Studt, F.; Bligaard, T. Density functional theory in surface chemistry and catalysis. *P Natl Acad Sci USA* **2011**, *108*, 937-943.

(4) Yu, W. T.; Porosoff, M. D.; Chen, J. G. G. Review of Pt-Based Bimetallic Catalysis: From Model Surfaces to Supported Catalysts. *Chem Rev* **2012**, *112*, 5780-5817.

(5) Bligaard, T.; Norskov, J. K. Ligand effects in heterogeneous catalysis and electrochemistry. *Electrochim Acta* **2007**, *52*, 5512-5516.

(6) Maroun, F.; Ozanam, F.; Magnussen, O. M.; Behm, R. J. The role of atomic ensembles in the reactivity of bimetallic electrocatalysts. *Science* **2001**, *293*, 1811-1814.

(7) Chen, M. S.; Kumar, D.; Yi, C. W.; Goodman, D. W. The promotional effect of gold in catalysis by palladium-gold. *Science* **2005**, *310*, 291-293.

(8) Chen, G. X.; Zhao, Y.; Fu, G.; Duchesne, P. N.; Gu, L.; Zheng, Y. P.; Weng, X. F.; Chen, M. S.; Zhang, P.; Pao, C. W.; Lee, J. F.; Zheng, N. F. Interfacial Effects in Iron-Nickel Hydroxide-Platinum Nanoparticles Enhance Catalytic Oxidation. *Science* **2014**, *344*, 495-499.

(9) Guo, X. G.; Fang, G. Z.; Li, G.; Ma, H.; Fan, H. J.; Yu, L.; Ma, C.; Wu, X.; Deng, D. H.; Wei, M. M.; Tan, D. L.; Si, R.; Zhang, S.; Li, J. Q.; Sun, L. T.; Tang, Z. C.; Pan, X. L.; Bao, X. H. Direct, Nonoxidative Conversion of Methane to Ethylene, Aromatics, and Hydrogen. *Science* **2014**, *344*, 616-619.

(10) Kim, D.; Resasco, J.; Yu, Y.; Asiri, A. M.; Yang, P. D. Synergistic geometric and electronic effects for electrochemical reduction of carbon dioxide using gold-copper bimetallic nanoparticles. *Nat Commun* **2014**, *5*, 4948.

(11) Zhang, S. R.; Nguyen, L.; Liang, J. X.; Shan, J. J.; Liu, J. Y.; Frenkel, A. I.; Patlolla, A.; Huang, W. X.; Li, J.; Tao, F. Catalysis on singly dispersed bimetallic sites. *Nat Commun* **2015**, *6*, 7938.

(12) Zhang, H. J.; Watanabe, T.; Okumura, M.; Haruta, M.; Toshima, N. Catalytically highly active top gold atom on palladium nanocluster. *Nat Mater* **2012**, *11*, 49-52.

(13) Cordes, T.; Blum, S. A. Opportunities and challenges in single-molecule and single-particle fluorescence microscopy for mechanistic studies of chemical reactions. *Nat Chem* **2013**, *5*, 993-999.

(14) Zhong, J. H.; Jin, X.; Meng, L. Y.; Wang, X.; Su, H. S.; Yang, Z. L.; Williams, C. T.; Ren, B. Probing the electronic and catalytic properties of a bimetallic surface with 3 nm resolution. *Nat Nanotechnol* **2017**, *12*, 132-136.

(15) Janssen, K. P. F.; De Cremer, G.; Neely, R. K.; Kubarev, A. V.; Van Loon, J.; Martens, J. A.; De Vos, D. E.; Roeffaers, M. B. J.; Hofkens, J. Single molecule methods for the study of catalysis: from enzymes to heterogeneous catalysts. *Chem Soc Rev* **2014**, *43*, 990-1006.

(16) Chen, P.; Zhou, X. C.; Andoy, N. M.; Han, K. S.; Choudhary, E.; Zou, N. M.; Chen, G. Q.; Shen, H. Spatiotemporal catalytic dynamics within single nanocatalysts revealed by single-molecule microscopy. *Chem Soc Rev* **2014**, *43*, 1107-1117.

(17) Chen, T.; Dong, B.; Chen, K.; Zhao, F.; Cheng, X.; Ma, C.; Lee, S.; Zhang, P.; Kang, S. H.; Ha, J. W.; Xu, W.; Fang, N. Optical Super-Resolution Imaging of Surface Reactions. *Chem Rev* **2017**, 7510-7537.

(18) Roeffaers, M. B. J.; Sels, B. F.; Uji-i, H.; De Schryver, F. C.; Jacobs, P. A.; De Vos, D. E.; Hofkens, J. Spatially resolved observation of crystal-face-dependent catalysis by single turnover counting. *Nature* **2006**, *439*, 572-575.

(19) Xu, W. L.; Kong, J. S.; Yeh, Y. T. E.; Chen, P. Single-molecule nanocatalysis reveals heterogeneous reaction pathways and catalytic dynamics. *Nat Mater* **2008**, *7*, 992-996.

(20) Decan, M. R.; Impellizzeri, S.; Marin, M. L.; Scaiano, J. C. Copper nanoparticle heterogeneous catalytic 'click' cycloaddition confirmed by single-molecule spectroscopy. *Nat Commun* **2014**, *5*, 4612.

(21) Ristanovic, Z.; Kerssens, M. M.; Kubarev, A. V.; Hendriks, F. C.; Dedecker, P.; Hofkens, J.; Roeffaers, M. B. J.; Weckhuysen, B. M. High-Resolution Single-Molecule Fluorescence Imaging of Zeolite Aggregates within Real-Life Fluid Catalytic Cracking Particles. *Angew Chem Int Edit* **2015**, *54*, 1836-1840.

(22) Tachikawa, T.; Yamashita, S.; Majima, T. Evidence for Crystal-Face-Dependent TiO2 Photocatalysis from Single-Molecule Imaging and Kinetic Analysis. *J Am Chem Soc* **2011**, *133*, 7197-7204.

(23) Zhang, Y. W.; Lucas, J. M.; Song, P.; Beberwyck, B.; Fu, Q.; Xu, W. L.; Alivisatos, A. P. Superresolution fluorescence mapping of single-nanoparticle catalysts reveals spatiotemporal variations in surface reactivity. *P Natl Acad Sci USA* **2015**, *112*, 8959-8964.

(24) Xu, W. L.; Shen, H.; Kim, Y. J.; Zhou, X. C.; Liu, G. K.; Park, J.; Chen, P. Single-Molecule Electrocatalysis by Single-Walled Carbon Nanotubes. *Nano Lett* **2009**, *9*, 3968-3973.

(25) Sambur, J. B.; Chen, T. Y.; Choudhary, E.; Chen, G. Q.; Nissen, E. J.; Thomas, E. M.; Zou, N. M.; Chen, P. Sub-particle reaction and photocurrent mapping to optimize catalyst-modified photoanodes. *Nature* **2016**, *530*, 77-80.

(26) Esfandiari, N. M.; Blum, S. A. Homogeneous vs heterogeneous polymerization catalysis revealed by single-particle fluorescence microscopy. *J Am Chem Soc* **2011**, *133*, 18145-18147.

(27) Huang, X. Q.; Zheng, N. F. One-Pot, High-Yield Synthesis of 5-Fold Twinned Pd Nanowires and Nanorods. *J Am Chem Soc* **2009**, *131*, 4602-4603.

(28) Zhou, X. C.; Andoy, N. M.; Liu, G. K.; Choudhary, E.; Han, K. S.; Shen, H.; Chen, P. Quantitative super-resolution imaging uncovers reactivity patterns on single nanocatalysts. *Nat Nanotechnol* **2012**, *7*, 237-241.

(29) Andoy, N. M.; Zhou, X. C.; Choudhary, E.; Shen, H.; Liu, G. K.; Chen, P. Single-Molecule Catalysis Mapping Quantifies Site-Specific Activity and Uncovers Radial Activity Gradient on Single 2D Nanocrystals. *J Am Chem Soc* **2013**, *135*, 1845-1852.

(30) Bueno, C.; Villegas, M. L.; Bertolotti, S. G.; Previtali, C. M.; Neumann, M. G.; Encinas, M. V. The excited-state interaction of resazurin and resorufin with amines in aqueous solutions. Photophysics and photochemical reaction. *Photochem Photobiol* **2002**, *76*, 385-390.

(31) Balcerzyk, A.; Baldacchino, G. Implementation of laser induced fluorescence in a pulse radiolysis experiment - a new way to analyze resazurin-like reduction mechanisms. *Analyst* **2014**, *139*, 1707-1712.

(32) Kresse, G.; Furthmuller, J. Efficient iterative schemes for ab initio total-energy calculations using a plane-wave basis set. *Phys Rev B* **1996**, *54*, 11169-11186.

(33) Dronskowski, R.; Blochl, P. E. Crystal Orbital Hamilton Populations (Cohp) - Energy-Resolved Visualization of Chemical Bonding in Solids Based on Density-Functional Calculations. *J Phys Chem-Us* **1993**, *97*, 8617-8624.

(34) Hoffmann, R. A Chemical and Theoretical Way to Look at Bonding on Surfaces. *Rev Mod Phys* **1988**, *60*, 601-628.

(35) Frisch, M. J.; Trucks, G. W.; Schlegel, H. B.; Scuseria, G. E.; Robb, M. A.; Cheeseman, J. R.; Scalmani, G.; Barone, V.; Mennucci, B.; Petersson, G. A.; Nakatsuji, H.; Caricato, M.; Li, X.; Hratchian, H. P.; Izmaylov, A. F.; Bloino, J.; Zheng, G.; Sonnenberg, J. L.; Hada, M.; Ehara, M.; Toyota, K.; Fukuda, R.; Hasegawa, J.; Ishida, M.; Nakajima, T.; Honda, Y.; Kitao, O.; Nakai, H.; Vreven, T.; Montgomery, J. A., Jr.; Peralta, J. E.; Ogliaro, F.; Bearpark, M.; Heyd, J. J.; Brothers, E.; Kudin, K. N.; Staroverov, V. N.; Kobayashi, R.; Normand, J.; Raghavachari, K.; Rendell, A.; Burant, J. C.; Iyengar, S. S.; Tomasi, J.; Cossi, M.; Rega, N.; Millam, J. M.; Klene, M.; Knox, J. E.; Cross, J. B.; Bakken, V.; Adamo, C.; Jaramillo, J.; Gomperts, R.; Stratmann, R. E.; Yazyev, O.; Austin, A. J.; Cammi, R.; Pomelli, C.; Ochterski, J. W.; Martin, R. L.; Morokuma, K.; Zakrzewski, V. G.; Voth, G. A.; Salvador, P.; Dannenberg, J. J.; Dapprich, S.; Daniels, A. D.; Farkas, O.; Foresman, J. B.; Ortiz, J. V.; Cioslowski, J.; Fox, D. J.: *Gaussian 09*, Revision D.01. Gaussian, Inc., Wallingford, CT, **2009**.

(36) Kim, F.; Connor, S.; Song, H.; Kuykendall, T.; Yang, P. D. Platonic gold nanocrystals. *Angew Chem Int Edit* **2004**, *43*, 3673-3677.

(37) Langille, M. R.; Personick, M. L.; Zhang, J.; Mirkin, C. A. Defining Rules for the Shape Evolution of Gold Nanoparticles. *J Am Chem Soc* **2012**, *134*, 14542-14554.

(38) Huang, J. F.; Zhu, Y. H.; Lin, M.; Wang, Q. X.; Zhao, L.; Yang, Y.; Yao, K. X.; Han, Y. Site-Specific. Growth of Au-Pd Alloy Horns on Au Nanorods: A Platform for Highly Sensitive Monitoring of Catalytic Reactions by Surface Enhancement Raman Spectroscopy. *J Am Chem Soc* **2013**, *135*, 8552-8561.

(39) Li, J. M.; Liu, J. Y.; Yang, Y.; Qin, D. Bifunctional Ag@Pd-Ag Nanocubes for Highly Sensitive Monitoring of Catalytic Reactions by Surface-Enhanced Raman Spectroscopy. *J Am Chem Soc* **2015**, *137*, 7039-7042.

(40) Zheng, Z. K.; Tachikawa, T.; Majima, T. Single-Particle Study of Pt-Modified Au Nanorods for Plasmon-Enhanced Hydrogen Generation in Visible to Near-Infrared Region. *J Am Chem Soc* **2014**, *136*, 6870-6873.

CHAPTER THREE

SUPPLEMENTARY INFORMATION

3.1 Introduction

This chapter contains experimental details and supplementary results of the bimetallic catalysis study in Chapter 2, which includes general instruments and experimental methods, materials synthesis, ensemble activity measurements, reaction mechanism discussions, data analysis of super-resolution catalysis imaging, additional imaging results, finite-difference time-domain (FDTD) simulations and DFT calculations.

3.2 General instruments and experiment methods

Resazurin used in the single-molecule catalysis imaging experiment was from Molecular Probes (99%, Cat no. R12204) with further purification by thin layer chromatography (TLC). Resazurin used in ensemble activity test was without TLC purification. Resorufin was from Sigma-Aldrich (95%; Cat no. 424455). All other chemicals were purchased from Sigma-Aldrich and used as received unless specified otherwise. All experiments were done at room temperature under ambient conditions unless specified otherwise. General instruments are listed here: UV-Vis spectra were measured on a Beckman Coulter DU800 spectrophotometer. Fluorescence spectra were measured on an Agilent Eclipse fluorometer. TEM (FEI Tecnai T12), high-resolution TEM (HRTEM, FEI Tecnai F20), SEM (LEO 1550) and related sample preparation were performed at the Cornell Center for Materials Research (CCMR) and the Cornell NanoScale Facility (CNF). The super-resolution reaction imaging experiment was carried out on a home-built prism-type wide-field total internal reflection fluorescence microscope. Image analyses were done using home-written MATLAB codes. FDTD simulations were performed using the Lumerical Solutions package. DFT calculations were performed using the Vienna Ab initio Simulation Package (VASP) and Gaussian 09 software.

All other instruments will be specifically described in the following sections.

3.3 Synthesis and characterizations of mesoporous-silica-coated PdAu nanoparticles

3.3.1 PdAu nanoparticles

PdAu nanoparticles were prepared via hydrothermal synthesis following Huang et al[1]. 17.7 mg $PdCl_2$, 300 mg NaI and 800 mg polyvinylpyrrolidone (PVP, MW = 55000) were dissolved in 18 mL nanopure water. Under stirring, the mixture was heated to 60 °C for 1 h in order to get a homogeneous solution and then transferred into a 100 mL Teflon-lined autoclave. The reactor was kept at 200 °C for 16 h to grow Pd nanorods (Figure 3.1A). Without purification, the resulting solution containing Pd nanorods (cooled down to room temperature) was directly used to make PdAu nanoparticles, in which the Au particle was grown at the ends of Pd nanorods. 6 mL of the as-synthesized Pd nanorod solution was mixed with 10 μL 0.15 M $HAuCl_4$ aqueous solution. The mixture was heated at 80 °C under vigorous stirring for 1 h to form PdAu bimetallic nanoparticles via galvanic replacement of Pd by Au. The final solution containing PdAu nanoparticles was mixed with isopropanol and centrifuged at 10,000 g for 10 min to remove the supernatant. The wash with isopropanol and precipitation were repeated once more for better purification. The precipitated PdAu nanoparticles were re-dispersed in 10 mL water for later silica shell coating. According to Huang et al[1], these Pd nanorods are likely 5-fold twinned structure with five {100} side surfaces along the ⟨110⟩ direction.

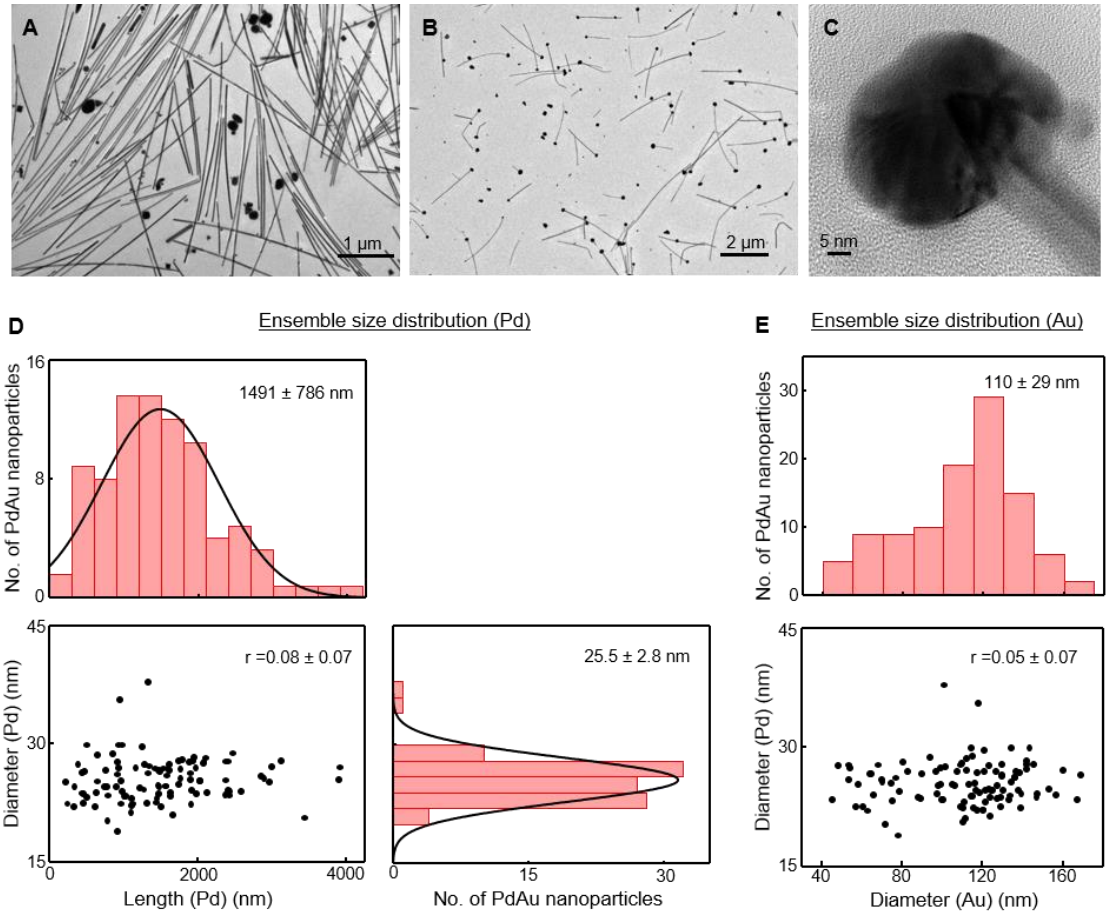

Figure 3.1 Structure characterizations of PdAu nanoparticles. (A-B) TEM images of Pd nanorods (A) and PdAu nanoparticles (B). (C) HRTEM image of an exemplary PdAu nanoparticle. It shows that the end of Pd nanorod was buried in the Au nanoparticle. (D) Size measurement of the Pd nanorod part of individual PdAu nanoparticles. Upper and right: distributions of the Pd nanorod length and diameter, respectively. Lower left: correlation between the diameter and length of 104 individual Pd nanorods. (E) Size measurement of the Au nanoparticle part of 104 individual PdAu nanoparticles: distribution of the Au nanoparticle diameter (upper) and the correlation plot of the Au nanoparticle diameter and Pd nanorod diameter (lower).

From the TEM image of PdAu nanoparticles (Figure 3.1B), the Au nanoparticles predominantly grow only on one end of the Pd nanorod, but occasionally could be on both ends. The length of the Pd nanorod part varied from several hundred nanometers to microns with an average of ~1500 nm, while the Pd nanorod diameter was mono-dispersed, ~25.5 ± 2.8 nm (Figure 3.1D). The Au nanoparticle diameter was about 110 ± 29 nm (Figure 3.1E, upper). There is no correlation between the length and the diameter of Pd nanorod (Figure 3.1D, lower left), or between the diameter of Au nanoparticle and that of Pd nanorod (Figure 3.1E, lower). HRTEM of the PdAu nanoparticles (Figure 3.1C) shows that the original end of the Pd was embedded in the Au nanoparticle, suggesting that the exposed bimetallic interface is on the side-facets of the Pd nanorods.

3.3.2 PdAu nanoparticles encapsulation by mesoporous silica shell

The PdAu nanoparticles were coated by a mesoporous silica shell using a procedure slightly modified from what we reported previously[2-4]. There were three steps involved: shell growth, shell etching, and sample activation:

(1) Shell growth: 100 μL 0.11 M 3-mercaptopropionic acid (MPA) in ethanol (instead of MPTMS in previous references[2-4]) was added to 10 mL PdAu nanoparticle aqueous solution under stirring for a 24 h ligand exchange. Then 100 μL 17 mM sodium silicate (Fisher Scientific) solution was added into the nanoparticle solution for an initial thin-layer-silica growth on PdAu nanoparticles. The resulting solution (pH adjusted to 9 by 2 M HCl) was stirred for 48 h and then centrifuged at 3,000 g to remove the supernatant. The precipitate was re-dispersed in a 10 mL 4:1 v/v ethanol/water mixture for further shell growth. 120 μL 10% (v/v) tetraethyl orthosilicate (TEOS) in ethanol and 100 μL 0.1 M NaOH solution were added into the mixture under vigorous stirring to grow a thicker silica shell. After 24 h growth, the solution was centrifuged at 3,000 g and the precipitate containing silica-coated PdAu nanoparticles (Figure 3.2A, C) was collected. The silica shell thickness was ~125 nm (Figure 3.2E, upper). The coated PdAu nanoparticles were re-dispersed in 12 mL 11:1 v/v water/ethanol mixture to etch the shell to be mesoporous.

(2) Shell etching: The above silica-coated PdAu nanoparticle solution was mixed with 60 μL 0.1 M cetyltrimethylammonium bromide (CTAB) and 60 μL 0.1 M NaOH solutions. The mixture was stirred for 30 min and then heated at 90 ℃ for 40

min to etch the silica shell. The resulting solution was cooled to room temperature and centrifuged at 3,000 g to collect mesoporous-silica-coated PdAu nanoparticles as precipitate. The final sample was washed by water and ethanol multiple times and dried in air. According to a previous study[4], the formed mesoporous silica shell has ordered wormhole-like pores. The average pore size is ~35 Å; and its specific surface area is ~1000 $m^2\ g^{-1}$.

(3) Sample activation: The organic compounds (i.e. PVP and CTAB) introduced in the earlier synthesis were removed via UV/ozone treatment, in which the dried sample was placed 2-3 cm away from a UV lamp (Ultraviolet, GPH357T5VH/4) and treated overnight. After UV/ozone treatment, the sample was re-dispersed in 1 mL water. An adequate amount (~10 μL) of 0.1 M $NaBH_4$ solution was added into the solution until the color was changed from brown to gray and kept for 5 min. (Note: too long an incubation in this solution would lead to a complete etching away of the shell, as $NaBH_4$ solution is basic.) The color change indicated that palladium oxide formed during the UV/ozone treatment was reduced to Pd[5]. Finally, the sample was washed by water (and then centrifuged down at 5,000 g to remove supernatant) multiple times to remove the unreacted $NaBH_4$. The final mesoporous silica shell thickness is ~114 nm (Figure 3.2E, lower), and the PdAu nanoparticle cores maintain their morphology (Figure 3.2B, D).

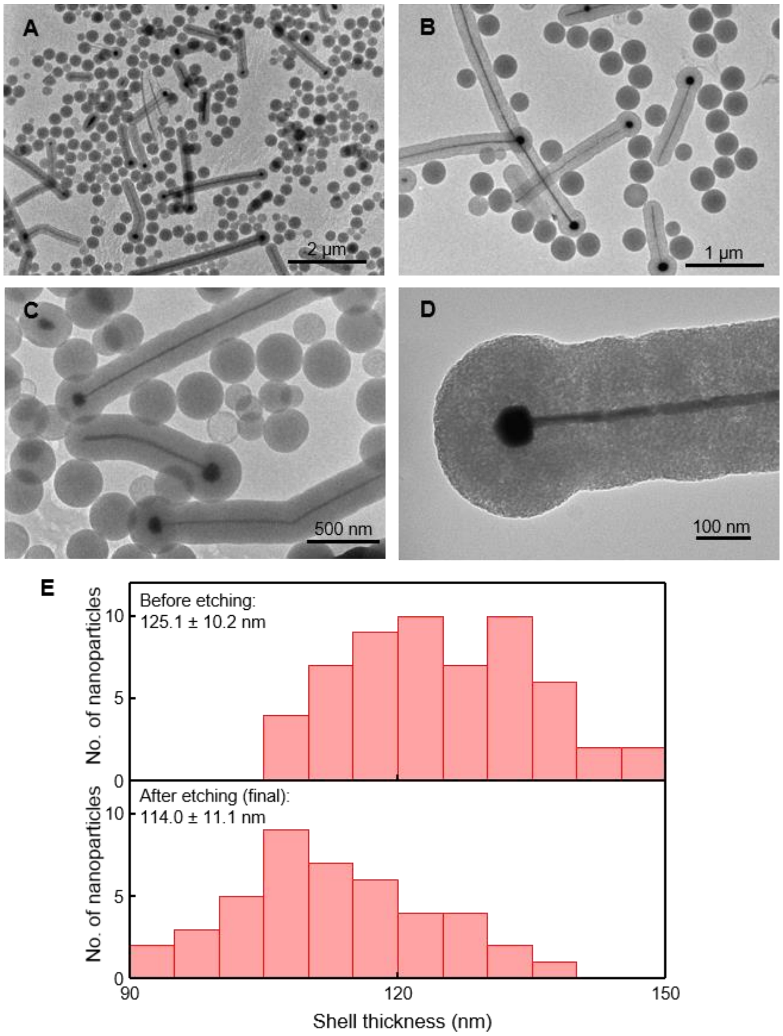

Figure 3.2 Structure characterizations of PdAu nanoparticles after silica shell coating and etching. TEM images of silica-coated PdAu nanoparticles (A, C) and mesoporous-silica-coated PdAu nanoparticles (after $NaBH_4$ treatment) (B, D). (E) Distributions of the silica-shell thickness before (top) and after (bottom) etching.

3.3.3 PdAu nanoparticles with a built-in nanoscale gap in mesoporous silica shell

The as-made mesoporous-silica-coated PdAu nanoparticles were heated at 450 ℃ for 1 h to break the Pd-Au junction (Figure 3.3A, B). After the heat treatment, the sample was also treated with $NaBH_4$ to reduce potential surface oxide layer. The gap size between Pd and Au varied broadly with the average of about 19 ±11 nm (Figure 3.3C-D), which is larger at longer heat treatment time (Figure 3.3E).

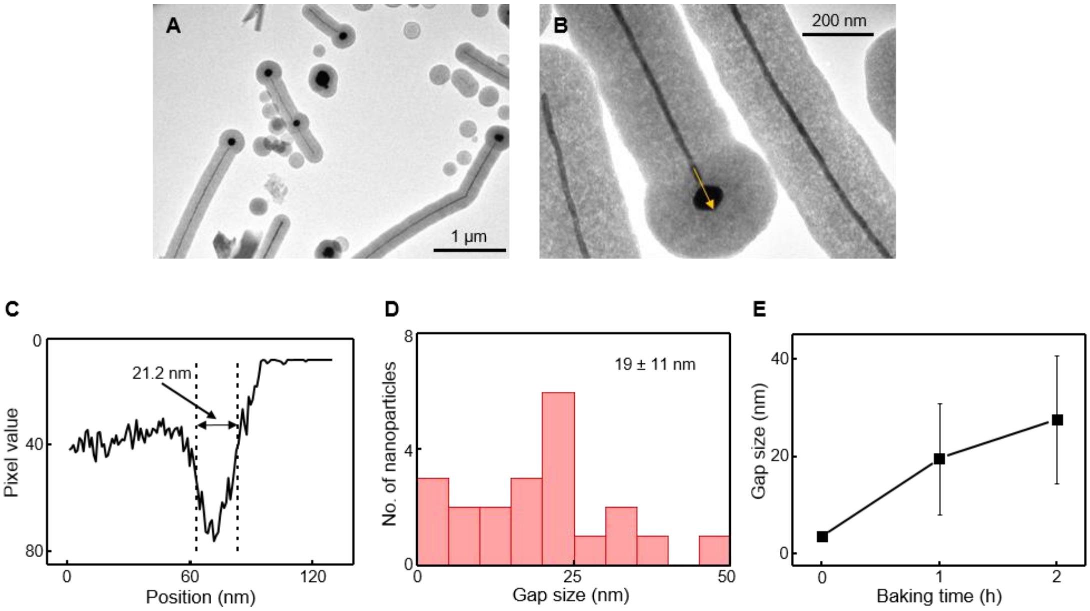

Figure 3.3 Structural characterizations of mesoporous-silica-coated PdAu nanoparticles after heat treatment to generate a gap. (A, B) TEM images of mesoporous-silica-coated PdAu nanoparticles with built-in nano-sized gaps. The arrow in B shows the direction of a line profile, which is presented in (C). (C) Line profile from B. The gap size is defined as the distance between the points at half-of-the-maximum for both sides. (D) Distribution of the gap size between Pd nanorod and Au particle after 1 h heat treatment. (E) Gap size versus heat treatment time. The error bar is s.d. The apparent gap size of ~3 nm at zero baking time indicates the uncertainty in measuring the gap size via line

profiling the TEM images. This uncertainty is much smaller than the average gap size of 19 ± 11 nm from D.

3.4 The study of photo-driven disproportionation reaction of resazurin to resorufin

3.4.1 Pd and Au can catalyze the photo-driven disproportionation reaction

The ensemble activity measurement of the photo-driven disproportionation reaction of resazurin to resorufin was performed by taking the time-dependent fluorescence spectra of the reaction solution. We sealed ~10 μL reaction solution containing resazurin, phosphate buffer and catalysts (homemade Pd nanorods or Au nanoparticles) in a 1.5 mm diameter borosilicate glass tube (Sutter Instrument) and the solution was illuminated by either 5 mW 532 nm (Coherent Sapphire) or 50 mW 488 nm (CrystaLaser) laser to drive the catalytic reaction. The detailed experiment conditions are in Figure 3.4 caption. Note: the as-synthesized Pd nanorods were capped by ligands and inactive for catalysis. We thus used the surfactant free Pd nanorods for ensemble activity measurement: we heat-treated mesoporous-silica-coated Pd nanorods (which were made by coating the Pd nanorods with the same procedure as described for PdAu nanoparticles) to remove surfactants and then dispersed them into 0.1 M $NaBH_4$ for an extended period of 3 h to reduce the palladium oxide formed in calcination as well as to dissolve the mesoporous silica shell (due to the strongly basic $NaBH_4$ solution), which exposed more Pd surfaces for catalysis. The Au nanoparticles were sub-10 nm sized, citrate-capped, prepared by the standard citrate-$NaBH_4$ reduction method[6].

The ensemble activity measurements show that: 1) Both Pd and Au can catalyze the reaction (Figure 3.4A, B). 2) Without the catalyst or the 532 nm light excitation, the reaction is significantly slower and almost negligible compared with that in the presence of both catalyst and light (Figure 3.4C, D). 3) The reaction could not be driven by 488 nm light (Figure 3.4C, D), which supports that it is the excited-state resazurin rather than the excited metal involved in the reaction because 488 nm cannot excite resazurin efficiently but can excite metal valence electrons (Figure 3.4E).

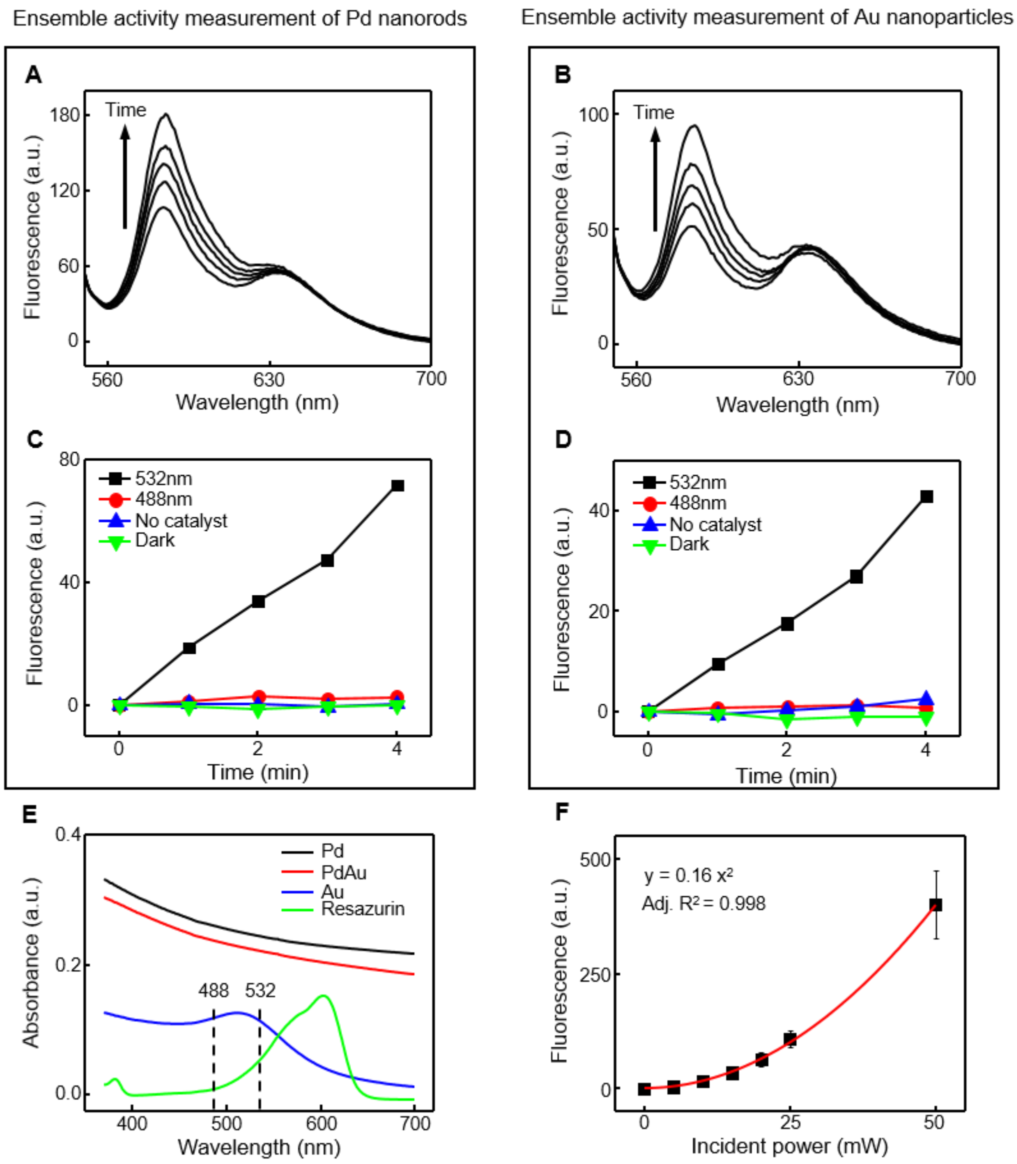

Figure 3.4 Ensemble catalytic activity measurement of Pd nanorods and Au nanoparticles. (A) Fluorescence spectra of the reaction solution containing 86.4 µM resazurin in 0.2 M pH 7.2 phosphate buffer in the presence of Pd nanorods under 5 mW 532 nm laser illumination. The fluorescence spectra were measured every 1 min and the increase of fluorescence at 583 nm indicates the formation of resorufin. (B) Same as A, but using Au nanoparticles as catalysts. (C) The time profile of fluorescence intensity

at 583 nm of the reaction solution under conditions including: 1) with catalyst (Pd nanorods) under 5 mW 532 nm illumination (black), 2) with catalyst under 50 mW 488 nm illumination (red), 3) without catalyst under 5 mW 532 nm illumination (blue) and 4) with catalyst but no illumination (green). (D) Same as C but using Au nanoparticles as catalysts. (E) Absorbance spectra of Pd nanorods (black), PdAu nanoparticles (red), Au nanoparticles (blue) and resazurin solution (green). All particles were measured without silica shell. (F) Power dependence of the uncatalyzed reaction activity (no catalyst added), which is reflected by the increase of fluorescence at 583 nm after 1 min reaction. The uncatalyzed reaction was measured in a more concentrated solution containing 0.78 mM resazurin in 0.2 M pH 6.6 phosphate buffer (lower pH here makes reaction faster and thus more easily measured). The error bar is the s.d. The excitation wavelength of all the fluorescence emission spectra is 532 nm.

3.4.2 Stoichiometry of the disproportionation reaction

The stoichiometry of the photo-driven disproportionation reaction of resazurin to resorufin was determined by quantitative analysis of the fluorescence spectra in the ensemble activity measurement. Here we used the above Pd-nanorod-catalyzed reaction (Figure 3.4A) to illustrate the stoichiometry measurement. The fluorescence spectra of pure resazurin (after TLC purification) and resorufin solution were shown in Figure 3.5A, which served as the standards to convert the fluorescence intensity into concentration. Note the fluorescence of the reactant resazurin is very weak, and needs to be measured at a much higher concentration. By monitoring the evolution of fluorescence at 583 nm and 634 nm along the reaction, we can get the relative concentration change of resazurin to resorufin (Figure 3.5B). It is worth noting that the fluorescence at 583 nm is from merely resorufin but at 634 nm is from the combination of resazurin and resorufin because of the spectral overlap. Therefore, for resazurin quantification (measured at 634 nm), we first removed the resorufin component (blue line in Figure 3.5B) and then calculated the concentration change. We measured the slope of the fluorescence intensity vs. time profile and converted that into resorufin generation or resazurin consumption rate. In the Pd-nanorod-catalyzed reaction, we calculated the stoichiometry of resazurin to resorufin is 3:1. In the same way, we also confirmed the stoichiometry of Au-nanoparticle-catalyzed reaction and the uncatalyzed reaction were 3:1 too.

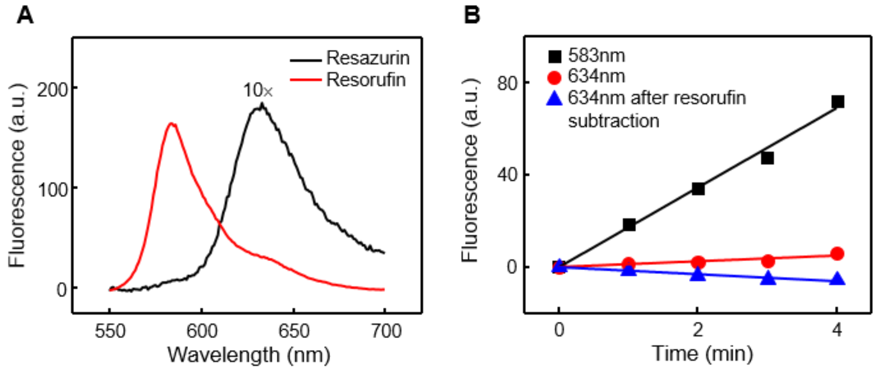

Figure 3.5 Stoichiometry determination of the photo-driven disproportionation reaction of resazurin to resorufin. (A) Fluorescence emission spectra of 1.03 µM resazurin (black, the curve is original data scaled by a factor of 10 to be clearly visualized) and 0.52 µM resorufin (red). (B) The fluorescence intensity versus time of the Pd-nanorod-catalyzed reaction solution at 583 nm (black), 634 nm (red), as well as 634 nm after

subtracting the contribution of resorufin (blue). The stoichiometry of resazurin to resorufin was calculated to be 3:1.

3.4.3 Proposed mechanism of the uncatalyzed reaction

Previous studies showed resazurin excited at 532 nm can disproportionate into a one-electron-reduced and a one-electron oxidized species[7], and the one-electron-reduced species can further disproportionate into resorufin and resazurin[8]. Combining these previous results with our experiment results, we proposed the following mechanism of the uncatalyzed photo-driven disproportionation reaction of resazurin (Rz^-) to resorufin (Rf^-):

$$2\mathrm{Rz}^{-*} \xrightarrow{k_1} \mathrm{Rz}^{\bullet} + \mathrm{Rz}^{2-\bullet} \tag{3.1}$$

$$2\mathrm{Rz}^{2-\bullet} + 2\mathrm{H_2O} \xrightarrow{k_2} \mathrm{Rz}^{-} + \mathrm{Rf}^{-} + 2\mathrm{OH}^{-} \tag{3.2}$$

$$\text{Overall: } 3\mathrm{Rz}^{-} + 2\mathrm{H_2O} \xrightarrow{hv} \mathrm{Rf}^{-} + 2\mathrm{Rz}^{\bullet} + 2\mathrm{OH}^{-} \tag{3.3}$$

k_1 and k_2 are rate constants of reactions (3.1) and (3.2), respectively.

In this mechanism, the excited resazurin (Rz^{-*}) can form a one-election-oxidized ($\mathrm{Rz}^{\bullet}$) and a one-election-reduced radical species ($\mathrm{Rz}^{2-\bullet}$) through self-quenching (3.1), which was reported by Encinas et al.[7] The one-election-reduced species ($\mathrm{Rz}^{2-\bullet}$) can further disproportionate to resazurin (Rz^-) and resorufin (Rf^-) (3.2), which was reported by Baldacchino et al.[8] The overall reaction (3.3) shows the stoichiometry of resazurin to resorufin should be 3:1, which is consistent with our experimental observation (Section 3.4.2).

Based on this proposed mechanism, the rate law of the overall reaction can be described. As the photoexcitation of resazurin and its decay to the ground state is at ultrafast time scale, much faster than the kinetics of the reactions, the photoexcited species Rz^{-*} can be assumed to be in equilibrium with the ground state Rz^{-} under a constant light illumination condition. Therefore, the excited state resazurin concentration $[Rz^{-*}]$ should be proportional to the ground state resazurin $[Rz^{-}]$ and the incident power density I_0:

$$[\mathrm{Rz}^{-*}] = K_{\mathrm{hv}} I_0 [\mathrm{Rz}^{-}] \tag{3.4}$$

where K_{hv} is a proportionality constant.

Considering reactions (3.1), (3.2), we applied the steady-state approximation to the one-election-reduced radical specials $[Rz^{2-\bullet}]$:

$$\frac{\mathrm{d}[\mathrm{Rz}^{2-\bullet}]}{\mathrm{d}t} = k_1[\mathrm{Rz}^{-*}]^2 - 2k_2[\mathrm{Rz}^{2-\bullet}]^2 = k_1(K_{\mathrm{hv}} I_0 [\mathrm{Rz}^{-}])^2 - 2k_2[\mathrm{Rz}^{2-\bullet}]^2 = 0 \tag{3.5}$$

Therefore

$$[\mathrm{Rz}^{\bullet 2-}] = \sqrt{\frac{k_1}{2k_2}} K_{\mathrm{hv}} I_0 [\mathrm{Rz}^{-}] \tag{3.6}$$

From Reaction (3.2), the resorufin $[Rf^{-}]$ formation rate is:

$$\frac{\mathrm{d}[\mathrm{Rf}^{-}]}{\mathrm{d}t} = k_2[\mathrm{Rz}^{\bullet 2-}]^2 = \frac{k_1}{2}(K_{\mathrm{hv}} I_0 [\mathrm{Rz}^{-}])^2 = k_{\mathrm{eff}} I_0{}^2 [\mathrm{Rz}^{-}]^2 \tag{3.7}$$

where $k_{\mathrm{eff}} = \frac{k_1 K_{\mathrm{hv}}^2}{2}$ is the effective rate constant.

This Equation (3.7) predicts a second-order power dependence of the uncatalyzed reaction rate, which was confirmed in the measurement of the power dependence of uncatalyzed reaction (Figure 3.4F). Note: since the uncatalyzed reaction is slow, we boosted the reaction by 1) increasing the resazurin concentration, 2) lowering pH of the solution, and 3) increasing the laser power. The results show that the reaction rate indeed has second-order power dependence.

It is worth noting that our results supports that the self-quenching (3.1) is between two excited resazurin molecules, while in the earlier study this step was written as one excited resazurin interacted with a ground state resazurin[7].

3.5 Super-resolution catalysis imaging

3.5.1 Experiment setup

The super-resolution catalysis imaging experiment setup was described in our previous studies[2,3,9] (Figure 3.6A). The experiment was performed on a home-built prism-type wide-field total-internal-reflection fluorescence (TIRF) microscope (Olympus, IX71). A 25 mW circularly polarized continuous wave 532 nm light (CrystaLaser, GCL-025-L-0.5%) was focused on an area of ~200 × 100 μm^2 in a home-made flow cell to excite the fluorescence of the catalytic product resorufin. The fluorescence was collected by a water-immersion 60X NA 1.2 objective (Olympus, UPLSAPO60XW), filtered by a 580 ± 30 nm band pass filter (Chroma, HQ580m60), and recorded by an EMCCD camera (ANDOR, iXon EM^+ DU-897 back illuminated) operating at 20 ms frame rate. For the single-particle emission spectrum measurement, we added a spectrograph (Princeton Instrument, Acton SP2150) in front of the EMCCD camera and took the spectrum of the product detected on a single catalyst particle to confirm the product is resorufin (Figure 3.6B).

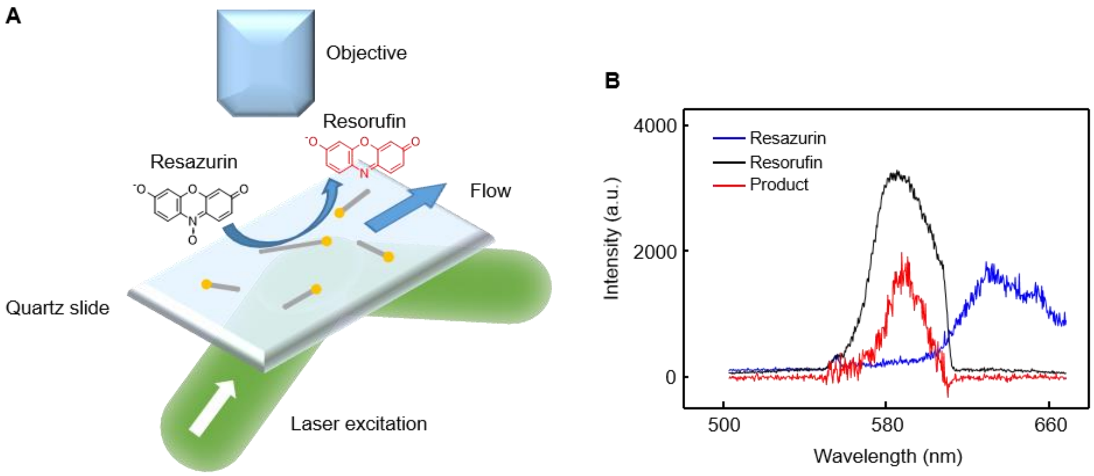

Figure 3.6 Super-resolution catalysis imaging on individual PdAu nanoparticles. (A) Schematic of experimental setup of the wide-field total-internal-reflection fluorescence (TIRF) microscope for super-resolution catalysis imaging. The prism on the back of the quartz slide and the coverslip on top of quartz slide were not shown. The configuration is depicted upside down here. (B) Single-particle fluorescence emission spectrum confirmed that the detected product was resorufin (red). The spectra of resazurin (blue) and resorufin (black) solutions were taken as references. The sharp vertical feature at 610 nm on the black spectrum was from the 580 ± 30 nm band pass cut off.

The flow cell was an assembly of a coverslip (Gold Seal) and a quartz slide (Technical Glass). Double-sided tape was used as the spacer in between to form a microfluidic channel, which was about 0.1 mm (height) × 5 cm (length) × 2 cm (width). Before assembly, a nanoparticle solution was drop-casted on the quartz slide and dried completely. During the experiment, the reactant (resazurin) solution was supplied into the channel with various concentrations (from 0 to 200 nM) at a continuous flow rate

(50 μL min^{-1}) by a syringe pump (Chemyx), to give a steady-state reaction condition.

3.5.2 Analysis procedures of super-resolution catalysis imaging results

3.5.2.1 Identification of single molecule events

The fluorescence images were analyzed by a home-written Matlab program, iqPALM (image-based quantitative photo-activated localization microscopy), which was reported in our previous studies[9,10]. There were some modifications of the original program for the current work and the details are listed below.

1) Each image was background subtracted (the average of the last 100 frames before each image was used as the background; note that the contribution of single-molecule signals to the background is negligible because typically in 100 frames there were typically less than 3 frames containing single-molecule fluorescence signals on a particle, and thus after averaging, their signals were completely washed out in the noise) to remove the constantly bright objects such as gold nanoparticle position makers, and the pixels with local maximum intensity larger than a threshold (typically mean plus 6 standard deviations of pixel counts in the image frame of 400 × 200 pixel^2, about 100 × 50 μm^2) were identified as the potential single molecule fluorescence signals. The threshold was intentionally set low to pick much more candidates (about 50) than the real events (less than 5) in each image frame and the later filtering process will clean up those false detections.

2) For each picked pixel (i.e., local maximum), a 13 × 13 pixel^2 area (centered

at that pixel) in the original image (without background subtraction) was taken out; from it we subtracted the same area of image from the average of the last five frames, which served as the background (if there was a local maximum found in these five frames, we used even earlier frames). By using the average of just 5 frames, we minimize the error in the background subtraction from stage drifting. Then the area was fitted with a 2-dimensional Gaussian function to get the centroid position (x, y). The fitting also generated the width parameters σ_x, σ_y (the standard deviations of the 2-D Gaussian function), integrated intensity (i.e., brightness) V of the Gaussian function as well as the localization errors Er_x, Er_y of the centroid position. The fitting details could be found in our earlier studies[2,10]. The drift correction was applied every frame based on the positions of 100 nm gold particle position markers (Ted Pella, Cat no. 82160-100), which are tannic acid-capped and inactive in catalysis. The positions of the makers were generated by fitting their emission signals with 2-D Gaussian functions.

3) To clean up the false detections in the above analysis procedures, we filtered the fitted events by their σ_x, σ_y, Er_x, Er_y. The ideal fluorescence signal of a single resorufin molecule should appear with the diffraction-limited FWHM $0.61 \times \lambda/\text{NA} = 0.61 \times 583 \text{ nm} / 1.2 = 297$ nm, which is about 126 nm in σ_x, σ_y. for a 2-D Gaussian function. The actual σ_x, σ_y of detected signal are peaked at ~197 nm (Figure 3.7A, B); this broadening is commonly seen, likely due to imperfect focusing of the detection system, noise contribution to the image, and that molecules are not exactly in the focal plane. Therefore we chose the events with σ_x, σ_y larger than 120 nm, and we also removed the events with σ_x, σ_y larger than 400 nm, which were too broad and negligible in population. We also applied the localization error filter to remove those events with

Er_x, Er_y larger than 50 nm, which were bad fits and also small in population (Figure 3.7C, D). The summaries of the fitting parameters of σ_x, σ_y, Er_x, Er_y and integrated intensity V of the final catalytic events on PdAu nanoparticles are shown in Figure 3.7.

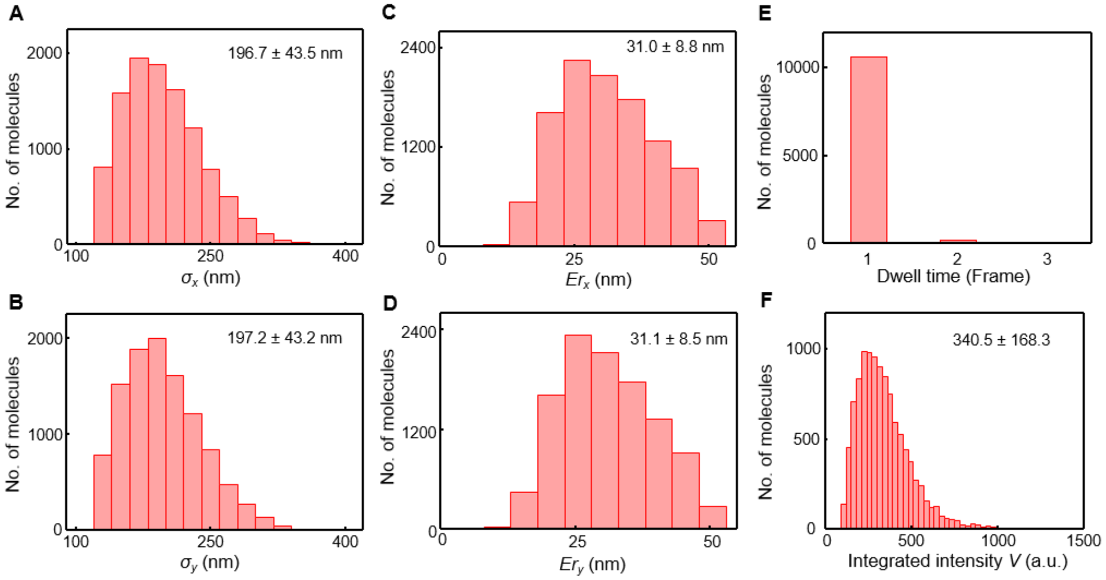

Figure 3.7 Obtained parameters of the detected product molecules. Distributions of σ_x (A), σ_y (B), Er_x (C), Er_y (D), dwell time (E), and integrated intensity of the 2D-Gaussian function V (in EMCCD camera counts) (F) of the detected molecules. The data contains 10853 events detected on 12 PdAu nanoparticles.

Justification of no over-counting for multi-frame events. Based on the iqPALM algorithm, if a fluorescence event lasts for several frames, it generates one fit per frame and therefore there might be an over-counting issue. To correct for it, we regarded the events in consecutive frames as the same molecule if they appeared within 50 nm in distance, which is approximately the mean plus 2 standard deviations of Er_x, Er_y. After event combining, we checked the dwell time of the detected single molecule events.

Majority (98.1%) of the detected events only lasted for 1 frame (Figure 3.7E). It means the over-counting issue is negligible (<2%), but we corrected for it anyway. The short dwell time also means there is no significant lateral diffusion of the product molecule within the mesoporous silica shell before it desorbs and disappears into surrounding solution.

3.5.2.2 Corrections of detection efficiency

Correction of differences in reactant concentration. With the increase of resazurin concentration, the fluctuation of fluorescence background (noise) also increases, and the detection of weaker signals would be harder and the detection efficiency of the fluorescent product molecules could decrease. To correct for that, we used the movie taken at the lowest resazurin concentration (10 nM) as the reference to evaluate the decrease of detection efficiency at higher concentrations. The procedure is as follows (we used the correction for the movie taken at 20 nM resazurin as an example):

(1) Get brightness (mean) and noise (standard deviation) of each pixel from its time-based trajectory in the reference movie (10 nM) and the evaluation movie (20 nM). For pixel *i* in the reference movie, its pixel counts follow approximately a Gaussian distribution, $N(\mu_{i1},\sigma_{i1}^2)$ and in the evaluation movie it should follow another Gaussian distribution, $N(\mu_{i2},\sigma_{i2}^2)$, where μ is the mean value and σ is the standard deviation of the Gaussian distribution.

(2) Generate a simulated movie of 20 nM by adding noises to the reference movie. Every pixel *i* in the reference movie was adjusted by adding a Gaussian noise, $N(\mu_{i2} - \mu_{i1}, \sigma_{i2}^2 - \sigma_{i1}^2)$, so it followed the same distribution as that in the actual evaluation movie (20 nM) after adjustment. This means in the simulated movie, the brightness and noise of each pixel is close to that in the actual evaluation movie.

(3) Analyze the simulated movie and calculate the recovery ratio, which is defined as the number of events identified in the simulated movie normalized by that in the reference movie. The recovery ratio is used to correct for the detection efficiency decrease

Correction for differences in laser power. With the decrease of the incident laser power density, the signal-to-noise ratio of fluorescence events gets smaller so the detection efficiency also decreases. The difference between correcting for reactant concentration and correcting for laser power is: in the former case it is the increased noise leading to the decrease of detection efficiency, while in the latter, it is the decreased signal resulting in the decrease of detection efficiency. Therefore we have to use a different approach to evaluate the detection loss caused by the incident power decrease. To keep consistent with the correction for reactant concentration, we used the same reference movie (10 nM resazurin, 21.7 mW incident power) to evaluate relative detection loss at lower incident powers. The procedure is as follows (we used the correction for the movie taken at 16.9 mW incident light as an example):

1) We examined the fitting results of the single molecule events (Figure 3.7) and recorded the distributions of fitting parameters as well as the noise at different power densities, which will be used to construct the simulated movie.

(2) Generate a simulated movie of 16.9 mW starting by constructing a series of fluorescent signals (2D Gaussian functions) on a flat surface with no noise. The brightness (V) and width (σ_x, σ_y) of the generated signals sampled their measured distributions from the actual movie (16.9 mW). Then add Gaussian noises to each pixel so that the noise in the simulated movie was close to that in the real movie.

(3) Analyze the simulated movie and calculate the recovery ratio, which is defined as the number of events identified in the artificial movie divided by the input number of single-molecule fluorescent signals. Finally the recovery ratios at different power densities were normalized by that in the reference movie (21.7 mW).

By evaluating the detection efficiency within the experimental reactant concentration and incident power range, we find: 1) With the increase of the reactant concentration, the detection efficiency dropped significantly (Figure 3.8A). At the highest substrate concentration (200 nM) the relative detection efficiency went down to 20% of that at 10 nM. 2) Within the experiment incident laser power range, the detection efficiency has very little change (Figure 3.8B). Therefore, we only applied the correction for the reactant concentration to the activity measurement (Figure 3.8C).

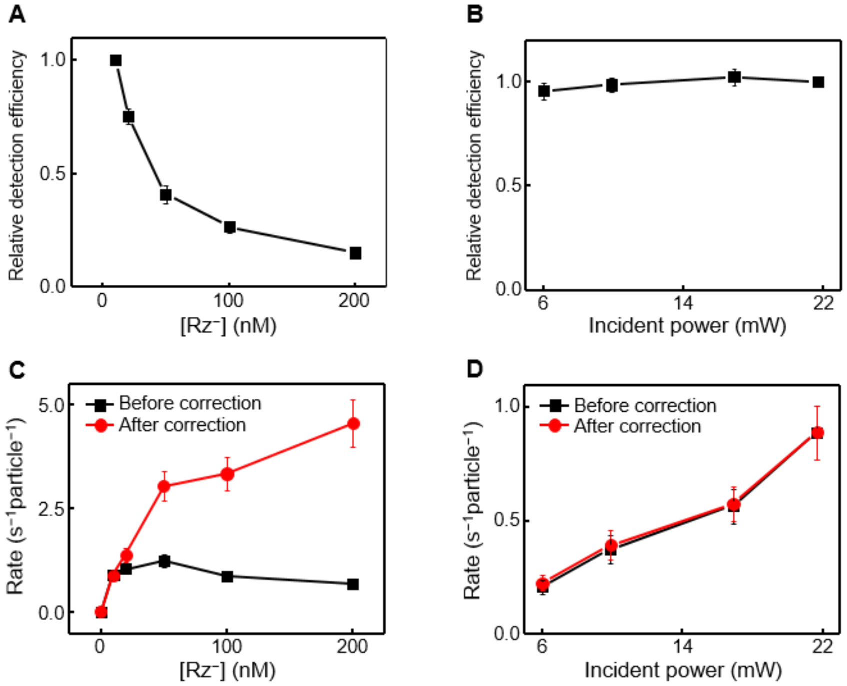

Figure 3.8 Correcting for the effect of reactant concentration and incident laser power dependences in affecting the detection efficiency. (A, B) The relative detection efficiency versus reactant concentration and incident power, respectively. (C) The concentration dependence of single PdAu nanoparticle turnover rates before (black) and after (red) correcting for the reactant-concentration dependent detection efficiency. (D) Same as C, but for correcting the laser incident power dependence; no significant difference here before and after the correction. The error bars are s.e.m.

3.5.2.3 Overlay of the super-resolution catalysis image onto the corresponding SEM image of PdAu nanoparticles

After we get the locations of the detected catalytic product formation events, we reconstructed the super-resolution (SR) image (i.e., 2-D histogram of product locations) of single particle catalytic activity. The SR image and SEM image were overlaid individually for every analyzed PdAu nanoparticle by the following procedures (Figure 3.9A). First, the SR and corresponding SEM images were both converted into binary images by thresholding (mean plus 2 standard deviations of all pixel values) to get the mass centers (of the binary images) and contours; the isolated hot pixels were removed from the binary image. We used this binary image, instead of the original SR image, to obtain the mass center because the mass center of the SR image could be affected by the activity heterogeneity at different locations within a single particle. Second, the contour from SR binary image was overlaid on top of that from SEM binary image with their mass centers overlapped. Third, the contour from SR image was rotated to maximize the overlap with the contour from SEM image. Note: In the subsequent spatial activity analysis, we only considered events within the SEM contour (with a 50 nm out-of-contour tolerance due to the spatial resolution of our catalysis imaging, ~40 nm).

The error of overlay. It is worth noting that each single particle overlay essentially establishes a transformation relation from the SR image to SEM image, which contains both translational and rotational moves. In the above overlaying process, the overall error has three components: 1) error in center determination in SEM image, 2) error in center determination in SR image and 3) error in rotation of SR image. The first term is related to the spatial resolution of SEM image (less than 5 nm), which is negligible compared to the spatial resolution of catalysis imaging (~30-40 nm) thus we assumed the center position in SEM is perfectly determined. The second term, defined as Δr, is actually the error in translational move (because the overlay of mass centers was done by translation), which is about the spatial resolution of SR image (~30-40 nm, detailed evaluation shown in Figure 3.9B, C). The third term, defined as $\Delta\alpha$, is estimated ~1-2 degree (Figure 3.9B, C). Therefore the overall error is estimated ~40 nm within an area less than 2×2 μm^2; this area is larger than most of our particle sizes.

We evaluated Δr and $\Delta\alpha$ by the following procedures. We set the center of the overlaid particle as the reference point and used its transformation relation to check the overlay precision of the nearby particles (Figure 3.9B). For a nearby particle, the distance between its centers in the SR image and the SEM image, ΔD, is related to its distance from the reference point, r, through the equation $(\Delta D)^2 = (r\Delta\alpha)^2 + (\Delta r)^2 = r^2(\Delta\alpha)^2 + (\Delta r)^2$, where Δr and $\Delta\alpha$ are the radial (translation) and angular (rotation) errors (Figure 3.9B), which are orthogonal to each other. By linear fitting of $(\Delta D)^2$ vs. r^2 (Figure 3.9C), we can calculate Δr from the intercept Δr^2 and $\Delta\alpha$ from the slope $\Delta\alpha^2$. From the fitting results of 72 pairs of particles, we estimated Δr ~39 nm and $\Delta\alpha$ ~1.9 degree.

The high contrast of Au nanoparticle core in SEM image enables the direct size measurement. We measured the Au nanoparticle core size from SEM image and compared it to the result from TEM image (Figure 3.9D). The difference is about 10%, possibly due to that the small Au particles are not easily visible in SEM image. It is worth noting that the small difference of size measurement between SEM and TEM images would not affect the measured bimetallic activity enhancement because we only compared two Au hemispheres within the same particle, which share the same Au particle size.

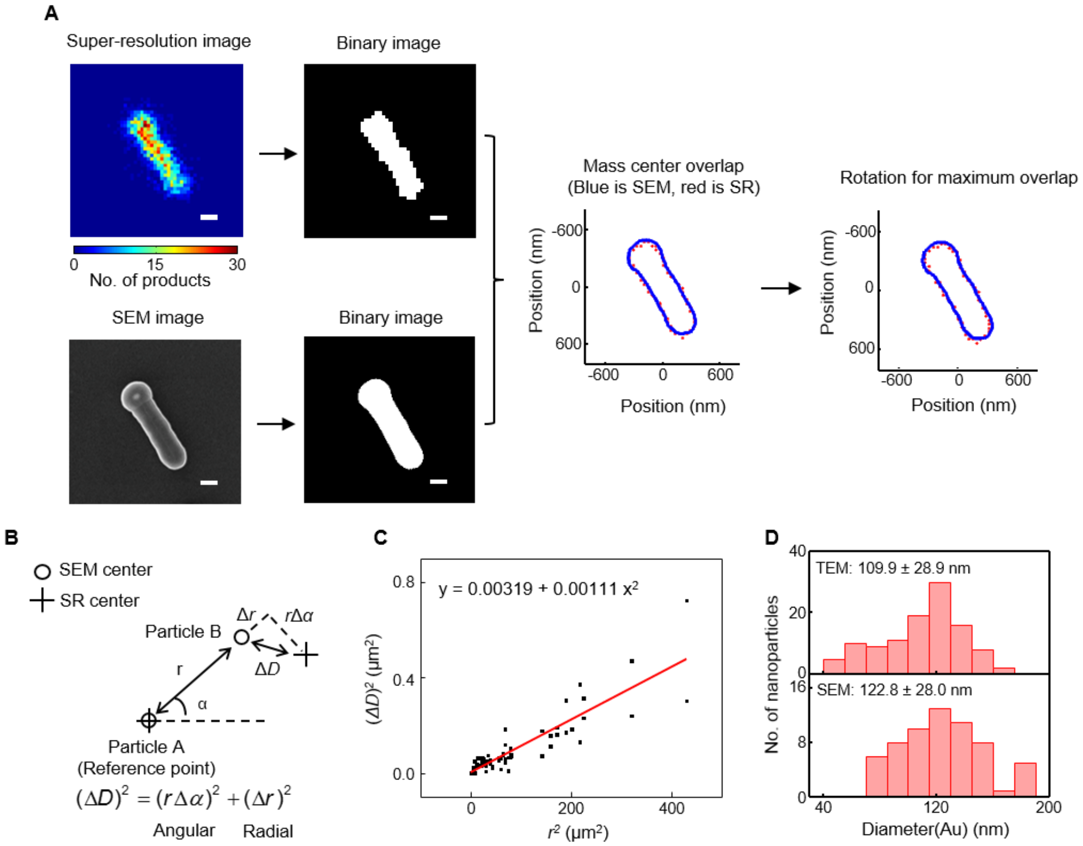

Figure 3.9 Overlay of the super-resolution (SR) catalysis image onto the SEM image of a PdAu nanoparticle. (A) Scheme of the overlay procedure. The SR and SEM images were converted into binary images to get their mass centers and contours. The mass centers were overlaid and then the SR image was rotated to achieve the maximum overlap of the contours in SR and SEM images. Since the original SR and SEM images were manually adjusted to have almost same orientations before overlay process, the rotation only did very small change (1.6 degree anticlockwise in this example shown). (B) The illustration of the overlay error. Particle A was set as the reference point to overlay the SR image onto SEM images. For a nearby particle B, the distance between its center in SR and SEM image (ΔD) is related to its distance from the particle A (r) as

well as the radial (translation) error Δr and angular (rotation) error $\Delta \alpha$ of the overlay process. (C) $(\Delta D)^2$ versus r^2 for 72 pairs of particles to determine the overlay error. From the linear fitting, Δr (calculated from intercept) is 39 nm and $\Delta \alpha$ (calculated from slope) is 1.9 degree. (D) Size measurement of Au nanoparticle in PdAu nanoparticles from TEM image (upper) and SEM image (lower). The scale bars in the images represent 200 nm.

3.5.2.4 Additional examples of super-resolution imaging of activity enhancement at bimetallic regions

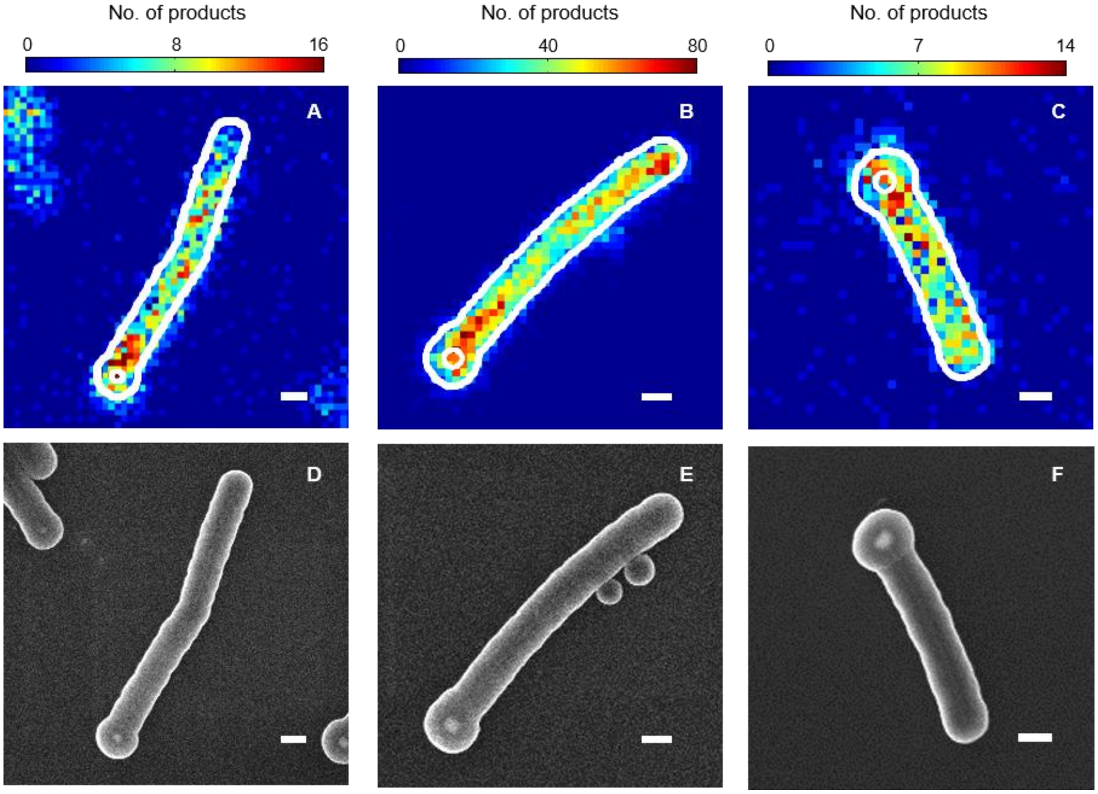

Figure 3.10 Additional examples of super-resolution catalysis imaging of catalytic activity enhancement near the Pd-Au bimetallic interface. (A-C) 2-D histogram of catalytic product positions on three PdAu bimetallic nanoparticles. (D-F) SEM images of the particles in A-C. All scale bars represent 200 nm.

3.5.2.5 Segmentation of the PdAu nanoparticles and surface area calculations

After we overlaid the super-resolution catalysis image onto the SEM image, we dissected the nanoparticle and the associated product positions into segmented regions for spatially resolved analysis. The segmentation is illustrated in Figure 3.11A. From the SEM image, we can locate the Pd-Au interface by using the center position and the diameter of Au nanoparticle. We defined the Pd segment (100 nm in length) next to the Pd-Au interface as the bimetallic Pd region (denoted as $\mathrm{Pd_{Au}}$). For parallel comparison, the rest of the Pd nanorod was also dissected into 100 nm-long segments from the other free end (and the last segment is less than 100 nm because the rod length is not integer multiplication of 100 nm). All Pd segments except the free-end segment ($\mathrm{Pd_{end}}$) and last two segments close to the interface (which covers the bimetallic Pd region, $\mathrm{Pd_{Au}}$) were combined to be the monometallic Pd region (denoted as Pd). For Au nanoparticle, the hemisphere next to the Pd-Au interface was defined as the bimetallic Au region ($\mathrm{Au_{Pd}}$) and the other hemisphere away from the bimetallic interface was defined as the monometallic Au region (Au).

In the gapped-PdAu nanoparticles, we also divided the Au nanoparticle into two hemispheres for comparison. The one proximal to the Pd nanorod was denoted as $\mathrm{Au_p}$ and the other hemisphere distant from the nanorod was labeled as $\mathrm{Au_d}$.

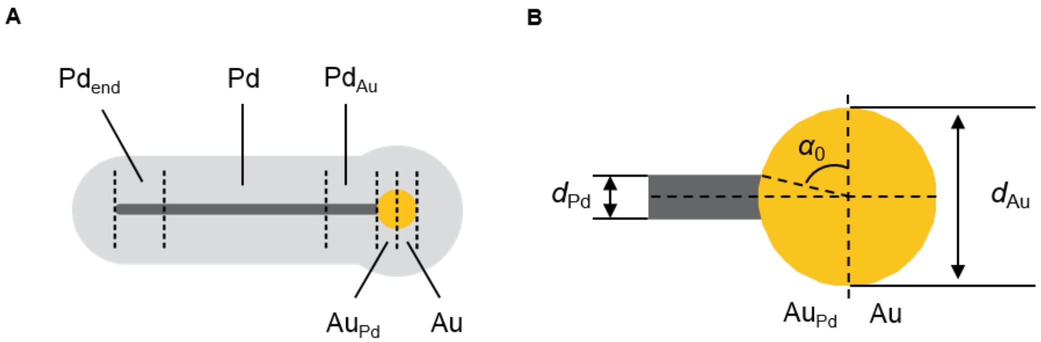

$$S(\mathrm{Au_{Pd}}) = \int_0^{\alpha_0} [2\pi(\frac{d_{\mathrm{Au}}}{2})\cos\alpha](\frac{d_{\mathrm{Au}}}{2})\mathrm{d}\alpha = \frac{1}{2}\pi d_{\mathrm{Au}}{}^2 \sin\alpha_0$$

$$= \frac{1}{2}\pi d_{\mathrm{Au}}{}^2 \sqrt{1-(\frac{d_{\mathrm{Pd}}}{d_{\mathrm{Au}}})^2} \qquad (\cos\alpha_0 = \frac{d_{\mathrm{Pd}}}{d_{\mathrm{Au}}})$$

Figure 3.11 Segmentation of PdAu nanoparticles. (A) The model PdAu nanoparticle with the definitions of bimetallic regions ($\mathrm{Pd_{Au}}$, $\mathrm{Au_{Pd}}$), monometallic regions (Pd, Au) and the Pd end segment (Pd_{end}). (B) The surface area calculation of the bimetallic region Au_{Pd}, considering that its contact with the Pd nanorod is buried.

In order to evaluate the local specific turnover rates, we calculated the surface area of all regions (Table 3.1). Specifically, for the surface area of the bimetallic Au region (Au_{Pd}), we did not count the part of the Au hemisphere blocked by the contact with the Pd nanorod (Figure 3.11B), even though it is only a very small fraction — the difference between the Pd nanorod and Au particle diameters (for $d_{Pd} = 25$ nm and $d_{Au} = 110$ nm) is large and the blocked part is less than 3% of the hemisphere surface area.

Table 3.1 Surface area calculation of PdAu nanoparticles [a]

Regions	Pd_{Au}, Pd, Pd_{end}	Au_{Pd}	Au, Au_p [b], Au_d [c]
Surface area	$\pi d_{Pd} L$	$\frac{1}{2}\pi d_{Au}^2 \sqrt{1-(\frac{d_{Pd}}{d_{Au}})^2}$	$\frac{1}{2}\pi d_{Au}^2$

[a] For bimetallic Pd region (Pd_{Au}) and monometallic Pd region (Pd), L is the segment length (100 nm). For the Pd end segment (Pd_{end}), L is the length of the end segment (100 nm), starting from the end of the Pd nanorod toward the rod body. [b, c] Au_p and Au_d refer to the Au hemispheres proximal to and distant away from the Pd nanorod in the gapped PdAu nanoparticles, respectively.

3.5.3 Control experiments

(1) The catalytic activity of PdAu nanoparticles are stable over 6 hours. We monitored the catalytic activity of the PdAu nanoparticles in the imaging experiment at

$[\mathrm{Rz}^{-}]$ = 50 nM over 6 h and there is no obvious deactivation of the catalytic performance (Figure 3.12A).

(2) Isolated monometallic Pd nanorods and Au nanoparticles show similar activities to the monometallic Pd region and the monometallic Au region in the bimetallic PdAu nanoparticles, respectively. In our bimetallic PdAu nanoparticle sample, there are also pure Pd nanorods and Au nanoparticles present as minor components, which were imaged together with the bimetallic PdAu nanoparticles. The properties (rate constant and reactant adsorption equilibrium constant) of the pure monometallic particles are comparable to the corresponding monometallic regions of the PdAu nanoparticles; this comparableness served as an extra control to show the increased activity of the bimetallic regions (Figure 3.12B, C).

(3) The fluorescence intensity of the product resorufin is homogeneous across different regions within single PdAu nanoparticles. We compared the fluorescence intensities of individual fluorescent product resorufin per image detected at different regions; there is no discernable difference among them (Figure 3.12D). This confirms that there is no detection bias between the bimetallic regions and monometallic regions.

(4) Reactant accesses to the bimetallic and monometallic regions are equivalent. To ensure that the observed catalytic activity differences at the bimetallic vs. monometallic regions are not due to differences in mesoporous silica shell structure (such as pore size) which could result in different access of the reactant to the metal surface, we flowed in the product resorufin solution and measured the binding frequency of the product molecules at different regions, using resorufin as a structural mimic to the reactant resazurin. For both Pd and Au, there is no appreciable difference in the

observed binding frequency of resorufin between bimetallic regions and monometallic regions (Figure 3.12E), supporting there is no structural difference of the mesoporous silica shell and thus the accessibility of metal surfaces of different regions should be the same. Note we normalized the resorufin binding frequency by the corresponding mesoporous silica shell volume. The conclusion would not change if we normalize it by the corresponding metal surface area of different regions, because for the same length of Pd_{Au} and Pd segments (or Au_{Pd} and Au), they correspond to the same mesoporous silica shell volume as well as metal surface area (thus either way of normalization would give the same conclusion).

(5) <u>The dwell time of the product within the mesoporous silica shell is equivalent between the bimetallic and monometallic regions.</u> The dwell times of resorufin on the nanoparticles, which are due to adsorption to the sites within the mesopores of the silica shell, in the bimetallic regions and monometallic regions, are about the same (~20 ms, or 1 frame, Figure 3.12F). This comparable dwell time indicates that the trapping efficiency of the product by the mesoporous silica shell at different regions are approximately the same.

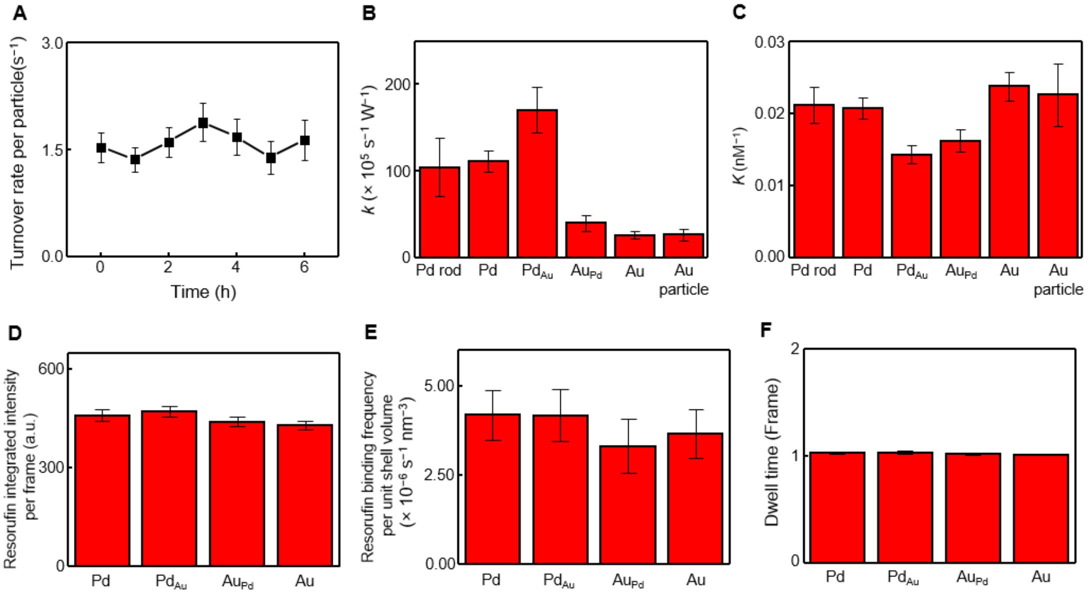

Figure 3.12 Control experiments of the super-resolution catalysis imaging of PdAu nanoparticles. (A) Temporal stability of the PdAu nanoparticle catalytic activity. The reaction condition is [Rz⁻] = 50 nM in 30 mM pH 7.2 phosphate buffer under 21.7 mW 532 nm laser excitation. Data averaged over 25 nanoparticles. (B, C) Rate constant *k* (B) and adsorption equilibrium constant *K* (C) of the bimetallic (Pd_{Au}, Au_{Pd}) and monometallic regions (Pd, Au) of the bimetallic PdAu nanoparticles in comparison with those of isolated monometallic Pd nanorods (Pd rod) and Au nanoparticles (Au particle) present in the sample (data averaged over 53 PdAu nanoparticles, 12 Pd nanorods, and 10 Au nanoparticles, respectively). (D) The integrated intensity per frame (in EMCCD counts) of the detected individual resorufin molecules at different regions (each region is an average from 20 PdAu nanoparticles). (E) The resorufin binding frequency per unit volume of the mesoporous silica shell at different regions (each region is the average result from 15 PdAu nanoparticles). The experiment was carried out under the condition [Rf⁻] = 190 pM in 20 mM pH 7.2 buffer under 21.7 mW 532 nm laser

excitation. (F) Dwell time of the detected individual resorufin molecules at different regions. Each bar is an average of ~1000 events. All error bars are s.e.m.

3.5.4 Proposed kinetic mechanism of the catalytic reaction

Based on the reactant concentration and light power dependence of the single-particle catalytic activity shown in Figure 2.2F, we propose a kinetic model of the catalytic photo-driven disproportionation reaction of resazurin to resorufin. The resazurin concentration dependence follows a typical Langmuir adsorption isotherm, indicating the reaction occurs to catalyst-surface adsorbed resazurin. The linear light power dependence indicates the rate-limiting step should involve a photo-excited resazurin (in Section 2.2.1, we have presented results that support the photo-driven part comes from exciting resazurin rather than the photo-excited metal). Therefore, the conversion from resazurin to resorufin in our model is that a metal-surface-adsorbed excited-state resazurin $[\mathrm{M}^{n}\text{–}\mathrm{Rz}^{-*}]$ gets two electrons to be reduced to resorufin (reaction (3.8); n reflects the number of electrons on the metal).

$$\mathrm{M}^{n}\text{–}\mathrm{Rz}^{-*}+\mathrm{H_2O}\longrightarrow \mathrm{M}^{n-2}\text{–}\mathrm{Rf}^{-}+2\mathrm{OH}^{-} \tag{3.8}$$

This two-electron reduction could be two consecutive one-electron reductions with the 1st one being rate-limiting, but could also be simultaneous 2-electron reduction. We cannot differentiate these two possibilities at the moment, but we favor the former one considering the energetics of orbitals involved (Figure 3.13A, right). Energetically, the singly-occupied HOMO of the excited-state resazurin can readily accept one, and only one, electron from the Fermi level of metal. The second electron transfer must occur after structural and electronic changes on the consequent 1-electron-reduced resazurin.

Based on this model, the specific turnover rate v (s^{-1} μm^{-2}) should be proportional to the concentration of adsorbed excited-state resazurin (as well as water, which could be from the bulk solution or adsorbed on the surface and which is a constant due to its large excess and can thus be part of the proportionality factor):

$$v \propto [\mathrm{M}^{\mathrm{n}}\text{–}\mathrm{Rz}^{-*}] \tag{3.9}$$

v should be further proportional to the incident power density I (in units of kW cm^{-2}) and the adsorbed ground-state resazurin $[\mathrm{M}^{\mathrm{n}}\text{–}\mathrm{Rz}^{-}]$ since $[\mathrm{M}^{\mathrm{n}}\text{–}\mathrm{Rz}^{-*}] \propto I[\mathrm{M}^{\mathrm{n}}\text{–}\mathrm{Rz}^{-}]$:

$$v \propto I[\mathrm{M}^{\mathrm{n}}\text{–}\mathrm{Rz}^{-}] \tag{3.10}$$

The adsorbed resazurin $[\mathrm{M}^{\mathrm{n}}\text{–}\mathrm{Rz}^{-}]$ should follow the Langmuir isotherm adsorption model, which is

$$[\mathrm{M}^{\mathrm{n}}\text{–}\mathrm{Rz}^{-}] = \frac{n_{\mathrm{T}}K[\mathrm{Rz}^{-}]}{1+K[\mathrm{Rz}^{-}]} \tag{3.11}$$

where K (nM^{-1}) is the adsorption equilibrium constant of resazurin on the metal surface, and n_{T} is concentration of the total number of available surface sites. Therefore putting everything together we could the rate expression:

$$v = k'I\frac{n_{\mathrm{T}}K[\mathrm{Rz}]}{1+K[\mathrm{Rz}]} = I\frac{kK[\mathrm{Rz}]}{1+K[\mathrm{Rz}]} \tag{3.12}$$

where k' is a proportionality constant, and $k = k'n_{\mathrm{T}}$ (in the units of s^{-1} W^{-1}) is effectively a rate constant that quantifies the catalytic reactivity of the metal. The unit of k does not contain μm^{-2} because the surface area normalization was included in the power density term I (in units of kW cm^{-2}). Equation (3.12) predicts the linear light power density dependence and saturation behavior vs. resazurin concentration of catalytic activity, consistent with the experiment observations.

Reaction (3.8) is the reduction half reaction of the overall disproportionation reaction. For the oxidation half reaction, which was not monitored directly in our experiments, a number of experimental observations hint on the underlying mechanism. First, since the stoichiometry of resazurin to resorufin in the reduction half is 1:1 while the overall stoichiometry of resazurin to resorufin was determined to be 3:1 (Section 3.4.2), the oxidation half should consume two resazurin molecules. Considering the reduction from resazurin to resorufin is an overall two-electron reduction reaction, the oxidation part should be two single-electron oxidations from two resazurin molecules in order to meet both stoichiometry and charge balance requirement. Second, from the energy level diagram (Figure 3.13A, left), the singly-occupied LUMO of the excited-state resazurin is energetically favorable to donate electron to Pd or Au. Combining these pieces of information, we proposed the oxidation half reaction as following (n reflects the number of electrons on metal):

$$\mathrm{M^{n}{-}Rz^{-*}} \longrightarrow \mathrm{M^{n+1}{-}Rz^{\bullet}} \qquad (3.13)$$

where $[\mathrm{M^{n+1}{-}Rz^{\bullet}}]$ is the surface-bound one-electron-oxidized radical species from resazurin.

In this mechanistic model, the metal catalyst behaves like an electron mediator so it could donate/accept electrons to/from excited-state resazurin to facilitate the disproportionation reaction. Combining Equations (3.8) and (3.13), the balanced chemical equation for the overall reaction is then:

$$3Rz^{-}+H_2O\xrightarrow[hv]{M}Rf^{-}+2Rz^{\bullet}+2OH^{-} \tag{3.14}$$

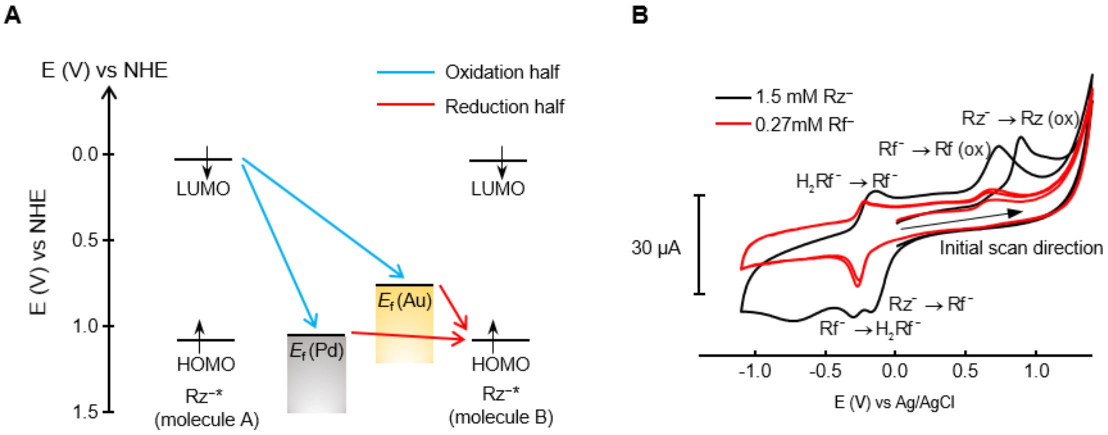

Figure 3.13 Energetics of the Pd/Au-catalyzed photo-driven disproportionation of resazurin to resorufin. (A) Energy level diagram of the HOMO and LUMO of resazurin and the Fermi level of Pd and Au; all referenced to the normal hydrogen electrode (NHE). The blue and red arrows refer to the oxidation and reduction pathways. The energies of HOMO (1.08 V) and LUMO (0.03 V) of resazurin were estimated from the electrochemistry measurement of resazurin, which were consistent with the DFT calculation results ($E_{\text{HOMO}} = 0.99$ V, $E_{\text{LUMO}} = -0.34$ V) (B) Cyclic voltammetry (CV) of 1.5 mM resazurin (black) and 0.27 mM resorufin (red) in 0.2 M pH 7.2 phosphate buffer. Scan rate = 25 mV s^{-1}; glassy carbon working electrode.

Cyclic voltammetry (CV) of resazurin and resorufin. As shown in Figure 3.13B, we measured the oxidation and reduction potentials of resazurin and resorufin. For resazurin (black): 1) the irreversible reduction wave with a peak potential at −0.18 V is the reduction of resazurin (Rz^{-}) to resorufin (Rf^{-})[11], 2) the irreversible oxidation wave at 0.89 V is the oxidation of resazurin to an unknown product (Rz (ox)), 3) the reversible redox waves at −0.31 V and −0.15 V are from the resorufin (Rf^-) /dihydroresorufin (H_2Rf^-) redox couple,[11] and 4) the irreversible oxidation wave at 0.74 V is the oxidation of resorufin to an unknown species (Rf (ox)). For resorufin (red), expectedly, 3) and 4) regarding Rf^-/H_2Rf^- reversible conversion and oxidation of resorufin appeared, further supporting our assignment. Note the measured reduction of resazurin (Rz^-) to resorufin (Rf^-) is a 2-electron process and the oxidation of resazurin to an unknown product (Rz (ox)) is also a 2-electron process (confirmed by the area under the peak). We approximated these two potentials as the energy levels of HOMO and LUMO. This approximation is valid by that they are close to the independent DFT calculation results (1.08 V vs. 0.99 V for HOMO, 0.03V vs. −0.34 V for LUMO; former from CV, latter from DFT).

3.5.5 Additional data: adsorption equilibrium constant of the reactant *K* of the gapped-PdAu nanoparticles

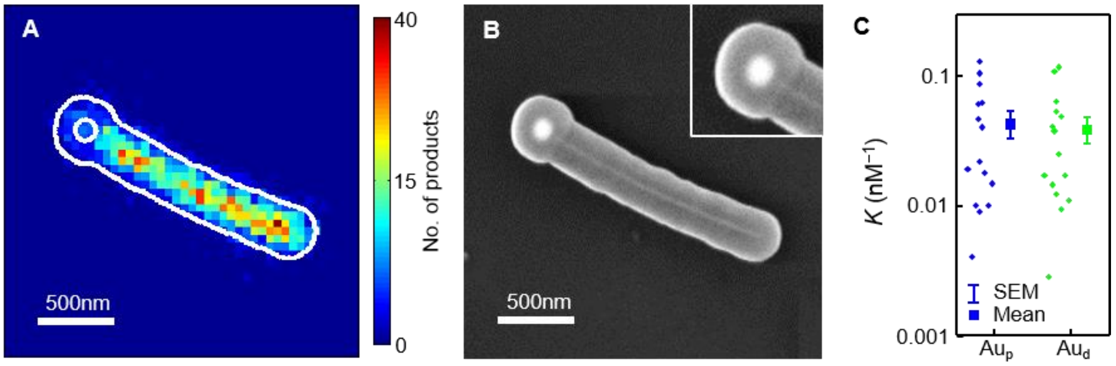

Figure 3.14 Additional super-resolution catalysis imaging results of gap-PdAu nanoparticles. (A) 2-D histogram of catalytic product positions on a gap-PdAu nanoparticle. (B) SEM image of the particle in A; the inset is the zoom-in of the nano-gap. (C) The adsorption equilibrium constant of the reactant *K* of the Au hemispheres proximal to (Au_p) and distant from (Au_d) the Pd nanorod in the gapped-PdAu nanoparticles. No appreciable difference is observed between two hemispheres.

3.6 FDTD simulations

3.6.1 Method

The 2D finite-difference time-domain (FDTD) simulations were performed to calculate the electric field intensity distribution on a PdAu nanoparticle surface, using a commercial software (Lumerical Solutions). The grid size was set 2×2 nm^2 and refractive index of the background medium was set as 1.33 (water). All the material properties were set based on the default optical material database (Palik). We used 532 nm circularly polarized light source (composed by two orthogonal linearly-polarized light sources with 90 degree phase difference) to excite a model PdAu nanoparticle, composed of a 120 nm diameter spherical Au particle attached to one end of a Pd nanorod of 400 nm in length and 30 nm in diameter. To mimic the experiment configuration, the incident light propagation direction was fixed and the PdAu nanoparticle was rotated to cover all the possible orientations in the experiment. An exemplary FDTD simulation result is shown in Figure 3.15A, upper panel, in which the PdAu nanoparticle is parallel to the light propagation direction. Its orientation angle θ is 0°, based on the definition shown in the inset. Following the similar segmentation schemes as in the super-resolution catalysis imaging analysis, we defined the locations to calculate the electric field intensity enhancement ($|E|^2/|E_0|^2$) of the bimetallic (Pd_{Au}, Au_{Pd}) and monometallic (Pd, Au) regions (Figure 3.15A, lower panel). We only considered the locations within 2 nm of the metal surface because the catalytic reactions occur at the surface and the size of the reactant and product molecules are ~1 nm. As expected, the local $|E|^2/|E_0|^2$ is dependent on the particle orientation (Figure 3.15B; note that θ is varied every 15° from 0° to 180° and when $\theta > 180°$, it is equivalent to $(360-\theta)°$ because of symmetry). So we calculated $|E|^2/|E_0|^2$ of the bimetallic and monometallic regions for each individual particle based on its actual orientation in the imaging experiment.

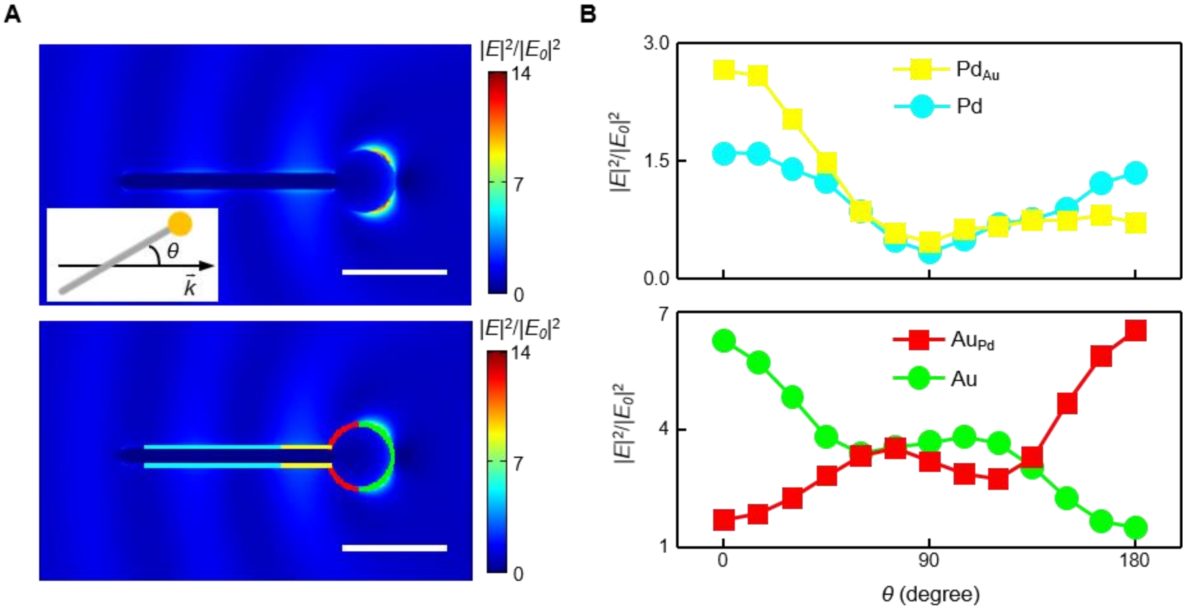

Figure 3.15 FDTD simulations of the PdAu nanoparticles. (A) Upper: the electric field intensity enhancement ($|E|^2/|E_0|^2$) pattern of the PdAu nanoparticle excited by 532 nm circularly polarized light with the propagation direction from left to right (shown in the inset). The inset in the upper panel shows the definition of the particle orientation angle θ with respect to the light propagation direction. For the PdAu nanoparticle presented here, $\theta = 0°$. Lower: The locations defined to calculate $|E|^2$ of the bimetallic regions, $\mathrm{Pd_{Au}}$ (yellow), $\mathrm{Au_{Pd}}$ (red), and monometallic regions, Pd (cyan), and Au (green). Only the near-surface (within 2 nm) region was considered in determining the $|E|^2/|E_0|^2$ for each region because both the reactant and product molecule sizes are ~1 nm. (B) $|E|^2/|E_0|^2$ of the bimetallic and monometallic regions versus particle orientation angle θ. The scale bars represent 200 nm.

3.6.2 No significant plasmonic effect in catalysis

The FDTD simulations of the electric field intensity ($|E|^2$) pattern around the

PdAu nanoparticle can be used to evaluate whether the surface plasmon excitation of Au nanoparticle by 532 nm laser light may or may not play a role in the observed catalytic enhancement around the Pd-Au interface. As shown in Figure 3.15A, the localized electric field enhancement is expectedly clear around the Au nanoparticle, while there is no significant enhancement near the Pd-Au interface or around the Pd nanorod, as 532 nm light does not excite Pd surface plasmon effectively. The $|E|^2$ ratios of bimetallic vs. monometallic regions, i.e., Pd_{Au}/Pd and Au_{Pd}/Au, for all possible particle orientations are shown in Figure 3.16A, upper. Taking into account the actual orientations of all PdAu nanoparticles we examined (Figure 3.16A, lower), the weighted average of the $|E|^2$ enhancement for both Pd_{Au} vs. Pd and Au_{Pd} vs. Au are merely 12% and 4%, respectively, because most of the nanoparticles are within the orientation range of 30 to 150° where $|E|^2$ ratios for both Pd_{Au}/Pd and Au_{Pd}/Au are ~1. This $|E|^2$ enhancement is much smaller than the observed average activity enhancement (~50%; Figure 2.3A, lower). Moreover, no correlation was observed between the catalytic rate constant k ratio and the local $|E|^2$ ratio of the bimetallic to monometallic regions (Figure 3.17).

We further normalized the catalytic rate constant k of each segment by its local $|E|^2$ to factor out the potential contribution of local electric field enhancement. The resulting normalized k' of the bimetallic Pd_{Au} and Au_{Pd} regions are still ~50% and ~70% larger than those of the monometallic Pd and Au regions, respectively (Figure 3.16B). Taken together, these results indicate that plasmonic enhancement effect does not make a significant contribution to the observed catalytic enhancement at the bimetallic regions of the PdAu nanoparticles, even though the reaction is photo-driven.

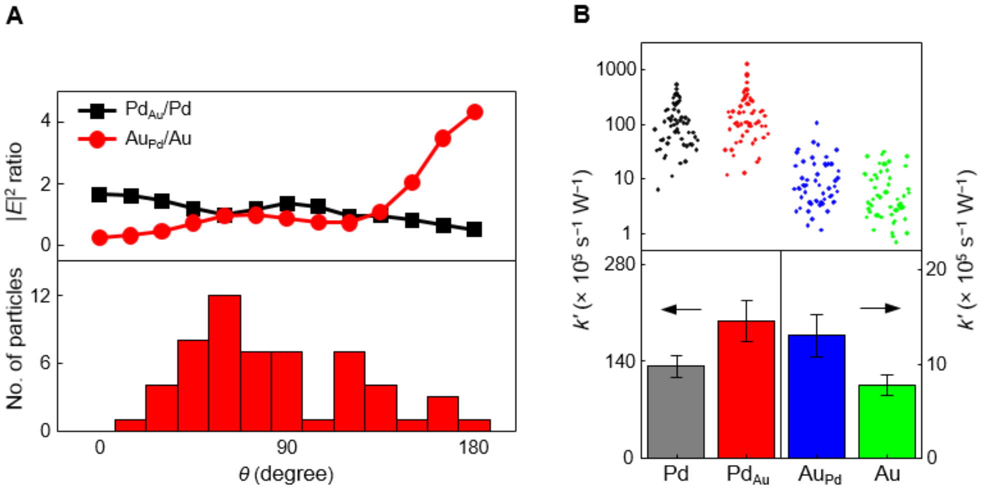

Figure 3.16 No significant plasmonic effect in catalysis. (A) Upper: the $|E|^2$ ratios of bimetallic vs. monometallic regions for Pd_{Au}/Pd and Au_{Pd}/Au as a function of particle orientation to the *k*-vector (light propagation direction). Lower: the orientation distribution of the PdAu nanoparticle examined experimentally. (B) The normalized catalytic rate constant *k*′ of bimetallic and monometallic regions of individual PdAu nanoparticles after factoring out the local electric field intensity enhancement contribution (upper). Lower panel shows the particle-averaged values; error bars are s.e.m.

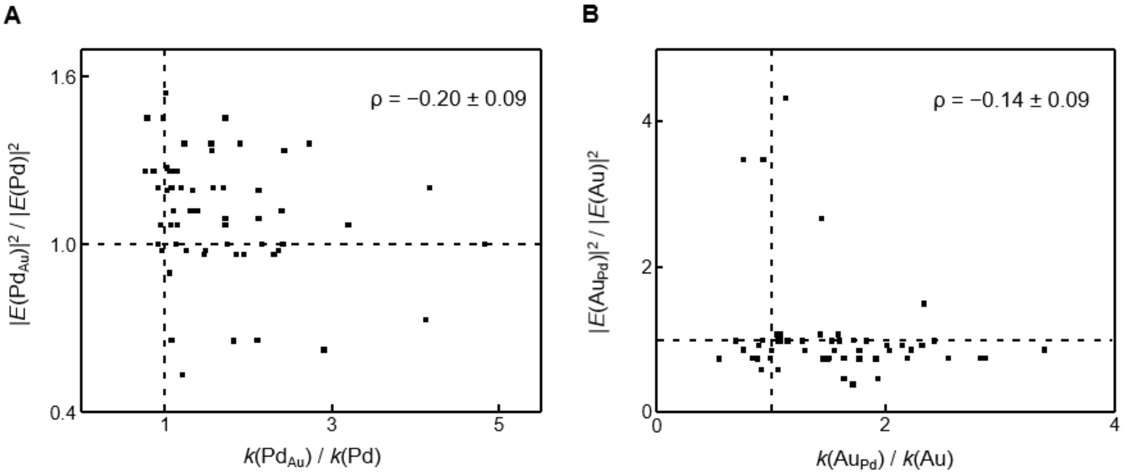

Figure 3.17 No correlation between the local electric field intensity and catalytic activity of PdAu nanoparticles. The correlation between the electric field intensity ($|E|^2$) ratio and catalytic rate constant (k) ratio of the bimetallic region over monometallic region, for Pd (A) and Au (B), respectively. Each dot represents a single PdAu nanoparticle (total 53). For each particle, the local $|E|^2$ of the bimetallic and monometallic regions were calculated based on its actual orientation in the experiment. The dashed vertical and horizontal lines go through (1, 1).

3.7 DFT calculations

3.7.1 Method

The DFT calculations of resazurin adsorption on Pd or Au surfaces were performed using the Vienna Ab initio Simulation Package (VASP, version 5.3.5)[12,13] in vacuum at 0 K. A plane-wave basis set of 400 eV energy cutoff was used with the

Perdew–Burke–Ernzerhof (PBE) exchange-correlation functional[14,15] and the projector augmented wave (PAW) pseudopotentials[16,17]. The convergence criteria are 10^{-4} eV for the electronic relaxation and 10^{-3} eV for the ionic relaxation (i.e., geometry optimization). Dispersion correction was included by using the zero damping DFT-D3 method of Grimme[18].

For fcc Pd (100) and Au (111) surfaces, we used a 6 × 6 supercell of five layers (180 metal atoms in total) with a vacuum region of more than six layers to break the interactions between neighboring surfaces. The lattice constants of Pd and Au were set as 3.89 Å and 4.08 Å[19], respectively. We only sampled the Gamma point in *k*-space because the supercell is very big. Both the metal surface and resazurin molecule were first geometry optimized and then put together to calculate the adsorption geometry, in which we had one resazurin molecule (per supercell) on top of the metal surface and geometry optimized the system (only the resazurin molecule and the top surface layer of the metal atoms were allowed to relax). A series of initial locations and orientations of resazurin on the surface were considered on the basis of the symmetry and possible important atomic interactions; all the cases were geometry optimized and the most stable one in energy was treated as the final adsorption geometry.

To investigate bimetallic effects on the Pd-based and Au-based surfaces, we used single-atom-substitution by the second metal to construct bimetallic surfaces. Starting from Pd (100) or the Au (111) surface, we substituted the surface atom that was identified to be involved in the adsorbate-surface interaction. We substituted all the relevant single surface atoms, one at a time, and optimized resazurin adsorption geometries on each of the constructed bimetallic surfaces. The most stable one was used as the final adsorption geometry on the bimetallic surface. The bond lengths were directly measured from the optimized geometries and the atomic charges were calculated by Bader's analysis, using the code developed by Henkelman et al[20,21].

The adsorption energy E_{ads} was defined as

$$E_{\mathrm{ads}}=E_{\mathrm{slab}}+E_{\mathrm{Rz}}-E_{\mathrm{slab+Rz}} \tag{3.15}$$

where E_{slab} is the electronic energy of the metal slab (monometallic or bimetallic) without resazurin adsorption and E_{Rz} is the electronic energy of the free resazurin and $E_{\mathrm{slab+Rz}}$ is the electronic energy of the metal slab with resazurin bound to the surface.

Crystal orbital Hamilton population (COHP) analysis[22,23] was performed to analyze the bonding interactions between Rz and the metal surface, using the Local-Orbital Basis Suite Towards Electronic-Structure Reconstruction package (LOBSTER, version 2.0.0)[24]. We specifically analyzed the interactions between the O or N atom of the N–O fragment of resazurin and the closest surface metal atoms (Pd or Au). In COHP and density of states (DOS) diagrams, the zero energy point refers to the vacuum level. Note in COHP analysis, the convention is that the *x*-axis represents the reserved COHP value, labelled as –COHP, in order to make the bonding interaction appear in the positive region and antibonding interaction in the negative region.

Molecular orbitals (MOs) of resazurin were calculated using Gaussian 09 software (Gaussian, Inc.) with PBE/SDDALL level of theory and the results were compared with the DOS of resazurin calculated from VASP.

3.7.2 Resazurin adsorption on monometallic surfaces

3.7.2.1 Resazurin on Pd(100) surface

We show the initial and the corresponding optimized geometries of resazurin on Pd(100) surface in Figure 3.18 (the red color labels the most stable geometry). Since the initial resazurin position on the surface may affect the final adsorption geometry, we started with ten initial resazurin positions to try to cover the most possible situations (left structure in each panel in Figure 3.18). First, we considered both flat-on (structures I to VIII) and edge-on (structures IX to X) adsorption geometries. For the edge-on geometries, we considered two candidates and each had a single O atom on top of a Pd atom. For the flat-on geometries, we consider two general molecular orientations: the long axis of resazurin's phenoxazine ring (indicated by the arrow in Figure 3.18, structure I) parallel to the edge (structures I to IV) and to the diagonal (structures V to VIII) of the supercell, which is a square from the top view. For each general orientation, the resazurin molecule was translated on the surface in order to form possible interactions with the surface atoms (i.e., atoms of resazurin to be directly on or close to be on-top of some metal surface atoms). The ten initial geometries were optimized (right structure in each panel in Figure 3.18) and the most stable one (structure III) is the flat-on configuration in which the Pd–C interactions dominate.

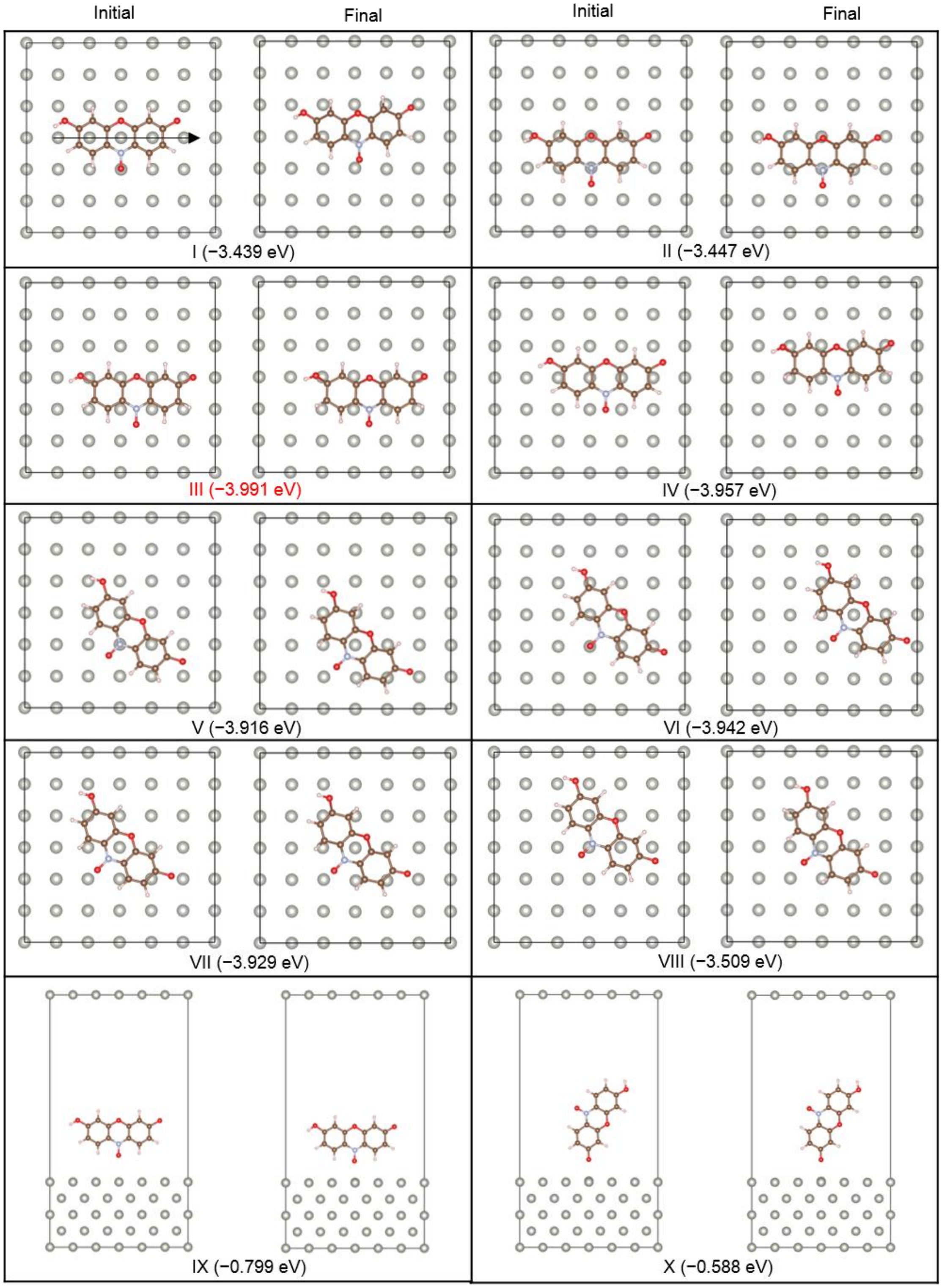

Figure 3.18 Initial (left) and optimized (right) geometries of resazurin on Pd(100) surface. Structures I-VIII are flat-on configurations and structures IX-X are edge-on

configurations. The most stable candidate (structure III) was taken as the final adsorption geometry of resazurin on Pd(100) surface. The arrow in structure I is the long axis of the phenoxazine ring of resazurin.

3.7.2.2 Resazurin on Au(111) surface

Figure 3.19 presents the initial and optimized geometries of resazurin on Au(111) surface. Similarly, we consider flat-on (structures I-VIII) and edge-on (structures IX-X) configurations. For the flat-on ones, we considered two general molecular orientations: the long axis of phenoxazine ring (indicated by the arrow in Figure 3.19A, structure I) along (structures I-II) the longer diagonal of the supercell, which is a rhombus from the top view; and along the edge of the supercell (structures III-V). From the optimized results of structures I-V, we found that the Au–O interaction is favorable as structure II was the most stable among the five structures. Therefore, based on structure II, the resazurin molecule was rotated around the O atom (which is on top of a Au atom) by 15° (structure VI), 30° (structure VII), 45° (structure VIII) to search for more stable geometries. Of all ten optimized geometries, structure II turned out to be the most stable one, in which the Au–O interaction is important.

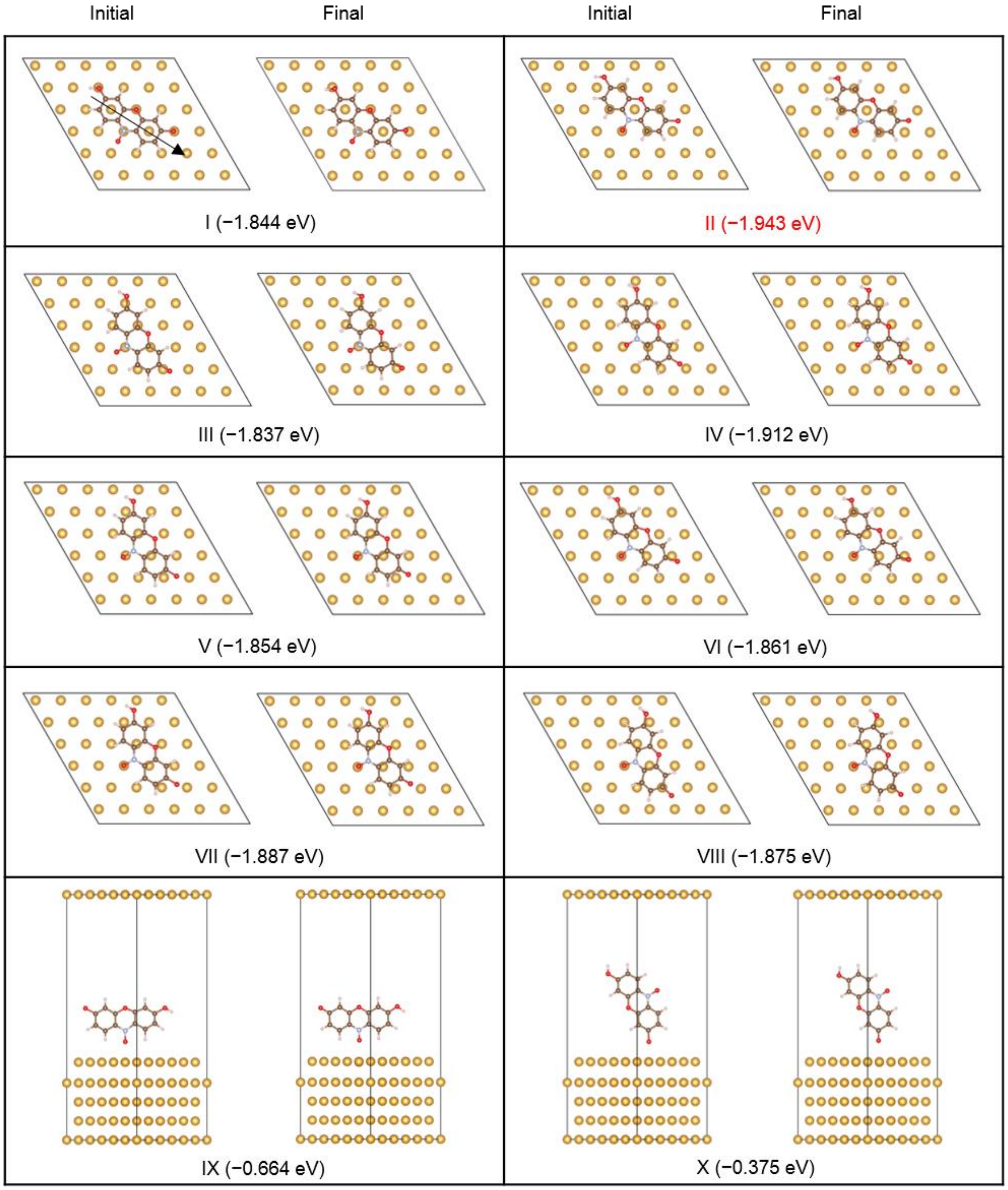

Figure 3.19 Initial (left) and optimized (right) geometries of resazurin on Au(111) surface. Structures I-VIII are flat-on configurations and structures IX-X are edge-on configurations. The most stable candidate (structure II) was taken as the final adsorption

geometry of resazurin on Au(111) surface. The arrow in structure I is the long axis of the phenoxazine ring of resazurin.

3.7.3 Resazurin adsorption on bimetallic surfaces

3.7.3.1 Resazurin on Au@Pd(100) surface

Based on the most stable geometries of resazurin on Pd(100) (Structure III in Figure 3.18), there are eight surface Pd atoms dominating the interactions with resazurin (labelled 1-8 in Figure 3.20A). For each of them, we substituted it with a Au atom to construct the Au@Pd(100) bimetallic surface and subsequently optimized the adsorption geometry (Table 3.2). Among the eight substitution candidates, six substituted structures have equal or longer N–O bond length than that on Pd(100) surface. The substitutions at Pd atom no.2 and no. 8 are the two most stable ones (Figure 3.20B, C, E, F). We focus more attention on structure no. 2 since it has a more lengthened N–O bond (by 0.004 Å) compared with that on monometallic surface (Table 3.2), which means there is more N−O bond activation. Structure no. 8, although slightly more stable than structure 2 (by 0.006 eV), its N−O bond is shorter (by 0.003 Å) than that on Pd(100), reflecting a deactivation of the N−O bond, which makes it irrelevant for bimetallic enhancement.

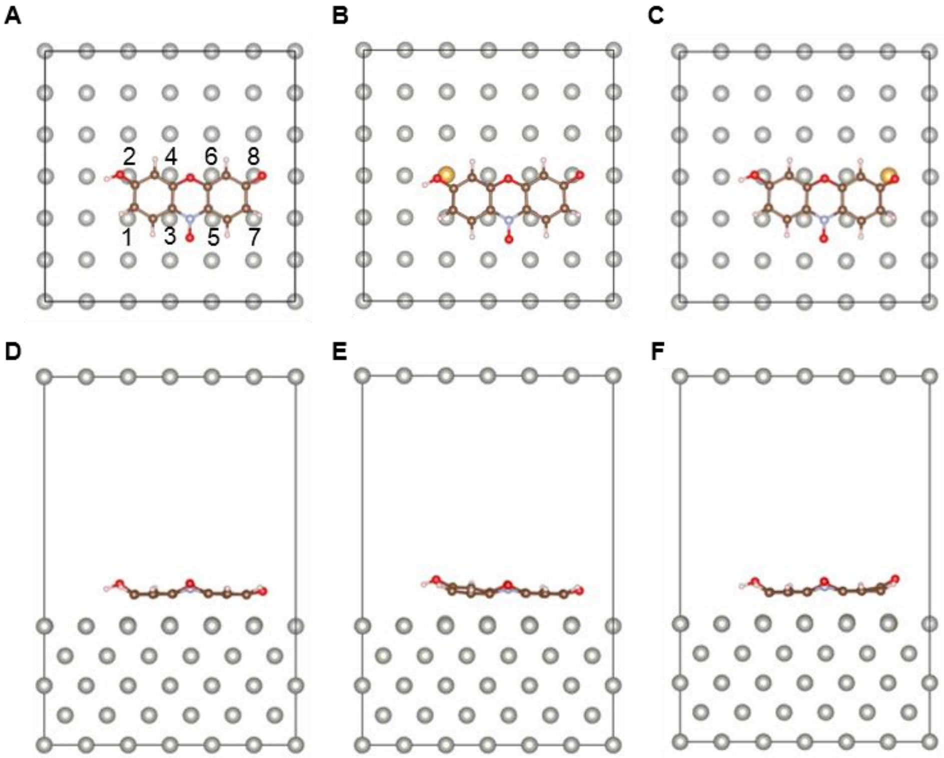

Figure 3.20 Adsorption geometries of resazurin on Au@Pd(100). (A) The most stable adsorption geometry of resazurin on Pd (100). Same as Structure III in Figure 3.18. The Pd atoms (labelled 1-8), which directly interact with resazurin, were individually replaced to build bimetallic surfaces. (B, C) The adsorption geometries of resazurin on Au@Pd(100) with substitutions at Pd atom no.2 and no.8, respectively, which are the two most stable adsorption geometries of all eight candidates formed by single-atom-substitutions. (D-F). Front views of structures in A-C, respectively.

Table 3.2 Geometric and charge properties of resazurin adsorbed on Pd(100) and single-atom substituted Au@Pd(100) bimetallic surfaces from DFT calculations

Rz-adsorption surface [a]	E_{ads} (eV)	$\Delta r_{N–O}$ (Å) [b]	$r_{M–O}$ (Å) [c]	$r_{M–N}$ (Å) [c]	ΔQ_{Rz} (e) [d]	$\Delta Q_{N–O}$ (e) [d]
1	−3.464	0.007	3.436	2.815	0.499	0.053
2	−3.530	0.011	3.291	2.785	0.456	0.025
3	−3.416	0.009	3.479	2.924	0.490	0.115
4	−3.395	0.008	3.323	2.810	0.478	0.082
5	−3.409	0.009	3.503	2.949	0.487	0.088
6	−3.449	0.007	3.359	2.828	0.481	0.033
7	−3.511	0.004	3.446	2.814	0.473	−0.003
8	−3.536	0.004	3.396	2.796	0.447	−0.015
Pd(100)	−3.991	0.007	3.391	2.804	0.548	0.026

[a] The numbers refer to the single-atom-substitution position, as shown in Figure 3.20A. (2 and 8, highlighted in red, are the most stable ones.) [b] $\Delta r_{N–O}$ is the elongation of the N–O bond compared to that of free resazurin (1.273 Å). [c] $r_{M–O}$ (or $r_{M–N}$) refers to the average distance between O (or N) and all bridged metal atoms. [d] ΔQ_{Rz} and $\Delta Q_{N–O}$ refer to the net charge transfer from metal to resazurin and to the N–O fragment, respectively. All charges were calculated by Bader's analysis. For free resazurin, the total charge Q_{Rz} is 84 and the charge of the N–O fragment $Q_{N–O}$ is 13.150.

3.7.3.2 Resazurin on Pd@Au(111) surface

Based on the most stable geometries of resazurin on Au(111) (Structure II in Figure 3.19), there are five surface Au atoms that dominate the interactions with resazurin (labelled 1-5 in Figure 3.21A). Similarly, for each of them, we substituted it with a Pd atom to construct a Pd@Au(111) bimetallic surface and subsequently optimized the adsorption geometry (Table 3.3). All five candidates have longer N–O bond length than that on Au(111) and the most stable one (substitution of Au atom no. 4) is shown in Figure 3.21B and D.

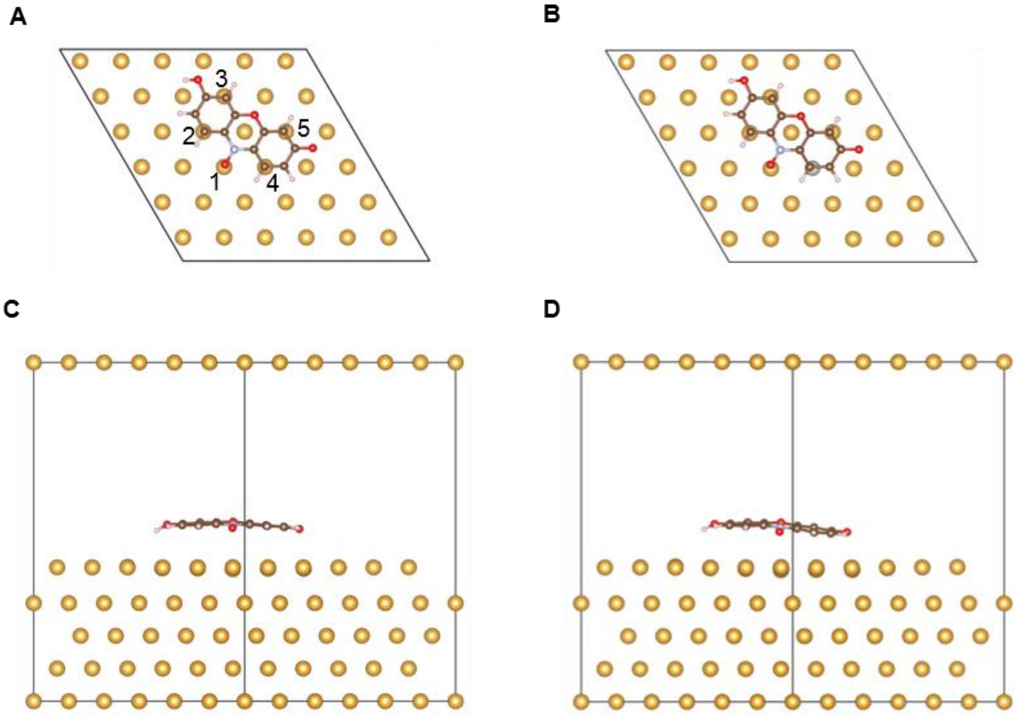

Figure 3.21 Adsorption geometries of resazurin on Pd@Au (111). (A) The most stable adsorption geometry of resazurin on Au(111); same as structure II in Figure 3.19. The Au atoms (labelled 1-5), which directly interact with resazurin, were individually replaced to build bimetallic surfaces. (B) The adsorption geometries of resazurin on Pd@Au(111) with substitution at Au atom no.4, which is the most stable adsorption geometry of all five candidates formed by single-atom-substitutions. (C-D) Rotated front views (in which the N–O of resazurin are pointing out of plane) of A and B.

Table 3.3 Geometric and charge properties of resazurin adsorbed on Au(111) and single-atom substituted Pd@Au(111) bimetallic surfaces from DFT calculations

Rz-adsorption surface [a]	E_{ads} (eV)	$\Delta r_{N–O}$ (Å) [b]	$r_{M–O}$ (Å) [c]	$r_{M–N}$ (Å) [c]	ΔQ_{Rz} (e) [d]	$\Delta Q_{N–O}$ (e) [d]
1	−1.998	0.018	2.522	3.307	0.021	0.055
2	−2.021	0.010	2.702	3.351	0.006	0.038
3	−1.980	0.008	2.782	3.411	−0.010	0.096
4	−2.089	0.013	2.665	3.342	0.023	0.045
5	−2.024	0.007	2.826	3.424	0.002	0.090
Au(111)	−1.943	0.006	2.845	3.457	−0.025	0.016

[a] The numbers refer to the single-atom-substitution position, as shown in Figure 3.21A. (4, highlighted in red, is the most stable one.) [b] $\Delta r_{N–O}$ is the elongation of the N–O bond compared to that of free resazurin (1.273 Å). [c] $r_{M–O}$ refers to the distance between O and closest metal atom and $r_{M–N}$ refers to the average distance between N and two bridged metal atoms. [d] ΔQ_{Rz} and $\Delta Q_{N–O}$ refer to the net charge transfer from metal to resazurin and to the N–O fragment, respectively. All charges were calculated by Bader's analysis. For free resazurin, the total charge Q_{Rz} is 84 and the charge of the N–O fragment $Q_{N–O}$ is 13.150.

3.7.4 Charge transfer between the metal and the adsorbed resazurin

We evaluated the charge transfer between resazurin and metal surfaces (Table 3.2, Table 3.3). For resazurin on Pd(100), the overall net charge transfer is from Pd to resazurin (0.548 *e*) with a small portion of it to N–O (0.026 *e*), because the phenoxazine ring dominates the overall interaction (Figure 3.20A, D). In contrast, for resazurin on Au(111), the overall net charge transfer is from resazurin to Au (−0.025*e*, the minus sign refers to the resazurin-to-Au charge transfer direction), but the N–O fragment still gains charge (0.016 *e*) from the surface. We think the differences in charge transfer on Pd(100) and Au(111) surfaces might be related to the observed higher activity of Pd than Au (Figure 2.3A). On Pd(100), due to the fact that π^*_{NO} orbital, the charge accepter orbital in the back-donation interaction, is delocalized over the entire molecule (Figure 2.5F), the charge transfer from Pd to ring structure could also go to N−O and contributes to the bond cleavage

On both Pd(100) and Au(111) surfaces, the net charge transfer between the metal and the N–O fragment is that the N–O fragment acquires charge from the metal surfaces, which indicates the back-donation (which results in a charge transfer into the N−O) is the more dominant interaction than forward-donation (which results in a charge transfer out of the N−O).

3.7.5 COHP analysis

In order to understand the adsorbate-surface bonding interactions, we did COHP analysis[22,23] and analyzed the interactions between metal and the N–O fragment of resazurin on Pd(100) and Au(111) surfaces (Figure 2.5C, D). Figure 3.22 below are the COHP analyses of resazurin on Au@Pd(100) (substitution at Pd atom no.2) and Pd@Au(111) (substitution at Au atom no.4) bimetallic surfaces, which are qualitatively similar to the ones on monometallic surfaces: both forward- and back-donation bonding interactions were identified ($\pi_{\text{N-O}} + d$ and $d + \pi^*_{\text{N-O}}$, respectively) between the metal and the N−O fragment. Compared with the monometallic surfaces, we found both forward- and back-donations were strengthened, as indicated by the larger integrated area under metal–O curve in the COHP diagram (Table 3.4). These results could rationalize, from the electronic structure perspective, the enhanced activation of the N–O bond for cleavage on the bimetallic surfaces because both forward- and back-donations result in the weakening of the N–O bond (see more discussions in Section 3.7.6).

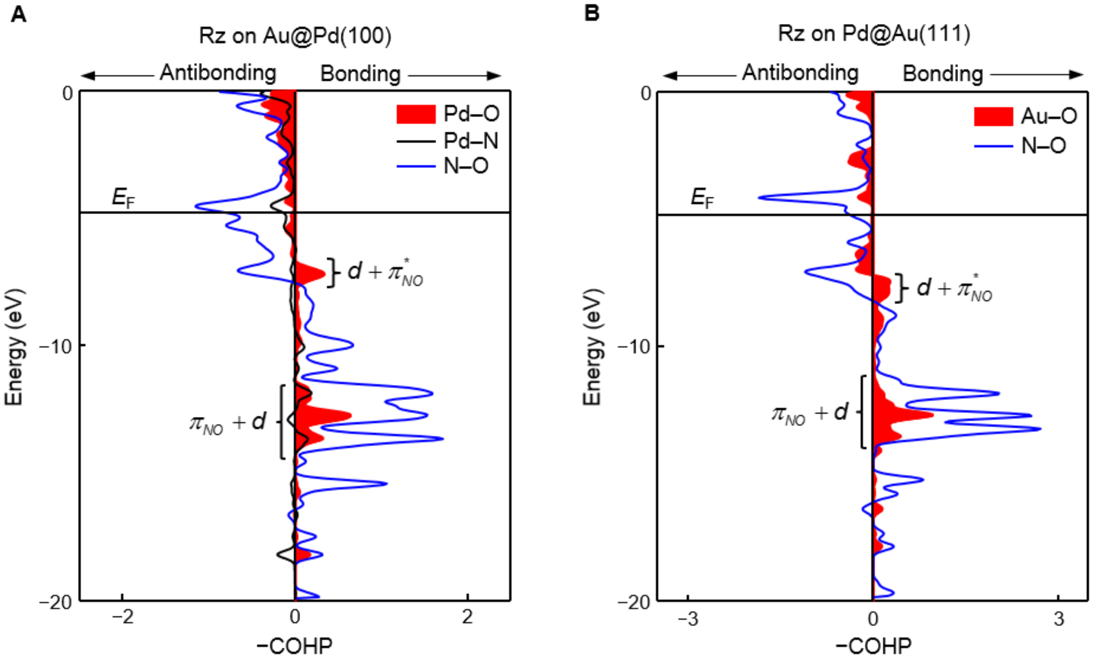

Figure 3.22 COHP analysis of resazurin on bimetallic surfaces. (A) The interactions between N−O and the bridged surface Pd atoms for resazurin on Au@Pd(100) (substitution at Pd atom no.2) surface, shown in Figure 3.20B and E. (B) The interactions between N−O and the closest surface Au atom for resazurin on Pd@Au(111) surface (substitution at Au atom no.4), shown in Figure 3.21B and D.

Table 3.4 Forward- and back-donations of metal–O interaction on monometallic and bimetallic surfaces [a]

Rz-adsorption surface	Forward-donation ($\pi_{N\text{-}O} + d$)	Back-donation ($d + \pi^{*}_{N\text{-}O}$)
Pd(100)	0.563	0.118
Au@Pd(100) [b]	0.645	0.166
Au(111)	0.657	0.121
Pd@Au(111) [c]	0.883	0.227

[a] The interactions are quantified by the integrated area under the metal-O curve in COHP analysis. [b] It refers to the Au@Pd(100) (substitution at Pd atom no.2, as shown in Figure 3.20B and E). [c] It refers to the Pd@Au(111) (substitution at Au atom no.4, as shown in Figure 3.21B and D).

3.7.6 MO diagrams of resazurin

We analyzed the molecular orbitals (MOs) of resazurin in order to identify the MOs that participate in the adsorbate-surface interactions, specifically the forward- and back-donations. Based on the COHP analysis (Figure 3.22) and DOS of resazurin (Figure 3.23A), we focus on two energy ranges (−7 to −2 eV and −13 to −10 eV, highlighted in the brackets in Figure 3.23A), which are relevant to the forward- and back-donations. The MO diagram of resazurin (from Gaussian calculations) is qualitatively similar to its DOS diagram (from VASP), as shown in Figure 3.23B and C, which helps identify the MOs involved in the forward and back-donations.

For the back-donation interaction, which requires an unoccupied MO of resazurin that is antibonding in nature between N and O (Figure 3.22A, blue curve), the

LUMO ($43\pi^*$ in Figure 3.23B) is a likely candidate to accept electron density from the metal *d*-block. Since this LUMO of resazurin is an anti-bonding orbital of the N−O fragment (Figure 3.24), donating electron density to this LUMO would weaken the N−O bond, thus activating it for cleavage. For the forward-donation interaction, there are a number of doubly occupied MOs in the corresponding energy range (Figure 3.23C). Since the resazurin molecule lies flat on the surface, the N−O orbitals should have lobes pointing toward the metal surface and perpendicular to the ring structure in order to form good orbital overlaps with the metal orbitals. Furthermore, the involved orbital of resazurin should be bonding in nature between the N and O atoms as shown by the COHP analysis in Figure 3.22A (blue curve). The π orbitals of N−O (20π and 25π, Figure 3.25) are thus likely candidates. We cannot differentiate these two, and simply picked 25π as a representative orbital for forward-donation interaction just to illustrate in Figure 2.5E in, as 25π is higher in energy and closer to the Fermi level as a frontier orbital.

Note: We matched the Fermi level of resazurin, calculated by VASP, with the midpoint between its LUMO and HOMO, calculated by Gaussian, to align DOS and MO diagrams (Figure 3.23B and C).

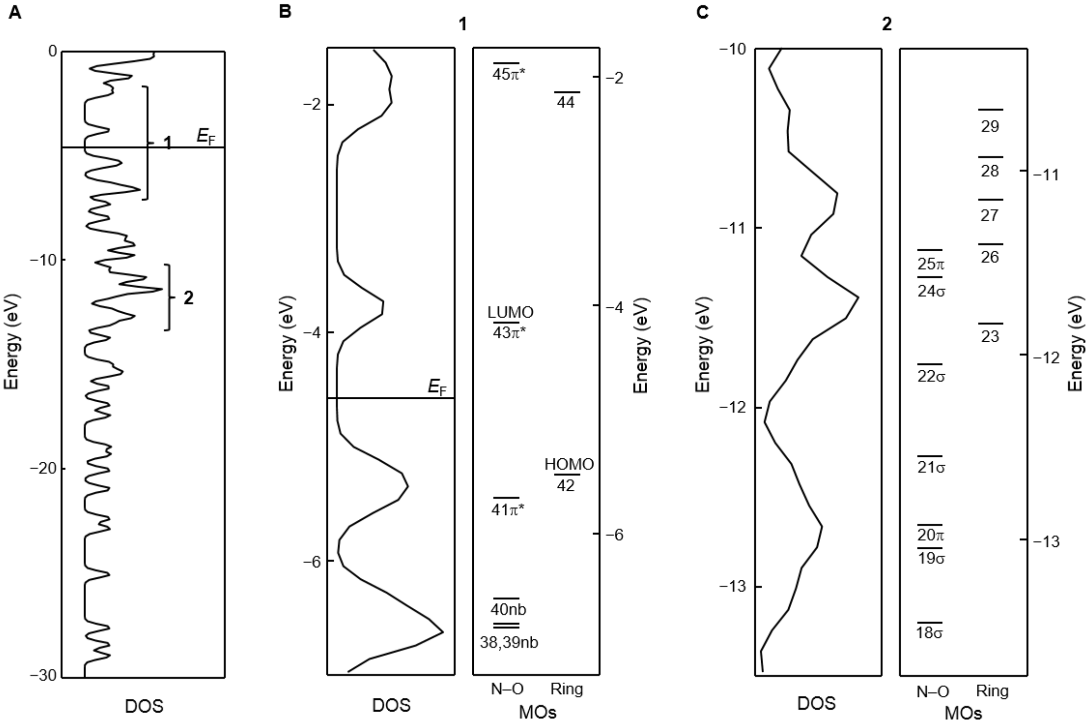

Figure 3.23 Resazurin bonding analysis. (A) DOS of resazurin from VASP calculations. The states in energy range 1 and range 2 (highlighted by brackets) are the relevant ones forming bonding interactions with metal surface. (B) MO analysis of resazurin in energy range 1: the left panel is the DOS from VASP and the right panel is the MO diagram of resazurin in the same energy range from Gaussian. The MOs are divided into two groups: the left and right columns represent ones with and without significant N–O fragment contributions, respectively. The MOs are labeled by the orbital number and the N–O bonding nature (if any), such as σ, π, and nb (non-bonding). (C) Same as B but for energy range 2. All the MOs in range 1 and range 2 are shown in Figure 3.24 and Figure 3.25, respectively.

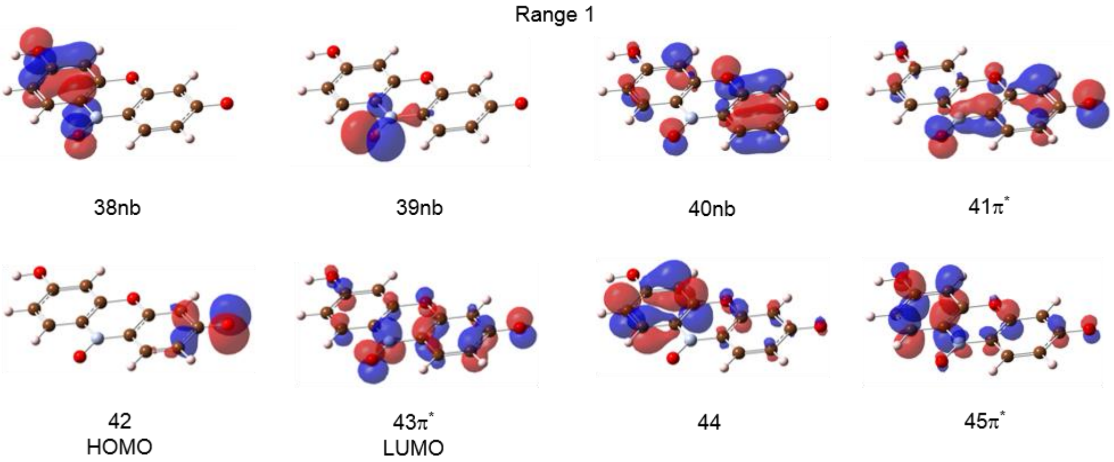

Figure 3.24 MOs of resazurin in energy range 1.

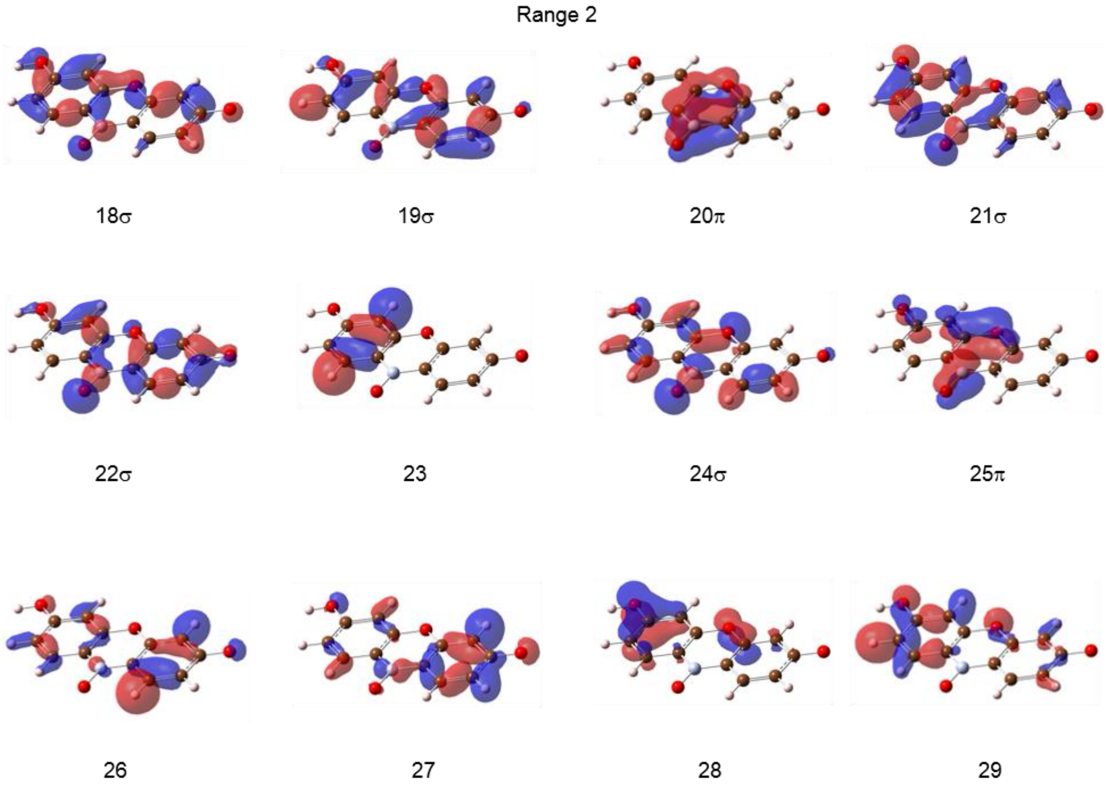

Figure 3.25 MOs of resazurin in energy range 2.

3.7.7 DOS decomposition in correlation with the COHP analysis

To gain more information on the nature of orbitals involved in the forward- and back-donation interactions that were identified by COHP analysis, we examined the orbital compositions of relevant states. Since the COHP analyses of resazurin on monometallic and bimetallic surfaces gave qualitatively similar results, we use the monometallic cases to illustrate the decomposition of the DOS (Figure 3.26). Parallel to the COHP analysis (middle panels in Figure 3.26A and B), we show the decomposition of DOS into those of the involved metal atoms (left) and that of the N–O fragment (right). In the energy range corresponding to the forward-donation interaction (i.e., $\pi_{N\text{–}O} + d$, about –12 to −13 eV), the DOS is well below the *d*-block of Pd or and Au (about –7 to −8 eV) and has significant contributions from the N–O fragment (and little from the metal). Therefore, the energy levels for the forward-donation interactions comprise mainly of N-O fragment in character and are denoted as $\pi_{N\text{–}O} + d$. In the energy range corresponding to the back-donation interactions (i.e., $d + \pi^*_{N\text{–}O}$, about –7 to −8 eV), the DOS is in the *d*-block range and well below the LUMO of resazurin (about −4 eV); therefore, the energy levels for the back-donation interactions are mainly metal *d* in character and denoted as $d + \pi^*_{N\text{–}O}$. Note: in the DOS from the N–O fragment, there is a peak in the back-donation energy range (about −7 eV), which are due to the lone pairs of the O atom (corresponding to the orbitals 38, 39, 40 in Figure 3.24) and not relevant to the back-donation interactions.

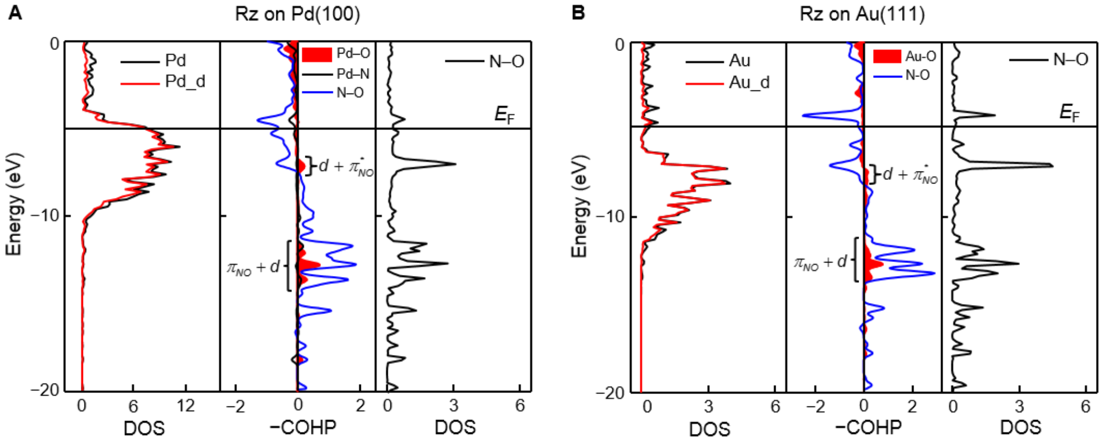

Figure 3.26 DOS decompositions of Rz adsorption on Pd(100) (A) and Au(111) (B) in correlation with the COHP analysis. (A) Resazurin on Pd(100). The middle panel is the COHP analysis of the interaction between the bridged Pd atoms and the N–O fragment of resazurin, which is also shown in Figure 2.5C. The left and right panels are the corresponding DOS from the four bridged Pd atoms (black lines; their d-orbital component is shown in red line) and N–O fragment of resazurin, respectively. (B) Same as A but for resazurin on Au(111). Here the DOS of Au is the Au atom right under the O of the N–O fragment. The COHP analysis (middle) is for the interaction between that Au atom and O, which is also shown in Figure 2.5D.

3.8 References

(1) Huang, X. Q.; Zheng, N. F. One-Pot, High-Yield Synthesis of 5-Fold Twinned Pd Nanowires and Nanorods. *J Am Chem Soc* **2009**, *131*, 4602-4603.

(2) Zhou, X. C.; Andoy, N. M.; Liu, G. K.; Choudhary, E.; Han, K. S.; Shen, H.; Chen, P. Quantitative super-resolution imaging uncovers reactivity patterns on single nanocatalysts. *Nat Nanotechnol* **2012**, *7*, 237-241.

(3) Andoy, N. M.; Zhou, X. C.; Choudhary, E.; Shen, H.; Liu, G. K.; Chen, P. Single-Molecule Catalysis Mapping Quantifies Site-Specific Activity and Uncovers Radial Activity Gradient on Single 2D Nanocrystals. *J Am Chem Soc* **2013**, *135*, 1845-1852.

(4) Botella, P.; Corma, A.; Navarro, M. T. Single gold nanoparticles encapsulated in monodispersed regular spheres of mesostructured silica produced by pseudomorphic transformation. *Chem Mater* **2007**, *19*, 1979-1983.

(5) Kundu, S.; Ravishankar, N. Rapid synthesis of hybrids and hollow PdO nanostructures by controlled in situ dissolution of a ZnO nanorod template: insights into the formation mechanism and thermal stability. *Nanoscale* **2016**, *8*, 1462-1469.

(6) Jana, N. R.; Gearheart, L.; Murphy, C. J. Seed-mediated growth approach for shape-controlled synthesis of spheroidal and rod-like gold nanoparticles using a surfactant template. *Adv Mater* **2001**, *13*, 1389-1393.

(7) Bueno, C.; Villegas, M. L.; Bertolotti, S. G.; Previtali, C. M.; Neumann, M. G.; Encinas, M. V. The excited-state interaction of resazurin and resorufin with amines in aqueous solutions. Photophysics and photochemical reaction. *Photochem Photobiol* **2002**, *76*, 385-390.

(8) Balcerzyk, A.; Baldacchino, G. Implementation of laser induced fluorescence in a pulse radiolysis experiment - a new way to analyze resazurin-like reduction mechanisms. *Analyst* **2014**, *139*, 1707-1712.

(9) Sambur, J. B.; Chen, T. Y.; Choudhary, E.; Chen, G. Q.; Nissen, E. J.; Thomas, E. M.; Zou, N. M.; Chen, P. Sub-particle reaction and photocurrent mapping to optimize catalyst-modified photoanodes. *Nature* **2016**, *530*, 77-80.

(10) Chen, T. Y.; Santiago, A. G.; Jung, W.; Krzeminski, L.; Yang, F.; Martell, D. J.; Helmann, J. D.; Chen, P. Concentration- and chromosome-organization-dependent regulator unbinding from DNA for transcription regulation in living cells. *Nat Commun* **2015**, *6*, 7445.

(11) Xu, W. L.; Shen, H.; Kim, Y. J.; Zhou, X. C.; Liu, G. K.; Park, J.; Chen, P. Single-Molecule Electrocatalysis by Single-Walled Carbon Nanotubes. *Nano Lett* **2009**, *9*, 3968-3973.

(12) Kresse, G.; Furthmuller, J. Efficient iterative schemes for ab initio total-energy calculations using a plane-wave basis set. *Phys Rev B* **1996**, *54*, 11169-11186.

(13) Kresse, G.; Furthmuller, J. Efficiency of ab-initio total energy calculations for metals and semiconductors using a plane-wave basis set. *Comp Mater Sci* **1996**, *6*, 15-50.

(14) Perdew, J. P.; Burke, K.; Ernzerhof, M. Generalized gradient approximation made simple. *Phys Rev Lett* **1996**, *77*, 3865-3868.

(15) Perdew, J. P.; Burke, K.; Ernzerhof, M. Generalized gradient approximation made simple (vol 77, pg 3865, 1996). *Phys Rev Lett* **1997**, *78*, 1396-1396.

(16) Blochl, P. E. Projector Augmented-Wave Method. *Phys Rev B* **1994**, *50*, 17953-17979.

(17) Kresse, G.; Joubert, D. From ultrasoft pseudopotentials to the projector augmented-wave method. *Phys Rev B* **1999**, *59*, 1758-1775.

(18) Grimme, S.; Antony, J.; Ehrlich, S.; Krieg, H. A consistent and accurate ab initio parametrization of density functional dispersion correction (DFT-D) for the 94 elements H-Pu. *J Chem Phys* **2010**, *132*, 154104.

(19) Hermann, K.: *Crystallography and surface structure : an introduction for surface scientists and nanoscientists*; Wiley-VCH: Weinheim, Germany, 2011.

(20) Henkelman, G.; Arnaldsson, A.; Jonsson, H. A fast and robust algorithm for Bader decomposition of charge density. *Comp Mater Sci* **2006**, *36*, 354-360.

(21) Tang, W.; Sanville, E.; Henkelman, G. A grid-based Bader analysis algorithm without lattice bias. *J Phys-Condens Mat* **2009**, *21*, 084204.

(22) Deringer, V. L.; Tchougreeff, A. L.; Dronskowski, R. Crystal Orbital Hamilton Population (COHP) Analysis As Projected from Plane-Wave Basis Sets. *J Phys Chem A* **2011**, *115*, 5461-5466.

(23) Dronskowski, R.; Blochl, P. E. Crystal Orbital Hamilton Populations (Cohp) - Energy-Resolved Visualization of Chemical Bonding in Solids Based on Density-Functional Calculations. *J Phys Chem-Us* **1993**, *97*, 8617-8624.

(24) Maintz, S.; Deringer, V. L.; Tchougreeff, A. L.; Dronskowski, R. LOBSTER: A Tool to Extract Chemical Bonding from Plane-Wave Based DFT. *J Comput Chem* **2016**, *37*, 1030-1035.